


8-2020

Directed Evolution of Macrocyclic Peptides for Inhibition of Autophagy

Joshua Gray

Follow this and additional works at: https://digitalcommons.library.tmc.edu/utgsbs_dissertations

 Part of the [Amino Acids, Peptides, and Proteins Commons](#), [Chemical and Pharmacologic Phenomena Commons](#), and the [Medicinal-Pharmaceutical Chemistry Commons](#)

Recommended Citation

Gray, Joshua, "Directed Evolution of Macrocyclic Peptides for Inhibition of Autophagy" (2020). *The University of Texas MD Anderson Cancer Center UTHealth Graduate School of Biomedical Sciences Dissertations and Theses (Open Access)*. 1026.

https://digitalcommons.library.tmc.edu/utgsbs_dissertations/1026

This Dissertation (PhD) is brought to you for free and open access by the The University of Texas MD Anderson Cancer Center UTHealth Graduate School of Biomedical Sciences at DigitalCommons@TMC. It has been accepted for inclusion in The University of Texas MD Anderson Cancer Center UTHealth Graduate School of Biomedical Sciences Dissertations and Theses (Open Access) by an authorized administrator of DigitalCommons@TMC. For more information, please contact digitalcommons@library.tmc.edu.

**DIRECTED EVOLUTION OF MACROCYCLIC PEPTIDES FOR
INHIBITION OF AUTOPHAGY**

by

Joshua Gray B.A.

APPROVED:

Steven Millward, Ph.D.
Advisory Professor

Seth Gammon, Ph.D.

Pratip Bhattacharya, Ph.D.

Richard Wendt, Ph.D.

Robert Bast Jr., M.D.

David Piwnica-Worms, M.D., Ph.D.

APPROVED:

Dean, The University of Texas
MD Anderson Cancer Center UTHealth Graduate School of Biomedical
Sciences

**DIRECTED EVOLUTION OF MACROCYCLIC PEPTIDES FOR
INHIBITION OF AUTOPHAGY**

A

DISSERTATION

Presented to the Faculty of

The University of Texas

MD Anderson Cancer Center UTHealth

Graduate School of Biomedical Sciences

in Partial Fulfillment

of the Requirements

for the Degree of

DOCTOR OF PHILOSOPHY

by

Joshua Gray B.A.
Houston, Texas

August, 2020

ACKNOWLEDGEMENTS

Firstly and foremost I wish to express the deepest gratitude to my adviser, Steven Millward, Ph.D who has been the most exemplary mentor I could have asked for. As a graduate student in the Medical Physics program, my desire to focus my dissertation on a chemical biology project was rather unusual, but Dr. Millward has been an enthusiastic supporter of my interests since I joined his lab for a tutorial research project in 2015. He has taken a profoundly hands-on approach in my training, and has been engaged heavily in the development of my technical and scholarly skills.

I thank the members of my thesis advisory committee; Seth Gammon, Ph.D, Pratip Bhattacharya, Ph.D., Richard Wendt, Ph.D., Robert C. Bast, M.D., and David Piwnica-Worms, M.D., Ph.D., for their support and critical advocacy. I am deeply grateful for all of the ideas and support you have offered me during my dissertation work and for constantly pushing me to refine and improve my experimental design.

I would like to acknowledge all of the members of the Millward lab past and present, and in particular the postdoctoral fellows Lindsay Kelderhouse Ph.D., Argentina Ornelas Ph.D., Brian Engel Ph.D., Brian Grindel Ph.D., and Nasir Uddin Ph.D. who have taught me innumerable skills and helped me troubleshoot and solve countless issues.

I would like to thank all of my current and former colleagues, fellow trainees, and friends in the Department Cancer Systems Imaging, the Graduate School of

Biomedical Sciences, and the Small Animal Imaging Facility for your scientific advice and assistance as well as for some of the greatest friendships I have ever known.

I owe so much to my family and to my partner, Hannah Locke for your love and bedrock of support without which I never could have reached this point. Words do not do justice to describing how much your love and support—personal and professional—means to me.

Lastly I would like to acknowledge the funding support both public and private that made the research in this dissertation possible. This work was sponsored by the National Institutes of Health, the National Cancer Institute, Cancer Prevention, philanthropic support from the Anne and Henry Zarrow Foundation, and generous donations from Stuart and Gaye-Lynn Zarrow, the Mossy Foundation and the Roberson endowment.

Directed Evolution of Cyclic Peptides for Inhibition of Autophagy

Joshua Gray B.A.

Advisory Professor: Steven Millward, Ph.D.

In recent decades it has become increasingly clear that induction of autophagy plays an important role in the development of treatment resistance and dormancy in many cancer types. Chloroquine (CQ) and hydroxychloroquine (HCQ), two autophagy inhibitors in clinical trials, suffer from poor pharmacokinetics and high toxicity at therapeutic dosages. This has prompted intense interest in the development of targeted autophagy inhibitors to re-sensitize disease to treatment with minimal impact on normal tissue. We utilized Scanning Unnatural Protease Resistant (SUPR) mRNA display to develop macrocyclic peptides targeting the autophagy protein LC3. The resulting peptides bound LC3A and LC3B—two essential components of the autophagosome maturation machinery—with mid-nanomolar affinities and disrupted protein-protein interactions (PPIs) between LC3 and its binding partners in vitro. LC3-binding SUPR peptides re-sensitized platinum-resistant ovarian cancer cells to cisplatin treatment and triggered accumulation of the adapter protein p62 suggesting decreased autophagic flux through successful disruption of LC3 PPIs in cell culture. In mouse models of metastatic ovarian cancer, treatment with LC3-binding SUPR peptides and carboplatin substantially reduced tumor growth after four weeks of treatment. These results indicate that SUPR peptide mRNA display can be used to develop cell-penetrating macrocyclic peptides that target and disrupt the intracellular PPIs that govern the autophagic machinery.

TABLE OF CONTENTS

DIRECTED EVOLUTION OF MACROCYCLIC PEPTIDES FOR INHIBITION OF AUTOPHAGY	1
DIRECTED EVOLUTION OF MACROCYCLIC PEPTIDES FOR INHIBITION OF AUTOPHAGY A	2
ACKNOWLEDGEMENTS	3
Directed Evolution of Cyclic Peptides for Inhibition of Autophagy	5
CHAPTER ONE - INTRODUCTION	9
Methods by which molecules cross the cell membrane	12
Passive Diffusion	13
Endocytosis and Macropinocytosis	18
Cyclic peptide screening and cell permeability	25
SUPR peptide selections for autophagy PPIs	30
CHAPTER TWO - DIRECTED EVOLUTION OF CYCLIC PEPTIDES FOR INHIBITION OF AUTOPHAGY	35
Introduction	35
Materials & Methods	39
Cell Lines	39
Expression and Purification of Recombinant LC3	40
Synthesis of N-methyl Alanine amber codon suppressor	41
SUPR mRNA Display Library Preparation	43
mRNA Display Selection	44
Sanger Sequencing	47
Peptide Synthesis and Cyclization	47
Fluorophore Conjugation of SUPR Peptides	49
Biotin Conjugation of SUPR peptides	50
Radiolabeled Binding Assays	50
Fluorescence Polarization Assays	51
Atg4B Activity Assay	52
Proteinase-K Stability Assays	52

ATG8 homologue Selectivity	53
Fluorescence microscopy	54
Cellular Cisplatin Sensitization Assays	55
Cisplatin Sensitization Animal Model	55
Statistical Analysis	56
Results & Discussion	56
Selection against LC3A using MK8 Library	56
Binding affinities of SUPR-4B and variants towards LC3A and LC3B	58
SUPR Peptides Attenuate Atg4b-mediated cleavage of LC3	62
Protease stability is dependent on cyclization and N-methyl incorporation	63
SUPR4B1W Selectivity for LC3 Homologs	65
SUPR4B1W is internalized into cells and co-localizes with punctate LC3 after starvation	66
SUPR peptides sensitize resistant cell lines to cisplatin <i>in vitro</i> .	67
SUPR4B1W sensitizes OVCAR8 tumors to carboplatin in nude mice	70
Conclusions	71
CHAPTER THREE - THE ARHI MODEL OF INDUCIBLE AUTOPHAGY IN OVARIAN CANCER	75
Introduction	75
Materials and Methods	76
Cell Culture	76
Uptake of Mitotracker Red FM by Fluorescence Microscopy	76
Uptake of TMRM and H2DCFDA by Flow Cytometry	77
TOM20 Staining by Flow Cytometry	77
Effect of Autophagy inhibitors on Cellular Viability following ARHI induction	78
Results and Discussion	78
ARHI expression modulates mitochondrial membrane potential & intracellular oxidative state	78
Treatment with SUPR4B1W restores viability following ARHI expression	81
Conclusion	83
CHAPTER FOUR - MULTI-WAVELENGTH PHOTOACOUSTIC VISUALIZATION OF HIGH INTENSITY FOCUSED ULTRASOUND LESIONS	85

Introduction	85
Photoacoustic imaging	86
Current image-guidance methods	88
HIFU guidance with PA imaging	89
	90
Methods	91
Imaging setup	92
Staining procedure	93
2D multi-wavelength PA analysis	94
Creation of tissue characterization maps	94
Image registration and characterization of ablation size	95
Results	97
2D multi-wavelength PA analysis	97
Lesion area statistics	98
Discussion	101
Future work	107
Conclusion	110
Acknowledgements	110
CHAPTER FIVE - CONCLUSION	112
REFERENCES	118
VITA	147

CHAPTER ONE

INTRODUCTION

Traditional drug design has focused primarily on the development of small molecules that occupy a specific region of physiochemical parameters of size ($MW < 500$), hydrogen bond donors ($HBD < 5$), hydrogen bond acceptors ($HBA < 10$) and lipophilicity ($\text{LogP} > 5$) (1). Commonly known as the “rule of 5” (RO5), these parameters of “druglikeness” emphasize the pharmacokinetic properties of oral bioavailability and cell permeability. Targets considered “druggable” (e.g. enzymes) typically have well-defined surface binding pockets that small molecules are able to access with high affinity and selectivity to modulate protein function within minutes to hours following administration. Protein families that inherently modify or interact with small compounds like G protein coupled receptors, nuclear hormone receptors, proteases, phosphatases, and kinases have all historically been amenable to drugging (2). Unfortunately, these easily druggable targets represent a relatively small fraction of target space. Indeed, it is estimated that only ~10% of the human proteome is made up of druggable targets and that only half of those represent useful targets for treating disease (2). As of 2016, only 549 unique human protein targets have FDA-approved small molecule inhibitors (3). The overwhelming majority of disease-related protein activities are considered undruggable as their critical interactions occur through interfaces of large protein surfaces ($750\text{-}1500 \text{ \AA}^2$) that druglike small molecules simply lack the size to efficiently disrupt (4).

Biologics (e.g. monoclonal antibodies and their variations) have seen development increase dramatically over the last two decades due to the ability of

these large compounds (~5-150 kDa) to inhibit protein-protein interactions (PPIs) by binding to large surface areas on targets with extremely high affinity and specificity. This class of compound however is inherently restricted to targeting extracellular proteins as the size of antibodies prevents them from crossing the cell membrane and accessing intracellular protein targets. Although antibodies possess the requisite affinity and target selectivity for disrupting extracellular PPIs, their high cost of production and chemical instability complicates their translation from the bench to the clinic.

Peptides occupy an important intermediate chemical space between small molecules and biologics that strongly positions them to become powerful therapeutic inhibitors of intracellular PPIs. With typical sizes between 5-30 AAs (~500-3500 Da), peptides possess sufficient surface area to achieve antibody-like binding to protein surfaces and inhibition of PPIs without becoming too large to categorically prohibit cell uptake. Protein interactions with peptides of 5-10 amino acids typically have a shared surface area $>400 \text{ \AA}^2$ (5) which is thought to be sufficient for effective disruption of most PPIs. Historically, peptides have been dismissed as potential drug candidates due to a number of factors including susceptibility to proteolysis, lack of inherent cell permeability, and challenging library screening procedures. As we will see, cyclization and N-methylation of the peptide backbone provide answers to many of the cell permeability and serum stability issues inherent to using peptides as drugs against intracellular targets. Combined with recent advances in rapid screening and directed evolution technologies, cyclic peptides have enormous

potential to become a preferred molecular scaffold for the inhibition of intracellular PPIs.

Scanning Unnatural Protease Resistant (SUPR) peptide mRNA display is a relatively recent advancement of the original mRNA display technology developed by Roberts and Stzosak that introduces macrocyclization, N-methyl amino acid incorporation, and protease screening (6). In this manner, libraries of trillions of unique compounds can be screened to produce cyclic peptide scaffolds that not only have superb affinity and selectivity for the target protein of interest, but are also nearly completely resistant to proteolytic degradation. Cyclization, serves two purposes in the SUPR peptide architecture. On one level, cyclization serves to constrain the three dimensional conformation of peptides, potentially freezing them in an active, target-binding state (7–9). Cyclization has also been shown to increase resistance to proteolytic degradation, possibly through increased conformational rigidity (10,11). The incorporation of N-methyl amino acids has been shown by many investigators to drive proteolytic stability by introducing tertiary amides in the backbone (11,12). Indeed, the incorporation of a single N-methyl amino acid has been shown to provide protection against proteolysis that extends several residues on either side of the incorporation site (13).

My work is based on the hypothesis that several of the characteristics that define the SUPR peptide architecture will also impart cell permeability. In the following sections, I will lay out some of the principles of cell permeability and the requisite physicochemical properties required to impart cell permeability to peptides. I will briefly review the growing field of cell permeable cyclic peptides with particularly

emphasis on the features of cell permeability that overlap with those found in SUPR peptides. I will provide an overview of mRNA Display and SUPR mRNA display as well as a brief discussion of autophagy and the role of protein-protein interactions in this process. Finally, I will introduce the LC3 protein, its PPIs, and its role as a target for SUPR peptide mRNA Display.

Methods by which molecules cross the cell membrane

Cellular plasma membranes are made up of a complex network of phospholipids arranged in a bilayer which protects the cell from its environment. The lipids that comprise the cell membrane consist of strongly hydrophilic head group attached to a hydrophobic lipid chain. These lipids are arranged in a double layer with the head groups exposed to the cell interior and exterior which isolates the hydrophobic lipid tails from the aqueous intracellular and extracellular environments (14). This arrangement creates a superb barrier between the extracellular space and the cell interior that is impermeable to all but a select few compounds. Internalization of molecules primarily occurs through three pathways: passive diffusion of moderately polar small molecules driven by a concentration gradient; endocytosis, the process of internalizing compounds adhered to the cell surface in vesicles made up of portions of the cell membrane; and active transport of molecules in a highly specific manner by ATP-activated protein transporters embedded in the surface of the cell membrane (15). With the exception of some classes of peptides that are actively transported, most peptides typically access the cytosol through passive diffusion or endocytosis. Some small di- and tri-peptides are actively transported by the proton-coupled oligopeptide transporter (SLC15) family of membrane transport

proteins (16,17) and some moderately sized (~8 residues) naturally occurring bicyclic peptides actively transported by the organic anion transporter polypeptide (OATP) family of transport proteins (18,19). As we will see, linear peptides lack many of the features that characterize highly cell permeable compounds. Significant modification—such as cyclization and incorporation of non-proteogenic amino acids—is typically required to achieve efficient entry into the cytosol.

Passive Diffusion

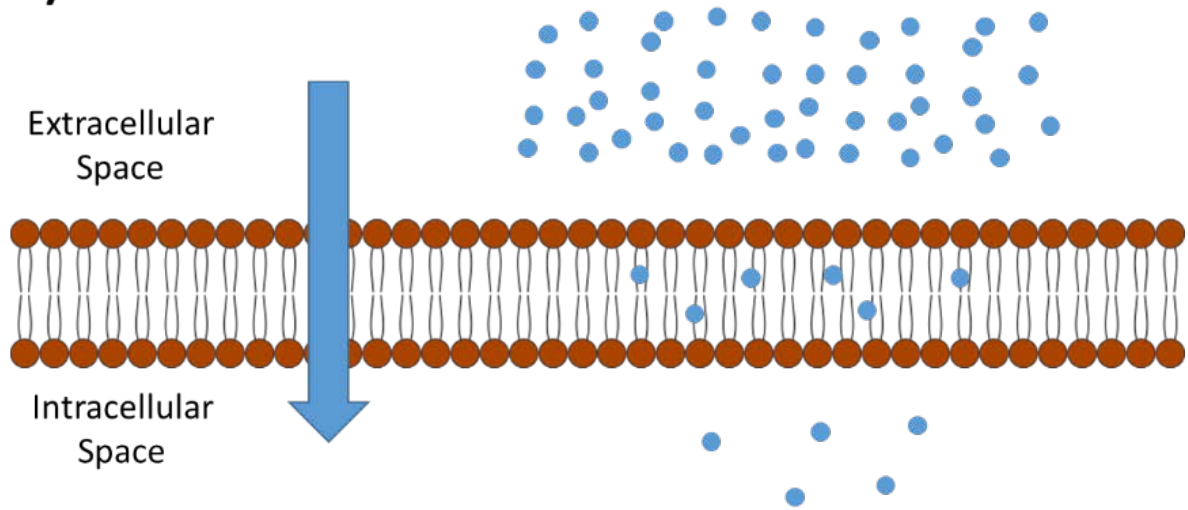
Small, moderately polar molecules are among the few classes of compounds that are able to passively cross the cell membrane in an energy-independent manner (**Figure 1A**). Membrane transit from the aqueous environment of the extracellular space to the aqueous environment of the cytosol occurs in three steps. The molecule first partitions into the outer hydrophilic membrane surface, then transits the inner hydrophobic membrane core, and finally exits the inner membrane surface to access cell interior (20). Passive transport across the cellular membrane is driven by a concentration gradient across the membrane and therefore—ignoring any energetic costs of establishing the gradient—is an energy-independent process. The rate of diffusion across plasma membranes can be modeled simply by the derivation of Fick's first law (15):

$$\frac{dM}{dt} = \frac{k_f \times S \times \Delta C(t)}{d \times MW^{1/2}}$$

Where dM/dt is the rate of transfer of compound across the membrane, k_f is the compound's membrane-water partition coefficient, S describes the surface area of the membrane, $\Delta C(t)$ describes the concentration gradient across the membrane, d

describes the thickness of the membrane, and $MW^{1/2}$ is the square root of the molecular weight. The MW and k_f are the two physical properties of the *compound* that define its ability to cross lipid bilayers. The membrane-water partition coefficient is the ratio of the concentration of a solute in water and in lipid (such as octanol) when the two solvents are mixed and it is one measure of compound lipophilicity. Transit across membranes is directly proportional to k_f , therefore strongly lipophilic compounds should more readily transit the hydrophobic membrane interior. Additional modeling studies have (20) identified desolvation as a critical aspect to initiation of partitioning of the membrane and that energy of desolvation strongly affects rate of transit across the membrane. Effectively this means that more lipophilic compounds pay a lower desolvation penalty when transitioning into the membrane interior. Druglike compounds are rarely strongly hydrophobic however, due to issues of solubility in the aqueous extracellular and intracellular environments. Successful therapeutic compounds must possess a delicate balance of hydrophobicity to drive cellular internalizations and hydrophilicity to maintain solubility. The rate of transfer is also inversely proportional to the MW of the compound meaning that smaller molecules will more readily diffuse across cell membranes than larger molecules. If one plots this equation, it quickly becomes clear that the contribution of MW to permeability rapidly becomes asymptotic and above 400 Da the permeability penalties imposed by increasing MW effectively saturate. At this point, the equation is heavily dominated by k_f and ΔC .

A) Passive Diffusion



B) Endocytosis

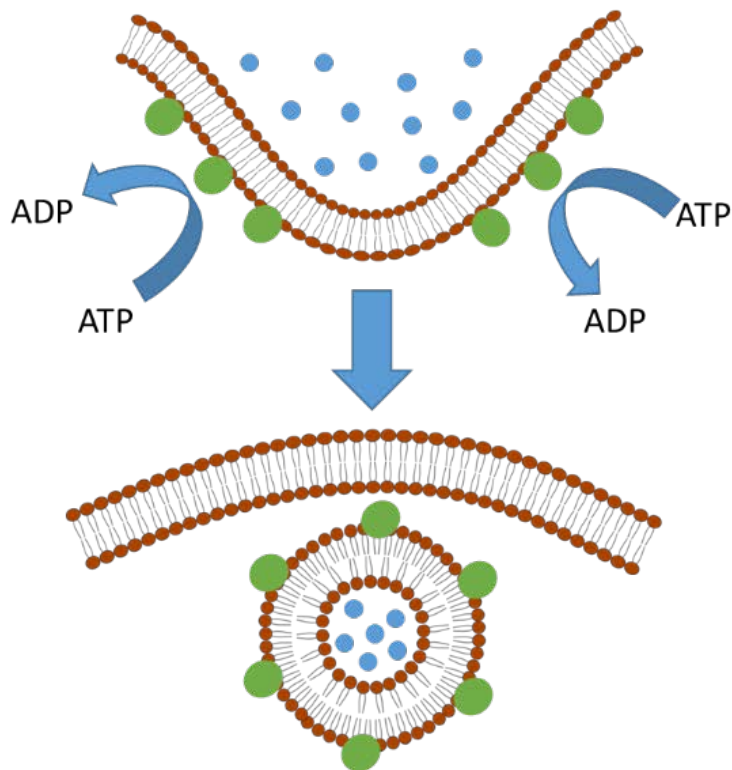


Figure 1: Diffusion and Endocytosis. A) Passive diffusion of molecules across the cell membrane is driven by a concentration gradient. Small, moderately polar molecules partition the outer membrane, diffuse through the membrane interior and access the cytosol. B) Endocytotic invagination of the cell membrane expends energy in the form of ATP to internalize compounds by pinching off portions of the membrane to form internal vesicles that are trafficked to various cellular compartments.

When we consider the Rules of 5 (RO5) for “druglike” compounds capable of passive permeation discussed earlier, it becomes readily apparent that most peptides—including cyclic peptides—are profoundly *non*-druglike. The RO5 provide convenient, easy to remember guidelines that predict whether a compound is likely to have acceptable passive permeability and oral bioavailability. With an average molecular weight of approximately 110 Da per amino acid, cyclic peptides begin to push the size boundaries of druglikeness in as few as five residues. On top of this fact, each peptide bond contributes 1 hydrogen bond donor (HBD) and 2 hydrogen bond acceptors (HBAs) before consideration of the chemical composition of the amino acid side chains. Based on these two factors, the RO5 guidelines predict that both cyclic and linear peptides containing 5 or more amino acids should not be cell permeable by passive diffusion.

For the most part this prediction is accurate, though there are notable exceptions in which cyclic peptides—both naturally occurring and synthetic—readily diffuse through the cell membrane. A key feature commonly found passively permeable cyclic peptides is the elimination of backbone HBDs through N^α-methylation of backbone amines and extensive intramolecular hydrogen bonding (15,21). Hydrogen bonds between backbone amide protons and water typically have a free energy of around 1 kcal/mol which is imposed as a desolvation penalty that must be paid when partitioning the membrane (22,23). Incorporation of N-methylation and intramolecular hydrogen bonds reduces the number of uncapped polar N-H groups in the peptide backbone that would require desolvation in order to achieve diffusion into the hydrophobic membrane interior (24). The inclusion of at

least one depsipeptide linkage has also been shown to contribute to passive permeability in a similar manner to N-methylation (21) as the replacement of an amide group in the peptide backbone with an ester linkage eliminates an HBD. However, the introduction of ester bonds in the backbone may impair the translatability of depsipeptides into effective clinical therapeutics due to serum stability issues introduced by susceptibility to ester hydrolysis. Stability studies of cyclic lipodepsipeptides in human serum revealed that ~65% of lipodepsipeptide was degraded in 24 hours—primarily due to hydrolysis of the ester bond—compared to no significant degradation of the control peptide which contained only amide backbone bonds (25).

Small tetramer and pentamer cyclic peptides and depsipeptides such as tentoxin and romidepsin largely obey the RO5 size restrictions and also reduce HBD load through N-methylation, depsipeptide linkages, and intramolecular hydrogen bonding (21,26,27). The most prominent example of a large cyclic peptide that passively permeates the cell membrane is Cyclosporine A (CsA), an 11-mer cyclic peptide immunosuppressant that possesses both excellent oral bioavailability and cell permeability despite violating the RO5 guidelines on size and HBD/HBAs (**Figure 2A**)(28). CsA contains 7 N-methyl amino acids and can undergo a significant conformational shift to reduce the number of backbone HBDs exposed to solvent. In aqueous environments, CsA adopts an “open” conformation which allows its backbone amides to interact with water molecules or its intracellular target, cyclophilin. When entering the cell membrane, CsA adopts a “closed” conformation in which all of its backbone amides that are not N-methylated participate in

intramolecular hydrogen bonds which dramatically reduces its polar surface area (29). Interestingly, Cyclosporine E (CsE)—a variant of CsA that lacks N-methylation of Val11—does not completely deplete HBDs in the peptide backbone and conformational changes occur at a 10-fold slower rate than CsA. This results in dramatically reduced cellular permeability and highlights the extent to which desolvation penalties drive membrane permeability by passive diffusion (29). Other large cyclic peptides such as enniatin B, patellamide C, and the PF1171 family of peptides that exhibit strong passive permeability all completely deplete backbone HBDs through a combination of N-methylation and intramolecular hydrogen bonding (21,30).

Endocytosis and Macropinocytosis

Endocytosis is the process of internalizing membrane proteins, lipids, and extracellular molecules from the exterior surface of the cell by invaginating the cell membrane and forming an internal vesicle (**Figure 1B**)(31). Once internalized the vesicle is transported to intracellular compartments (i.e. lysosomal or golgi compartments) for downstream processing. While clathrin-mediated endocytosis has been studied extensively in the literature (32), other mechanisms of receptor-mediated endocytic uptake that do not rely on clathrin remain fairly poorly understood.

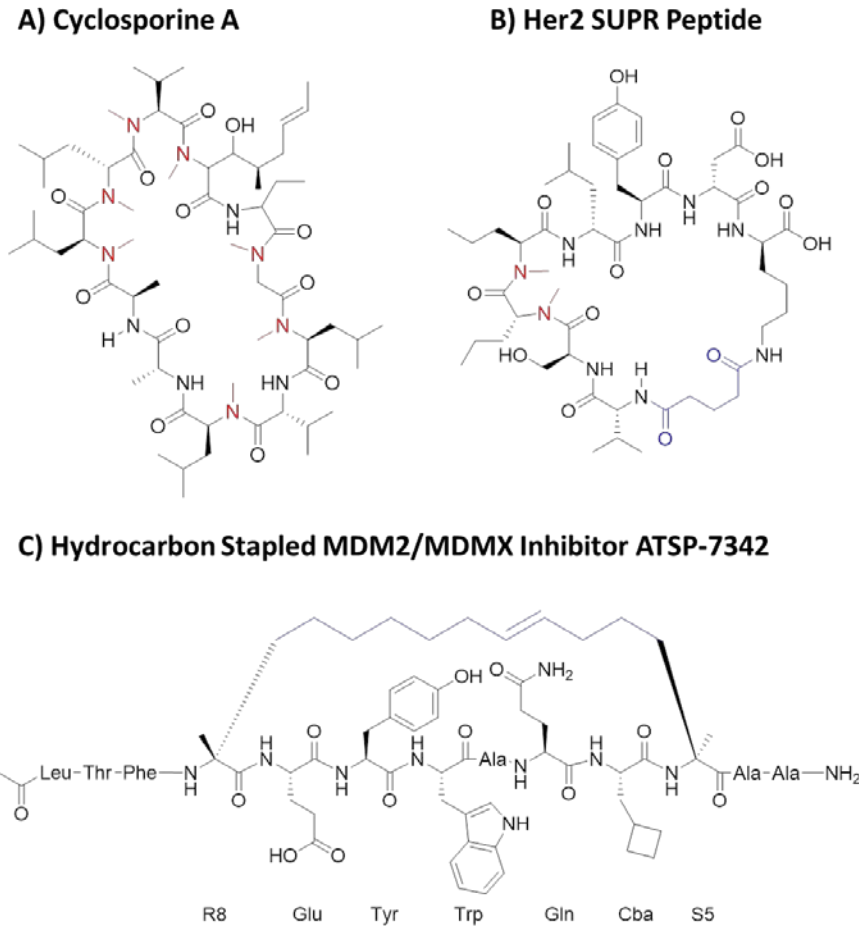


Figure 2: Examples of various constrained cyclic peptides. **A)** Cyclosporine A, a naturally occurring 11mer peptide contains 7 N-methylated backbone residues (red) and can undergo a conformational shift, forming extensively internal hydrogen bonds in the peptide backbone allowing it to passively diffuse through the hydrophobic membrane interior. **B)** An example SUPR peptide produced by a selection against HER2 (Fiacco 2016). SUPR peptide mRNA display produces cyclic peptides that combine both N-methylation (red) and macrocyclization through a hydrophobic crosslinker (blue) which may impart intrinsic cell permeability. **C)** Example stapled peptide ATSP-7342, this peptide utilizes a hydrophobic crosslinker to enforce α -helical structure. ATSP-7342 efficiently accesses the cytosol through endocytosis and inhibits MDM2/MDMX PPIs. The presence of a hydrocarbon staple appears to be critical for cell permeability. A modified version of this stapled peptide (ALRN-6924) is currently in Phase-II clinical trials for the treatment of several types of cancer.

Macropinocytosis represents one of the more well-studied forms of non-clathrin-mediated endocytosis. Unlike endocytosis which proceeds through invagination of the membrane, micropinocytosis involves the formation of large vesicles through the actin-mediated extension of membrane folds called ruffles outwards from the

cell surface (33,34). Activation of membrane growth factor receptors such as EGFR is known to initiate membrane ruffling and, as a consequence, highly elevated macropinocytic activity is often observed in cancer cells that overexpress growth factor receptors (35). Macropinocytosis is non-selective in its cargo uptake and its

vesicles are typically much larger than other endosomal vesicles. Despite this, macropinocytotic vesicles undergo very similar processing through the endosomal and lysosomal compartments (36).

Both receptor-mediated endocytosis and macropinocytosis are subjects of interest as tools for delivering exogenous compounds to the cell interior, particularly in the case of large molecules and nanomaterials that cannot access the cell interior through passive diffusion or active transport (37). Macropinocytosis in particular has been studied extensively as a mechanism to deliver therapeutics semi-specifically to cancer cells, due to the tendency of these cells to be highly macropinocytotic by virtue of growth factor receptor overexpression (36). It is currently believed that cytosolic access following endosomal or macropinocytotic uptake is limited primarily by escape from the endosome interior rather than initial uptake efficiency.

The discovery in the early 1990s of two peptides—the transactivator of transcription domain of HIV (TAT, GRKKRRQRRRPQ) and Antennapedia homeodomain of *Drosophila* (penetratin, RQIKIWFQNRRMKWKK)—which were found to cross the cell membrane through endocytic uptake initiated the study of so-called cell-penetrating peptides (CPPs)(38,39). This class of heavily cationic and amphipathic peptides are readily taken up into the cell by endocytosis and subsequently escape the endosomal vesicles to access the cytosolic milieu. As of early 2020, more than 1700 unique peptide sequences have been classified as CPPs according to CPPsite 2.0, a database that tracks CPPs in the literature (40). While the exact mechanisms by which CPPs access the cytosol remains a topic of debate, it is consensus agreement that internalization of CPPs occurs through

endosomal uptake initiated by association with the outer plasma membrane. Cationic CPPs such as TAT and polyarginine depend on coulombic interactions between the positively charged side-chains of basic amino acids—primarily arginine and lysine—and the negatively charged surfaces of cellular membrane (41,42). It has also been established that the association of the guanidinium sidechains of arginine with heparan sulfate drives initiation of endocytosis, providing evidence that CPPs are active initiators of endocytosis. Uptake of these peptides by endocytosis may also benefit from normal membrane recycling activities (43,44). Like cationic CPPs such as TAT, amphipathic peptides such as penetratin and RW9 (RRWWRRWRR) form hydrogen bond associations with the surface of the outer cell membrane but also undergo hydrophobic interactions via sequestration of aromatic side-chain residues into the lipid bilayer (45,46).

Following internalization of the endosome, CPPs must escape from the endosomal-lysosomal compartment. While it has been established that CPPs do escape endosomes, escape efficiency for linear CPPs is generally very poor and the vast majority of linear CPPs remain trapped in the endosome and are eventually degraded without ever gaining access to the cytosol (15). Proposed mechanisms of escape have been poorly studied until very recently and evidence supporting hypothesized mechanisms of endosomal escape remains sparse. One of the more prominent theories of endosomal escape posits that the CPP associates with the interior surface of the endosome as it matures and acidifies, generating transient toroidal or barrel stave pores in the membrane through which the CPP escapes by diffusion into the cytosol (47,48). However, this model cannot fully explain why some

CPPs are able to facilitate the transport of large macromolecules (e.g. nucleic acids and nanoparticles) out of endosomes (49,50).

Until very recently, CPP research has focused nearly entirely on linear peptides. According to CPPSite 2.0, a database that tracks the CPP literature, nearly 95% of unique CPP sequences are linear peptides (40). The uptake efficiency of linear CPPs—defined as the concentration of peptide in the cytosol versus the extracellular concentration—ranges from 0.2-4.0%. This low rate of uptake is thought to be driven largely by poor endosomal escape rather than by inefficient endosomal loading (51). Cyclic CPPs, on the other hand, have demonstrated the potential for significantly higher uptake efficiencies—in some cases more than two orders of magnitude higher—than those observed in linear CPPs. Studies of cyclized variants of TAT, polyarginine, amphipathic polarginine peptides incorporating tryptophan groups, and many other cyclic CPPs have demonstrated several-fold higher uptake rates in cyclic variants of the peptide compared to linear formulations (52–54). The Pei group has designed a family of amphipathic, cyclic nona-peptides combining two aromatic, hydrophobic residues (phenylalanine, 2-naphthylalanine) and four arginine residues that have achieved cytosolic delivery efficiencies between 20-120%—as much as 2 orders of magnitude greater than linear TAT—and show evidence of delivering large macromolecules and fluorescent proteins to the cytosol with similar efficiency (55–57). Interestingly these molecules appear to escape from early endosomes rather than late endosomes as TAT most other linear CPPs do.

The combination of conformational stabilization through macrocyclization and amphipathicity seem to be critical physiochemical features that drive efficient access

to the cytosol by CPPs. A potential explanation for this phenomenon may be that the bottleneck for cytosolic access lies in endosomal escape rather than initial endosomal uptake; traditional cationic CPPs like TAT appear to have similar initial endosomal uptake to cyclic, amphipathic CPPs despite dramatically lower cytosolic access efficiencies (15). It has been proposed that pore formation in endosomes requires association with the inner endosomal membrane by cationic guanidinium groups and simultaneous, orthogonal insertion of hydrophobic side chains into the membrane (57). The enhanced backbone rigidity enforced by macrocyclization or hydrocarbon stapling may reduce conformational entropy and cause amphipathic cyclic peptides to more consistently adopt conformations capable of achieving both hydrophilic and hydrophobic interactions with the endosomal membrane than linear, cationic and amphipathic CPPs can achieve. This implies that the conformational restrictions required for endosomal release may be different from those required for target engagement. Thus, CPPs are perhaps best employed as cell delivery vectors rather than as a component of a target-binding scaffold.

While eminently useful for basic research and chemical biology applications, the highly cationic nature of CPPs has proved a sizeable hurdle to their translation into clinical use. *In vivo* biodistribution studies of common CPPs like TAT, penetratin, and polyarginine reveal that these compounds initially bind strongly to the vasculature local to the site of administration followed by rapid clearance through the liver. In some cases, 90% liver uptake was observed in as little as 30 minutes (58,59). This rapid accumulation of compound in the liver is known to be associated with acute liver toxicity at clinically relevant doses (58). Despite these issues that

impair the ability to translate CPPs into clinical use, they have contributed expansively to the understanding of how to design therapeutic peptides with enhanced cell permeability.

There is evidence that stapled peptides—a special class of cyclic peptides in which the side chains of the i , $i+4$ or i , $i+7$ residues are crosslinked with a hydrocarbon linker to enhance α -helical structure and increase protease resistance—are cell permeable at least in part through endosomal uptake and escape. Hydrocarbon stapling typically occurs between the $i,i+4$ or $i,i+7$ residues because these spacings correspond to one or two α -helical turns respectively (60). Bridging the side-chains at these positions with a hydrophobic crosslinker significantly reinforces the α -helical structure of the macromolecule. An exhaustive study by Verdine and colleagues on the uptake mechanisms of over 200 hydrocarbon stapled peptides and CPPs found that cell permeability was correlated with formal positive charge and that cellular uptake was abrogated in CHO cells deficient in sulfated proteoglycans (61). Their studies suggest that hydrocarbon stapled peptides access the cytosol primarily through clathrin/claveolin-independent endocytosis triggered by association with negatively charged membrane components, similar to traditional cationic and amphipathic CPPs. Uptake efficiency was also found to correlate strongly with the extent of helical stabilization. When stapled in different locations, a peptide derived from the BH3 domain of the BID apoptotic effector protein exhibited differing levels of α -helicity by circular dichroism (CD) spectroscopy and significantly lower endosomal uptake was associated with peptide variants that had less-stabilized helical structure (62). Several stapled

peptides have been shown to be successful at crossing the cell membrane to disrupt PPIs, most notably in the case of inhibitors of the MDM2/MDM4:p53 interaction. ALRN-6924—a stapled peptide mimetic of the MDM2/MDM4 binding region of p53—efficiently permeates cell membranes to mediate its effect on MDM2/MDM4 and is currently in phase 2 clinical trials for the treatment of T-cell lymphoma (**Figure 2C**)(63,64). Several other intracellular PPIs have been successfully targeted using stapled peptides, including the NOTCH transcription factor complex (65), Wnt signaling through β -catenin (66), and the PRC2 complex (67). However, it should be noted that only a small subset of stapled peptides are cell permeable and that endosomal escape remains a challenge for this class of molecules.

Cyclic peptide screening and cell permeability

mRNA display is an *in vitro* directed evolution method developed by Roberts and Stzosak to screen libraries of randomized peptides for desired properties (e.g. binding to a target) by forming a covalent link between each peptide and its encoding mRNA (68). This allows functional molecules to be rapidly identified by DNA sequencing following selection. As a method, mRNA display has significant advantages over older biological display methods such as phage or yeast display since the size of the library is not limited by the transformation efficiency of the host organism. mRNA display libraries can reach sizes $>10^{15}$ unique sequences while phage display libraries are orders of magnitude smaller ($\sim 10^{11}$ unique sequences)(69). Post-translational chemical modification of mRNA Display libraries can also be carried out without concern for the molecular surface, greatly expanding the potential chemical complexity of the library. Compared to ribosome display,

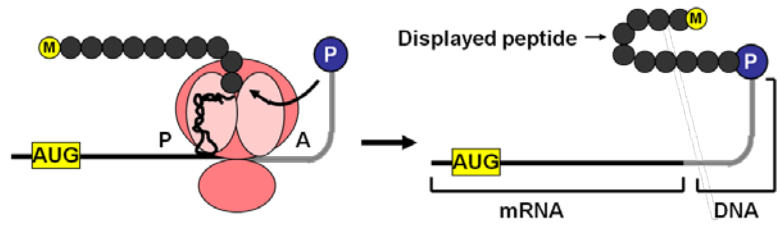
mRNA display suffers far fewer confounding effects from the surface on which the peptide is displayed (70). Since its invention, mRNA display has been used to design numerous high affinity peptides for targets such as G-protein coupled receptors (8), boxB RNA (71), and PDL-1 (72) among many others.

Extensions of the technology to evolve large macromolecules

like fibronectin (73) and single-chain antibodies (74) have also been achieved.

The process of an mRNA display selection begins with the design of a randomized dsDNA library. Libraries can be either totally naïve or a partial randomization of an existing sequence and as many as twelve codons can be fully randomized ($>10^{15}$ unique sequences) with complete library coverage before issues of translation scale arise. After assembly, the dsDNA library is transcribed to mRNA *in vitro* and ligated to puromycin by a poly-dA linker. Puromycin acts as an

A) mRNA-peptide fusion



B) Selection of LC3-binding SUPR Peptides

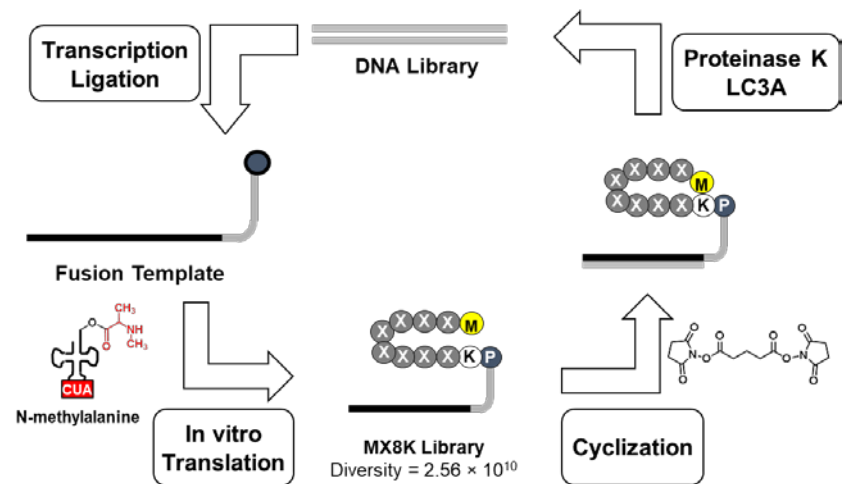


Figure 3: mRNA Display and SUPR mRNA Display. A) Diagram of mRNA-peptide fusion. During translation of the ligated mRNA, puromycin can enter the active site of the ribosome to form a covalent amide linkage between the peptide and its encoding genetic information. B) SUPR peptide mRNA display selection scheme outlining the steps performed in a round of SUPR selection, in this case against the target LC3A

aminoacyl-tRNA mimetic; during *in vitro* translation of the library it can enter the active site of the ribosome and cause the ribosome to stall. Subsequent amide bond formation between the primary amine of puromycin and the C-terminus of the growing peptide yields a covalent linkage between the translated peptide and its encoding mRNA (**Figure 3A**). The ligated mRNA libraries are translated *in vitro* using rabbit reticulocyte lysate depleted of endogenous mRNA. Following translation the mRNA-peptide fusions can be purified from the translation mixture using a poly-dT resin that associates with the poly-dA linker between the peptide and its conjugated mRNA (75). Purified mRNA-peptide fusions are typically reverse transcribed to form an mRNA-DNA duplex to stabilize the genetic information and prevent inadvertent selection of aptamers. The resulting peptide-DNA-RNA conjugates are then screened against an immobilized target protein for binding. Following extensive washing to remove non-functional sequences, PCR is performed to amplify the genetic information of peptide sequences which bind strongly to the target. This yields an enriched library of dsDNA that serves as the basis for the next round's library. From here the process of selection can be repeated as many times as necessary for the library to converge (typically 5-7 rounds) at which point the final pool can be sequenced to identify candidates for further investigation.

While an eminently powerful tool for identifying peptide sequences that bind to target proteins with antibody-like affinities and specificity, the products of mRNA display selections suffer from all the traditional liabilities associated with linear peptides. Linear peptides are often disordered which impairs binding affinity and

imparts susceptibility to enzymatic hydrolysis in the face of serum and intracellular proteases. Linear peptides are almost always non-cell permeable further reducing their potential for translation. **Scanning Unnatural Protease Resistant (SUPR)** peptide mRNA display represents an advancement on the original mRNA display technology which aims to solve the issues of conformational entropy and protease susceptibility (**Figure 2B**). During SUPR peptide mRNA display selections, amber codon nonsense suppression is utilized during *in vitro* translation to facilitate incorporation of a single non-proteogenic amino acid into translated peptides. While any non-proteogenic amino acid may be chosen, N-methylated amino acids such as N-methyl-L-alanine or N-methyl-L-norvaline are commonly selected to increase resistance to proteases (11). In addition to unnatural amino acid incorporation, SUPR peptide mRNA display employs macrocyclization to reduce conformational entropy and improve stability. A common method to cyclize peptides involves designing the SUPR peptide libraries with a locked C-terminal lysine immediately adjacent to the randomized region. Macrocyclization can then be readily achieved between the sidechain of lysine and the N-terminus of the peptide using an amine-reactive crosslinker such as disuccinimidyl glutarate (DSG) using N-hydroxysuccinimide ester chemistry (8,76). As a final modification of the mRNA display selection procedure, SUPR peptide mRNA display selections will typically incorporate an additional selection pressure for protease resistance by incubating the cyclized mRNA-peptide fusion library with strong protease—such as proteinase-K—immediately prior to each round of binding selection (**Figure 3B**). These strategies tend to produce hits that not only have high affinity and selectivity for the

target protein of interest, but also superb protease stability. Selected peptides are frequently observed to incorporate multiple N-methyl amino acids resulting in biological half-lives on the order of weeks in human serum (*ex vivo*)(11).

While designed to produce serum-stable peptides that bind targets with antibody-like affinities, the strategies employed by SUPR peptide mRNA display produce peptides that possess many of the features thought to convey cell permeability. As we have discussed already, the combination of N-methylation of the peptide backbone and cyclization of peptides with a hydrophobic cross-linker has been shown to dramatically improve the intrinsic cell permeability of peptides. Macrocyclization-promoted formation of intramolecular hydrogen bonding and N-methylation of the peptide backbone reduce the number of solvent accessible HBDs in the peptide backbone which reduces the desolvation penalty the peptide pays to associate with the outer surface of the cell membrane, an essential first step to both passive diffusion and endocytosis. Hydrocarbon stapling utilizes a hydrophobic crosslinker between the sidechains of the $i, i+4$ residues of peptides to enforce α -helicity and it has been shown that endosomal uptake and escape efficiencies of stapled peptides are dependent on the extent of helix stabilization induced by the staple (62). The DSG crosslinker utilized in SUPR mRNA display selections is chemically similar to the hydrocarbon bridges in stapled peptides and may convey similar properties of improved endosomal uptake by structural stabilization.

SUPR peptides may be ideal scaffolds for inhibiting intracellular disease-generating PPIs. The directed evolution technology is highly efficient in generating macrocyclic peptides that bind targets with antibody-like affinity, specificity and

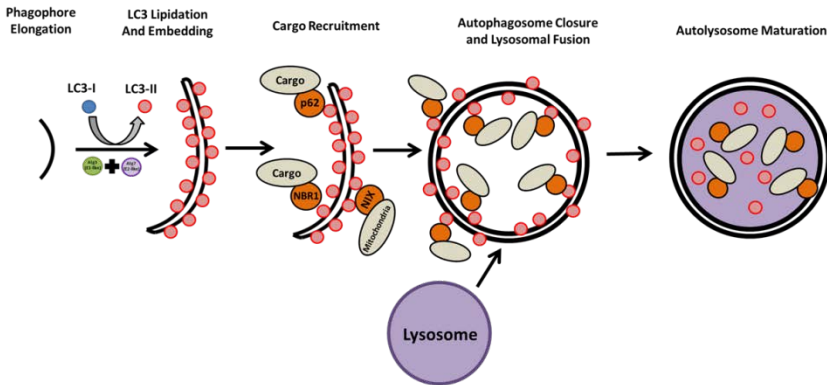
sufficient surface area to disrupt PPIs while remaining highly resistant to serum proteases. SUPR peptide sizes (~1200-2000 Da) are not too large to be endocytosed and the combination of macrocyclization and backbone N-methylation conveys many of the properties characteristic of peptides that undergo highly efficient endosomal uptake and escape into the cytosol.

SUPR peptide selections for autophagy PPIs

Macroautophagy, or simply autophagy, is a catabolic, bulk-degradation cellular housekeeping process that may provide an ideal target for the development of cell-permeable SUPR peptide PPI inhibitors. Autophagy is mediated by highly conserved molecular machinery that typically operates at a low basal level and is dramatically upregulated in response to cellular stress such as nutrient deprivation (77,78). Upon initiation of autophagy signaling, isolation membranes in the cytosol originating from the endoplasmic reticulum are expanded, eventually forming double-membrane vesicles called autophagosomes. These autophagosomes encapsulate portions of the cytosol containing proteins and organelles during their expansion, and prior to closure, a number of autophagy adaptor proteins transport damaged or superfluous proteins and organelles to the autophagosome interior. The mature, closed, autophagosome eventually fuses with the lysosome—forming a vesicle called the autolysosome—and hydrolytic lysosomal proteases degrade the contents of the vesicle to monomers which are used for downstream metabolism. In this manner autophagy lives up to the literal translation of its name: self-eating. Internal components of the cell are broken down into basic metabolites to fuel essential processes (**Figure 4A**).

As an adaptive stress response, autophagy allows cells to survive transient periods of stress. Basal autophagic flux is slow, but can be rapidly upregulated to break down nonessential cellular machinery during periods when the cell cannot acquire sufficient nutrients from its environment. Like many processes necessary for cellular health, autophagy can be co-opted by disease. Many types of cancer—including ovarian (79,80), breast (81,82), esophageal (83), colon (84), and pancreatic (85–87)—constitutively activate autophagy far above basal levels in order to survive the nutrient deprived conditions imposed on the developing tumor microenvironment by poor and dysregulated vasculature. Additionally, autophagy is known to be upregulated in response to internalization of cytotoxic agents or extreme internal stress such as can be caused by radiation-induced DNA damage and free radical generation. Many cancers will activate autophagy in response to chemotherapeutics (83,88–90) and radiation (91–93)—particularly, recurrent, metastatic disease that has been treated previously. Because of this, there is significant clinical interest in inhibitors of autophagy as an adjuvant to increase or restore the effectiveness frontline chemotherapeutics and radiation. Chloroquine and hydroxychloroquine have been investigated exhaustively in combination with stand-of-care cancer therapies. Unfortunately, these compounds don't specifically target autophagy. Rather, they are non-specific lysosomotropic agents which impair the function of lysosomes by raising lysosomal pH and inhibiting the activity of lysosomal enzymes. As a consequence, chloroquine and hydroxychloroquine incur unacceptably high levels of normal tissue toxicity at therapeutically relevant doses. While the toxicity of CQ and HCQ have recently come to the attention of the public

A) Autophagy machinery



B) LC3-interacting motif

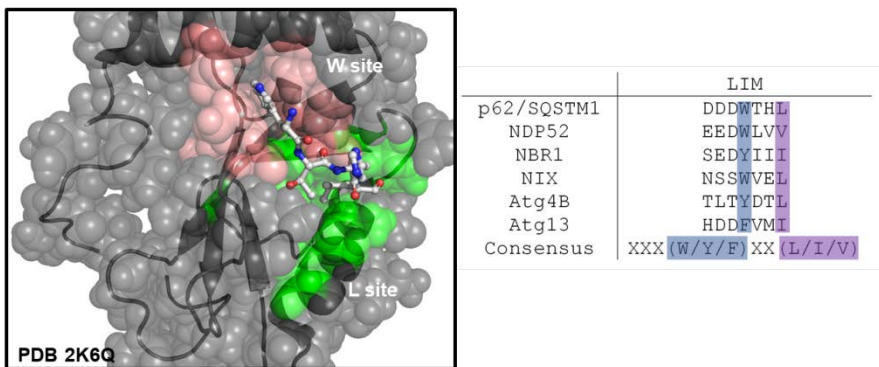


Figure 4: The autophagy machinery and the role of LC3. **A)** Diagram of the autophagy machinery. Following initiation of autophagy, LC3 is lipidated and embedded in the autophagosomal surface where it facilitates cargo recruitment and closure of the autophagosome. **B)** LC3 PPIs are mediated by a consensus amino acid motif in its binding partners that recognizes two hydrophobic binding pockets on the surface of LC3 shown here in red (W-site) and green (L-site). This hot spot is recognized by LC3-interacting motifs (LIMs) which contain the consensus sequence W/Y/F-XX-L/I/V. We hypothesized that SUPR mRNA display could generate cell permeable macrocyclic peptides that recapitulate this motif and effectively inhibit LC3 PPIs.

autophagy machinery itself. These compounds would block only the PPIs relevant to the normal functioning of the autophagic machinery without inducing significant toxicity in healthy cells.

We hypothesized that SUPR peptides might be the ideal class of compounds to inhibit the autophagy machinery in a targeted manner. While the signaling, initiation, and maturation of autophagosomes is a complex process that involves hundreds of PPIs, one particular family of proteins stands out as a crucial element.

as a result of the SARS-CoV-2 epidemic (94), the toxic effects of CQ and HCQ have long been understood. Therapeutically relevant doses can lead to rapid onset of retinopathy (95,96), hypotension, and potentially fatal ventricular tachycardia (97). What is needed are inhibitors of the

Microtubule-associated protein light-chain 3 (LC3) is a small 14 kDa protein built around a ubiquitin core that plays an essential role in the maturation of autophagosomes and transport of cargo into their interior. Following translation, LC3 is acted upon by the autophagy-related protein Atg4 which cleaves the C-terminus of LC3 to expose a glycine residue (LC3-I). When autophagy is initiated, LC3-I is modified by a series of protein complexes in an E1- and E2-like manner to conjugate the membrane lipid phosphatidylethanolamine (PE) to its newly exposed C-terminal glycine residue (LC3-II). LC3-II is then embedded in the interior and exterior surfaces of the nascent autophagosome membrane where it plays an essential role in the expansion and closure of the autophagosome. Additionally, both during and following the closure of the autophagosome, LC3 is heavily involved in the recruitment of cargo to the autophagosome interior. Many autophagy related cargo adapter proteins—such as p62 (SQSTM1), NIX, NBR1, and NDP52—transport organelles, proteins, and protein aggregates to the vicinity of the autophagosome and then interact with LC3 to transport their cargo to the autophagosome interior (98). The vast majority of LC3's PPIs—including those associated with cargo adapter proteins and the protein machinery that post-translationally modifies and lipidates LC3—occur via a “hot spot” on the surface of LC3 made up of two hydrophobic binding pockets. These two binding pockets recognize a common amino acid motif of (W/F/Y)-XX-(L/I/V) where X can represent any amino acid (99–101). This motif—termed the LC3 interacting motif (LIM)—is found in nearly all of LC3's PPI partners (**Figure 4B**).

The combination of LC3's essential role in autophagosome maturation and the universal nature of the LIM in mediating its function makes the hot spot of LC3 an appealing target for specific inhibition of autophagy. Small molecules are unlikely to be effective at disrupting LC3 hot spot PPIs since it is made up of two pockets spaced over a moderate surface area rather a single pocket. Likewise, biologics would not be effective inhibitors of LC3 PPIs since the LC3 machinery operates exclusively in the cytosol. We hypothesized that SUPR peptide mRNA display might represent an ideal technology to develop compounds that possess sufficient size to mimic the LIM and disrupt LC3 PPIs while retaining cell permeability and efficient cytosolic access.

CHAPTER TWO

DIRECTED EVOLUTION OF CYCLIC PEPTIDES FOR INHIBITION OF AUTOPHAGY

Introduction

Macroautophagy (hereafter autophagy) is a conserved cellular catabolic process responsible for recycling damaged, misfolded, or superfluous cytosolic proteins and organelles (77,78,102,103). Upon initiation of autophagy, intracellular double membrane vesicles called autophagosomes are formed which engulf and sequester organelles, lipids, starches, and proteins (104). Cargo adapter proteins (e.g. p62) facilitate the transfer of organelles and protein aggregates to the interior of the autophagosome (100,105,106). Mature autophagosomes then fuse with lysosomes to degrade their contents to monomers for downstream anabolism and catabolism. Basal autophagy maintains cellular homeostasis through clearance of superfluous or damaged proteins and organelles, and autophagic flux is upregulated as an adaptive response to nutrient deprivation and exposure to cytotoxic agents. In recent years it has become increasingly apparent that autophagy upregulation plays a major role in the development and response to treatment of cancer (107–112). Many tumors types—including ovarian (79,80,113), pancreatic (85–87,114–116), breast (81,82,117), and colon cancers (84)—depend on persistent activation of autophagy to sustain growth in the poorly vascularized, hypoxic, and nutrient-deprived conditions of the tumor microenvironment (118,119). Activation of autophagy in response to chemotherapy (83,88–90,113,120,121) and radiation (91–

93,122–124) has been identified as a major contributing factor to acquisition of treatment resistance (108,112,125).

As a result of its central role in tumor development and treatment resistance, there has been intense clinical interest in autophagy inhibitors to augment frontline radiation and chemotherapy treatment strategies. As of 2019, over 50 Phase-I and Phase-II clinical trials focusing on autophagy inhibitors to treat cancer have been with the vast majority combining chloroquine (CQ) or hydroxychloroquine (HCQ) with current standard-of-care therapies (126,127). Unfortunately these non-specific lysosomotropic compounds inhibit the function of lysosomes in normal tissue leading to unwanted toxicities at therapeutically relevant doses (128). The narrow therapeutic window of chloroquine-based drugs argues for the development of targeted agents that selectively disrupt the fundamental protein-protein interactions (PPIs) of the autophagic machinery.

Microtubule-associate protein light chain 3 (LC3) is a 14 kDa ubiquitin-like protein that is essential to the maturation of the autophagosome, delivery of cargo to the autophagosome interior, and fusion with the lysosome. Following translation, pro-LC3 is cleaved by Atg4 to expose a C-terminal glycine residue (LC3-I) which is uniformly distributed throughout the cytosol. Upon induction of autophagy, LC3-I is modified by a series of autophagy-related proteins leading to conjugation of phosphatidylethanolamine (PE) to the exposed C-terminus (LC3-II). LC3-II is embedded in both inner and outer membranes of the nascent autophagosome where it facilitates its elongation and closure. Membrane-bound LC3-II also interacts with autophagy adapter proteins such as p62 (SQSTM1), NIX, NBR1, and NDP52 to

transport damaged organelles and protein aggregates to the autophagosome interior. Disruption of LC3 processing and embedding—i.e. through LC3 knockout or knockout/knockdown of *Atg5* or *Atg7* which mediate LC3 conjugation to PE—leads to dysfunctional phagophore elongation, hampered autophagosome closure, and inhibition of fusion between the autophagosome and lysosome (107,129).

Due to its essential role in the maturation of the autophagosome, blockade of LC3 PPIs represents a promising strategy for targeted autophagy inhibition. The vast majority of LC3 PPIs are thought to occur via a “hot spot” on the surface of LC3 consisting of two hydrophobic binding pockets which recognize a core amino acid motif—(W/F/Y)-XX-(L/I/V) where XX can be any amino acids (99,100,130). This sequence is referred to as the LC3-interacting motif (LIM) and is found in nearly all proteins that interact with LC3.

Inhibiting PPIs with small molecules remains challenging due to their small size and molecular radius (131,132). Small, linear peptides, which have shown great promise as PPI disruptors *in vitro*, cannot readily cross biological membranes and suffer from poor serum stability. LC3-binding peptides derived from naturally occurring LIMs possess relatively low affinities (mid to low micromolar range) and would likely suffer from the same stability and permeability issues that typically limit the usefulness of small, linear peptides *in vivo* (133).

In natural product space, there are numerous examples of cyclic peptides that readily cross the cell membrane (e.g. Microsytin LR, α -amnitin, and phalloidin (134–136)), exhibit nanomolar potencies against intracellular targets, and show sufficient

biostability for *in vivo* applications (137,138). Consequently, macrocyclic peptide scaffolds have received a great deal of attention as a means to generate PPI-disrupting compounds with drug-like affinity, stability, and cell permeability (15). One strategy for designing cell-permeable cyclic peptides focuses heavily on N-methylation of amino acids within the context of macrocyclic scaffolds. The work of Lokey and co-workers, for example, has shown that extensive methylation of backbone amides within the peptide macrocycle effectively eliminates hydrogen bonds between backbone amide protons and water and results in significant enhancement of passive cell permeability (139,140). Pei and co-workers have elegantly demonstrated that cyclic, amphipathic cell-penetrating peptides can drive the uptake of otherwise non-permeable peptide and protein cargo. These cyclic sequences can be incorporated within the context of bioactive macrocycles to greatly enhance cell uptake with minimal perturbation of biological function (141). The use of “stapled” peptides represents a third approach to enhancing cell uptake (61). In this approach, ring-closing metathesis is employed to cross-link the side chains of α -helical peptides, providing conformational constraint and stabilizing $i+4$ and $i, i+7$ hydrogen bonding patterns (61). This approach has been used to design proteolytically stable, cell permeable peptides that target MDM2/4 and inhibit proteasome-mediated degradation of p53 (142).

Scanning Unnatural Protease Resistant (SUPR) mRNA display provides a method to rapidly evolve macrocyclic, protease-resistant peptides for *in vivo* applications (143,144). SUPR peptide mRNA Display is a recent advancement of mRNA display (6,69) that integrates disuccinimidyl glutarate-based macrocyclization,

incorporation of non-proteogenic N-methyl amino acids, and pre-screening for protease resistance (76,145). This technique leads to the selection of macrocyclic peptides with high target affinity and dramatically enhanced stability to hydrolytic degradation. The SUPR peptide scaffold also recapitulates many of the physiochemical properties of cell permeable macrocyclic peptides (backbone amide N-methylation and a hydrophobic crosslinker) suggesting that SUPR peptide may possess the requisite cell permeability for disruption of intracellular PPIs.

We carried out SUPR mRNA display selections against recombinant LC3 to identify LC3-binding SUPR peptides with sufficient affinity, stability, and cell permeability for *in vivo* applications. The most promising candidate from the selection (SUPR4B1W) binds to LC3A and LC3B with mid-nanomolar affinity and was significantly more stable to proteolytic degradation than its linear and non-methylated counterparts. SUPR4B1W sensitized multiple cancer cell lines to cisplatin treatment, resulted in accumulation of intracellular p62, and significantly modulated the LC3-I/LC3-II ratio in cell culture. Finally, SUPR4B1W, in combination with carboplatin, effectively prevented intraperitoneal tumor outgrowth in orthotopic mouse models of ovarian cancer after four weeks of treatment.

Materials & Methods

Cell Lines

OVCAR5, OVCAR8, and HEY cell lines were maintained in RPMI 1640 medium supplemented with 10% fetal bovine serum, 2 mM L-Glutamine, 1 mM Na-Pyruvate, and 1% (v/v) penicillin-streptomycin. SKOV3 cells were maintained in in McCoy's 5A medium supplemented with 10% fetal bovine serum, 2 mM L-

Glutamine, and 1% (v/v) penicillin-streptomycin. MDA-MB-231, PANC-1, and MIA PaCa-2 cell lines were maintained in DMEM medium supplemented with 10% fetal bovine serum and 1% (v/v) penicillin-streptomycin.

HeLa cells were maintained in RPMI 1640 supplemented with 5% fetal bovine serum. HeLa cells stably expressing EGFP-LC3B were generated using pEGFP-LC3 (Addgene #24920). HeLa cells were directly transfected with pEGFP-LC3 using Mirus TransIT-LT1 transfection reagent and then maintained in RPMI 1640 supplemented with 5% fetal bovine serum and 400 µg/mL active G418 for 14 days. Single-cell sorting was performed on a FACSAria IIIu instrument. HeLa-GFP-LC3B cell lines derived from single cells were maintained in RPMI 1640 supplemented with 5% fetal bovine serum and 200 µg/mL active G418.

Expression and Purification of Recombinant LC3

pQTEV-MAP1LC3A vectors for expression and purification of N-terminally polyhistidine tagged recombinant LC3A were ordered through Addgene (Plasmid #34824) and transformed into BL21-DE3 pLysS E. coli (Promega). 2 Liters of LB media were inoculated from overnight cultures and grown to an OD600 of 0.6 before expression was induced with IPTG at a concentration of 0.6 mM for 3 hours. Cell pellets were resuspended in 15 mL equilibration buffer (20 mM HEPES pH 7.2, 200 mM NaCl, 10 mM imidazole) and lysed by sonication. Clarified lysate was incubated with 1 mL Ni-NTA resin for one hour, loaded onto a fritted column, and flow-through eluted. Resin was washed four times with equilibration buffer and the protein was eluted with 15 mL elution buffer (20 mM HEPES pH 7.2, 200 mM NaCl, 250 mM imidazole). Eluted protein was buffer exchanged against dialysis buffer (20 mM

HEPES pH 7.2, 200 mM NaCl, 25% glycerol) using 3,000 MWCO dialysis tubing (Fisher) and concentrated by Amicon Ultracel 3k centrifugal filters (Millipore) to a final concentration of 1.4 mg/mL (7 mg/L total yield). His6-LC3A was biotinylated using 5x molar excess biotin-NHS (Sigma). The reaction was incubated on ice for 2 hours before excess biotin-NHS was removed by 7,000 MWCO Zeba spin column (Thermo). Biotinylation was confirmed by HABA-Avidin assay (Pierce) and final concentration of biotinylated His6-LC3A was measured at 1.25 mg/mL by BCA assay.

pDEST15-LC3A and pDEST15-LC3B constructs for N-terminally tagged GST-LC3A and GST-LC3B were provided by Dr. Terje Johansen^{1,2}. Transformation and expression of plasmids were performed as described above. Clarified lysate was incubated with 1 mL glutathione agarose (Goldbio) for one hour, loaded onto a fritted column, and flow-through eluted. Resin was washed four times with equilibration buffer and the protein was eluted with 15 mL elution buffer (20 mM HEPES pH 8.0, 200 mM NaCl, 10 mM reduced glutathione). Eluted protein was exchanged against dialysis buffer (20 mM HEPES pH 7.2, 200 mM NaCl, 25% glycerol) using 3,000 MWCO dialysis tubing (Fisher) and concentrated by Amicon Ultracel 3k centrifugal filters (Millipore) to a final concentration of 1.18 mg/mL GST-LC3A and 1.13 mg/mL GST-LC3B by BCA assay.

Synthesis of N-methyl Alanine amber codon suppressor

NVOC-N-methyl-L-alanine cyanomethyl ester was synthesized according to previously described protocols for conjugation to the dinucleotide pdCpA and ligation to the amber suppressor THG73 tRNA. NVOC-Cl (269 mg, 970 μ mol, Sigma) was

dissolved in 8 mL THF and added dropwise to N-methyl-L-alanine (100 mg, 969.7 μ mol, Sigma) dissolved in 2 mL sodium carbonate. 10 N NaOH was added to bring the reaction mixture to pH > 10 and the reaction mixture was stirred at room temperature protected from light for 3 hours. Solvents were removed in vacuo and the dried compound was dissolved in 3 mL dry DMF to which 2 mL chloroacetonitrile and 600 μ L triethylamine were added. The reaction was stirred under nitrogen overnight before the solvents were removed in vacuo and the remaining solid was purified by silica gel flash chromatography.

NVOC-N-methyl-L-alanine cyanomethyl ester (12.7 mg, 33.2 μ mol) and pdCpA (5 mg, 8.3 μ mol, TriLink Biotechnologies) were dissolved in 400 μ L dry DMF under nitrogen and stirred at room temperature protected from light for 4 hours before quenching the reaction with 20 μ L ammonium acetate (25 mM, pH 4.5). The crude product was purified by reverse phase preparative HPLC using a gradient of ammonium acetate (25 mM, pH 4.5) to acetonitrile and the fractions corresponding to the product were combined and lyophilized yielding 3 mg of NVOC-N-Methyl-L-Alanine-pdCpA (36.1% yield). Product was confirmed by observing the [M+H]⁺ peak at MW = 961.54 (expected 960.21) using electrospray ionization mass spectrometry.

pUC19-THG73tRNA plasmid (a gift from Dennis Dougherty, California Institute of Technology) containing the gene for THG73 amber codon suppressor tRNA was PCR amplified and linearized by overnight FokI digestion at 37C. THG73 tRNA was transcribed in vitro by T7 RNA polymerase, purified by Urea-PAGE and dissolved in water (2 μ g/ μ L final concentration).

NVOC-N-methyl-L-alanine-pdCpA was ligated to THG73 tRNA just prior to its use in in vitro translation reactions. THG73 tRNA (20 µg in 10 µL water) and HEPES (20 µL, 10 mM, pH 7.5) were combined and heated at 95 °C for 3 minutes, then cooled to 37 °C. NVOC-N-Methyl-L-Alanine-pdCpA (8 µL, 3 mM in DMSO) was added to the tRNA-HEPES mixture along with water (30 µL), T4 RNA Ligase (4 µL, New England Biolabs), and 10x T4 Reaction Buffer (8 µL, New England Biolabs). The reaction was incubated at 37 °C for 65 minutes, extracted with 25:24:1 phenol:chloroform:isoamyl alcohol (Sigma), and precipitated with >3 volumes cold ethanol at -80 °C. The precipitate was dried by vacuum, dissolved in 20 µL 1 mM sodium acetate, quantified by measuring A260, and adjusted to a final concentration of 1 µg/µL. Immediately prior to in vitro translation the AA-tRNA solution was deprotected by short-wave UV for 15 minutes.

SUPR mRNA Display Library Preparation

To perform selections, we assembled a DNA library encoding eight random positions between an N-terminal methionine residue and a C-terminal lysine residue. The library was constructed by the PCR amplification of the antisense template oligo (5' TCC GCT GCC GGA TTT SNN SNN SNN SNN SNN SNN SNN SNN CAT TGT AAT TGT AAA TAT AAT T 3' where N= A, C, G or T and S = C or G) with the primers MKForward (5' TAA TAC GAC TCA CTA TAG GGA CAA TTA CTA TTT ACA ATT ACA 3') and MKReverse (5' GCC AGA TCC GCT GCC GGA TTT 3'). In addition to the open reading frame, the DNA library contains a T7 promoter sequence and a ribosome binding site.

The mRNA display library was generated by *in vitro* transcription of the DNA library. Transcription was performed by incubating DNA libraries with transcription buffer (80 mM HEPES-KOH, pH 7.5, 2 mM spermidine, 40 mM DTT, and 25 mM MgCl₂) and rNTP mixture (4 mM ATP, GTP, CTP, UTP) at 65 °C for 15 minutes before cooling briefly at room temp and adding T7 RNA polymerase. Transcription reactions were allowed to proceed overnight at 37 °C and were terminated by phenol chloroform extraction and ethanol precipitation. The mRNA library was then purified by running denaturing Urea-PAGE, cutting out mRNA bands, and recovering by electroelution.

The mRNA library was then ligated at the 3' end to a puromycin-DNA linker (pF30P - 5' 8AA AAA AAA AAA AAA AAA AAA A77 7AC C6 3') where 6 = puromycin CPG, 7 = spacer phosphoramidite 9, 8 = phosphate). Puromycin acts as an aminoacyl tRNA mimetic that can enter the active site of the ribosome to form a covalent link between the translated peptide and its encoding mRNA resulting in an mRNA-peptide fusion. Ligation reactions were performed by incubating 3000 pmol of mRNA library with 1.2 molar excess PF30P, 1.4 molar excess splint oligo (5' TTT TTT TTT TGC CAG ATC CGC TG 3'), and T4 DNA ligase at room temperature for 75 minutes. The ligated mRNA library was then purified by Urea-PAGE and electroelution as described above.

mRNA Display Selection

In vitro translations were performed using rabbit reticulocyte lysate kits (Ambion). To assemble the translation reaction 10 pmol ligated mRNA library was added to rabbit reticulocyte lysate (17 µL), EasyTag [35S]-Methionine (3 µL, 8

$\mu\text{Ci}/\mu\text{L}$, PerkinElmer), amber suppressor tRNA charged with N-Methyl Alanine (2.25 μL , 1 $\mu\text{g}/\mu\text{L}$), 20x high salt mix (1.25 μL , KOAc 3 M, MgOAc 10 mM, creatine phosphate 200 mM, and 1 mM of each amino acid except methionine). After a 70 minute incubation at 30 °C the translation mix was supplemented with 100 mM KCl and 0.5 mM MgCl₂ to promote the formation of mRNA-peptide fusions. mRNA-peptide fusions were purified from the translation mix using oligo-dTcellulose (GE) which selectively binds to the poly dA linker between the mRNA template and puromycin. Oligo dT cellulose was washed with dT binding buffer (Tris-HCL pH 8.0 20 mM, NaCl 1 M, EDTA 1 mM, Triton-X 0.2% (v/v)) and translation mixes were rotated with 10 mg of oligo dT cellulose in 500 μL dT binding buffer at 4 °C for 60 minutes. The oligo-dT cellulose was then washed with dT wash buffer (Tris-HCL pH 8.0 20 mM, 300 mM NaCl) and mRNA-peptide fusions were eluted in 60 °C water.

Following dT purification, mRNA-peptide fusions were ethanol precipitated and resuspended in 50 mM phosphate buffer pH 8.0 for cyclization between the primary amine of the lysine side chain and at the N-terminal amine using the crosslinker disuccinimidyl glutarate (DSG). The cyclization reaction was carried out by adding DSG to the mRNA-peptide fusions to a final concentration of 200 $\mu\text{g}/\text{mL}$ and rotating at room temperature for 60 minutes. Cyclized mRNA-peptide fusions were then dT purified using the method described above. Following purification, mRNA-peptide fusions were reverse transcribed by M-MuLV reverse transcriptase (NEB). Reverse transcribed fusions were subjected to protease screening by incubating with proteinase-K agarose (Sigma) for 30 s before filtering with Spin-X microcentrifuge column. To eliminate sequences with significant off-target binding to

the resin, proteinase-treated fusions were incubated with streptavidin-agarose (Life Technologies) at 4 °C for 60 minutes before recovering unbound fusions using Spin-X microcentrifuge column.

Selection targets were prepared by incubating streptavidin-agarose with 1.5x molar excess biotinylated-LC3A at 4 °C with rotation for 30 minutes to saturate the resin with target. The immobilized target was then washed thoroughly with selection buffer (20 mM HEPES-KOH pH 7.5, 150 mM NaCl, 0.2% (v/v) Tween-20, 1 mg/mL BSA, 50 µg/mL tRNA, 1 mM β-mercaptoethanol). Selections were carried out by incubating fusions with immobilized target with rotation for 2 hours. Selection incubations were carried out at 4 °C for the first four rounds of selection and then split into parallel selections carried out at 25 °C or 4 °C thereafter. Following incubation, the selection resin was washed 3 times with selection buffer and filtered with a Spin-X column. The resin was then washed two additional times in selection buffer without BSA or tRNA and bound fusions were eluted in 0.15% sodium dodecyl sulfate (SDS) (Thermo-Fisher). SDS was subsequently precipitated using SDS-Out (Thermo-Fisher) and eluted fusions were filtered and ethanol precipitated. The precipitated pellet was resuspended in dH₂O and one fifth of the total volume was subjected to PCR amplification using the MKFor and MKRev primers. Small volumes of PCR product were removed every 3 PCR cycles and tested by 4% agarose gel to identify formation of the amplified product. The remaining eluted fusions were amplified using the minimum PCR cycles as defined in the previous step. Further selection rounds were conducted using previous round's enriched dsDNA library.

The library was considered converged when the number of PCR cycles required to recover the enriched dsDNA library did not decrease in three consecutive rounds.

Sanger Sequencing

After libraries converged, the final pool was TOPO-TA cloned into pCRTMII-TOPO[®] vector (Thermo-Fisher), transformed into One Shot TOP10 chemically competent *E. coli* (Thermo-Fisher), and plated on ampicillin-agarose to isolate individual sequences from the final selection pool. Twelve colonies from each parallel selection were selected at random and plasmid minipreps (Life Technologies) were prepared from 5 mL overnight cultures. Amplified plasmids were submitted for Sanger sequencing and analyzed using FinchTV software. Peptide Synthesis and Cyclization

Peptide Synthesis and Cyclization

Peptides were synthesized using a Prelude automated peptide synthesis instrument (Protein Technology, Inc.). 2-chlorotrityl resin (0.439 g, 0.5 mmol, Advanced Chemtech) was swollen in DMF for 1 hour and washed twice with 5 mL DMF. The initial C-terminal amino acid coupling to the resin was performed manually prior to automated synthesis of peptides. 2 equivalents Fmoc-propargylglycine (1 mmol, 335 mg) and 3 equivalents N,N-diisopropylethylamine (DIEA, 1.5 mmol, 262 μ L, Sigma) were added to the swelled resin in 6 mL DMF and rotated at room temperature for 1 hour. To synthesize each peptide, 100 mg of Fmoc-propargylglycine resin was loaded onto the automated synthesis instrument and synthesis was performed with 3 equivalents of Fmoc amino acid (Oakwood Products, Inc.), DIEA, and N,N,N',N'-Tetramethyl-O-(1H-benzotriazol-1-yl)uronium

hexafluorophosphate (HBTU, Oakwood Products, Inc.) in N-methyl Pyrrolidone (NMP). A total of 3 coupling reactions (10 minute duration) were performed for each amino acid building block. Deprotection of Fmoc groups was achieved using 20% (v/v) piperidine in NMP. After synthesis and final deprotection, resin was washed 5x with NMP (1.5 mL, 2.5 minutes), 5x with DCM (1.5 mL, 2.5 minutes), and dried under vacuum for 1 hour. Peptides were cleaved from the resin with 95% (v/v) trifluoroacetic acid, 2.5% (v/v) water, 2.5% (v/v) triisopropylsilane at room temperature for 3 hours, precipitated with cold diethyl ether, and dried under vacuum. Crude products were purified by reverse phase preparative HPLC (Luna Phenomenex, 5 μ m C18(2), 250 mm x 21.2 mm LC column) using gradient elution (5-95% Buffer B over 45 minutes; Buffer A dH₂O + 0.1% (v/v) TFA, Buffer B CH₃CN + 0.1% (v/v) TFA). Appropriate fractions were combined and lyophilized yielding a white solid. Purified products were confirmed by electrospray ionization mass spectrometry.

Amine reactive cross-linker chemistry was utilized to cyclize peptides between the N-terminus of the peptide and the side-chain of a C-terminal lysine residue. Purified linear peptide was dissolved in DMF and mixed with 1.1 equivalents of disuccinimidyl glutarate (DSG) and 7 equivalents DIEA at room temperature for 3 hours. After 3 hours the reaction was quenched with hydroxylamine (10 mM final concentration) for 15 minutes and solvent was removed in vacuo. The crude product was dissolved in 1 mL 95:5 (v/v) dH₂O:CH₃CN + 0.1% (v/v) TFA and purified by reverse phase preparative HPLC using gradient elution (5-20% Buffer B over 5 minutes, 20-95% Buffer B over 60 minutes; Buffer A dH₂O + 0.1% (v/v) TFA, Buffer

B CH₃CN + 0.1% (v/v) TFA). Appropriate fractions were combined and lyophilized yielding a white solid. Purified products were confirmed by electrospray ionization mass spectrometry.

Fluorophore Conjugation of SUPR Peptides

Copper-catalyzed click chemistry was used to conjugate fluorescein-azide to the side-chain alkyne of the C-terminal propargylglycine residue in SUPR peptides. Between 2-3 μ mol of each peptide was dissolved in DMSO and added to 1.2 equivalents FAM-azide, 6-isomer (50 mg/mL, Lumiprobe), 50 μ L click solution (16 mg/mL CuSO₄·2H₂O and 30 mg/mL L-ascorbic acid in dH₂O), 5 μ L of tris-(benzyltriazolylmethyl)amine (TBTA, 100 mg/mL in DMF). Reaction mixture was brought to a final volume of 150 μ L with dH₂O and rotated at room temperature for 2 hours and purified by reverse phase preparative HPLC (Luna Phenomenex, 5 μ m C18(2), 250 mm x 21.2 mm LC column) using gradient elution (5-95% Buffer B over 45 minutes; Buffer A dH₂O + 0.1% (v/v) TFA, Buffer B CH₃CN + 0.1% (v/v) TFA). Appropriate fractions were combined and lyophilized yielding a yellow-green solid. Purified products were confirmed by electrospray ionization mass spectrometry.

Copper-catalyzed click chemistry was used to conjugate carboxy-X-rhodamine (ROX) azide to the side-chain alkyne of the C-terminal propargylglycine residue of SUPR4B1W. 3 μ mol of SUPR4B1W was dissolved in DMSO and added to 1.2 eq ROX-azide (50 mg/mL, Lumiprobe), 50 μ L click solution (16 mg/mL CuSO₄·2H₂O and 30 mg/mL L-ascorbic acid in dH₂O), 5 μ L of TBTA (100 mg/mL). Reaction mixture was brought to a final volume of 150 μ L with dH₂O and rotated at room temperature for 2 hours and purified by reverse phase preparative HPLC

(Luna Phenomenex, 5 μ m C18(2), 250 mm x 21.2 mm LC column) using gradient elution (5-95% Buffer B over 45 minutes; Buffer A dH₂O + 0.1% (v/v) TFA, Buffer B CH₃CN + 0.1% (v/v) TFA). Appropriate fractions were combined and lyophilized yielding a light purple solid. Purified products were confirmed by electrospray ionization mass spectrometry

Biotin Conjugation of SUPR peptides

Copper-catalyzed click chemistry was used to conjugate biotin-azide to the side-chain alkyne of the C-terminal propargylglycine residue in SUPR peptides. 2 μ mol of SUPR4B1W was dissolved in DMSO and added to 1.2 equivalents Biotin-PEG3-azide (Thermo-Fisher), 50 μ L click solution (16 mg/mL CuSO₄·2H₂O and 30 mg/mL L-ascorbic acid in dH₂O), 5 μ L of tris-(benzyltriazolylmethyl)amine (TBTA, 100 mg/mL). Reaction mixture was brought to a final volume of 150 μ L with dH₂O and rotated at room temperature for 2 hours and purified by reverse phase preparative HPLC (Luna Phenomenex, 5 μ m C18(2), 250 mm x 21.2 mm LC column) using gradient elution (5-95% Buffer B over 45 minutes; Buffer A dH₂O + 0.1% (v/v) TFA, Buffer B CH₃CN + 0.1% (v/v) TFA). Appropriate fractions were combined and lyophilized yielding a white solid. Purified products were confirmed by electrospray ionization mass spectrometry.

Radiolabeled Binding Assays

Plasmid minipreps for individual clones were PCR amplified using the MKFor and MKRev primers to obtain dsDNA for individual sequences from the final pool. These dsDNA sequences were transcribed, ligated, and translated in the presence of [³⁵S]-Methionine as described above. Following incubation for 70 minutes, RNase

A (1 μ L, 10 mg/mL, MilliporeSigma) was added to the translation mix to digest the mRNA fused to the peptides which might impact binding. The peptides were purified from translation using dT cellulose and subjected to cyclization as described above. A small portion of the cyclized and purified translation product was reserved for scintillation counting and the remaining product was incubated with biotinylated-LC3A immobilized on neutravidin-acrylamide (Thermo-Fisher) at 25 °C with rotation for 1 hour. The incubation mix was pelleted, the supernatant reserved, and the pelleted resin washed three times with Spin-X microcentrifuge columns. The resin pellet and portions of the supernatant and each wash were subjected to scintillation counting and a percentage of input activity that remained bound to the immobilized target after washing was calculated for each clone.

Fluorescence Polarization Assays

For fluorescence polarization assays, stock solutions of GST, GST-LC3A and GST-LC3B were adjusted to 5 μ M and serially diluted to concentrations between 5 μ M and 2.4 nM in triplicate in black polystyrene 96-well plates (Corning). FAM-labeled peptide was added to each well to a final concentration of 10 nM and incubated at room temperature for 2 hours. Fluorescence polarization was measured on a Biotek Synergy Neo Microplate Reader using a dual PMT FP 485/528 filter set. The mean value of polarization was calculated for each sample concentration and mean polarization values for GST were subtracted from GST-LC3 measurements to eliminate any effects from non-specific interactions. Mean fluorescence polarization measurements were converted to fluorescence anisotropy and fit to a one-site

saturation binding model in Graphpad Prism 8 to calculate equilibrium binding constants for each peptide.

Atg4B Activity Assay

LC3-AMC (R&D Systems) was diluted in Reaction Buffer (25 mM Tris, 150 mM NaCl, 10 mM DTT) to a final concentration of 230 nM. 20 μ L of LC3-AMC was added to 5 μ L SUPR peptide (1 μ M, 500 μ M, 250 μ M, 0 μ M in Reaction Buffer) in a 96-well microtiter plate pre-blocked with 5 mg/mL BSA. After incubating for 5 minutes at room temperature, 25 μ L 400 pM Atg4B (R&D Systems) was added to initiate the reaction. The final concentrations of each component in the hydrolysis reaction were LC3-AMC (92 nM), Atg4B (200 pM), and SUPR peptide (0-100 μ M), and the final volume was 50 μ L. The hydrolysis reaction was allowed to progress at room temperature for 40 minutes and the fluorescence measured each minute (λ EX = 380 nm, λ EM = 460 nm) on a BioTek Synergy H4 microplate reader. The resulting fluorescence at each time point (AU) was normalized to the fluorescence at t=0 to compute the normalized product. Each reaction condition was carried out in triplicate and the values shown represent the mean value of three measurements.

Proteinase-K Stability Assays

Protease stability was assessed by treating peptide solutions (1 mM in PBS, final volume 500 μ l) with 0.3 mg proteinase-K agarose (Sigma). At time intervals of 0, 30, 60, 120, and 240 minutes, 50 μ L samples were taken from the digestion mixture and separated from proteinase-K agarose by centrifugal filtration with Spin-X columns. Samples were then subjected to analytical HPLC (Agilent 1100 Series HPLC equipped with a Phenomenex Gemini 5 μ C18 110A column) using

gradient elution (10-30% Buffer B over 30 minutes; Buffer A dH₂O + 0.1% (v/v) TFA, Buffer B CH₃CN + 0.1% (v/v) TFA). Peak area was calculated for the peak corresponding to the intact peptide for each sample and the fraction intact was calculated for each time point. Half-lives for each peptide were calculated in Graphpad Prism 8.

ATG8 homologue Selectivity

SUPR-4B1W-biotin was conjugated to neutravidin acrylamide by adding 2 µL, 1 mM SUPR-4B1W-biotin to 50 µL neutravidin acrylamide slurry (Thermo-Fisher) with 200 µL binding buffer (150 mM NaCl, 50 mM Tris-HCl, pH 7.8) and rotating for 1 hr at room temperature. The immobilized peptide resin was then washed twice with 200 µL binding buffer using Spin-X centrifugal filter columns.

pET151/D-TOPO bacterial expression vectors containing the genes for LC3A, LC3B, LC3C GABARAPL1, GABARAPL2, ATG8, and ubiquitin were designed and ordered from Thermo-Fisher. Forward and Reverse primers were designed to allow PCR amplification of each gene from the bacterial vectors with the addition of 5' T7 promotor and ribosome binding site sequences. Following PCR amplification, DNA templates were extracted with 25:24:1 Phenol:chloroform:isoamyl alcohol (Sigma) and precipitated with >3 volumes cold ethanol at -80 °C. The centrifuged precipitate was dried by vacuum and resuspended in 100 µL dH₂O. DNA templates were transcribed *in vitro* by T7 RNA polymerase and purified by UreaPAGE. 10 pmol of each RNA template were translated *in vitro* in the presence of [³⁵S]-Methionine as described previously.

To test selectivity of SUPR4B1W for the various ATG8 homologues, 8 μL of translation reaction was added to 10 μL of either peptide-saturated resin (125 pmol/ μL resin) or naked resin in triplicate and brought to a final volume of 50 μL with binding buffer (20 mM HEPES-KOH pH 7.5, 150 mM NaCl). Reaction mixtures were rotated at room temperature for 60 minutes before reaction mix was transferred to a Spin-X column, washed 3x with 200 μL binding buffer, and washed resin was subjected to scintillation counting.

Fluorescence microscopy

HeLa cells stably expressing eGFP-LC3 were seeded at a density of 30,000 cells/well in an 8-well chambered coverslide (Corning) 24 hours before beginning treatment. Cells were treated with complete media supplemented with 500 nM SUPR4B1W-ROX for 12 hours. After 12 hours cells were either starved with Hank's Balanced Salt Solution (Corning) or were given fresh complete media for 2 hours and then subjected to live-cell fluorescence confocal imaging.

Quantification of colocalization between SUPR4B1W-ROX and eGFP-LC3 puncta was performed in ImageJ. Three fields of images for both starved and unstarved treatments were selected and split into red and green channels. Cells that were mitotic or had lost eGFP-LC3 expression were removed from the analysis. Manders M1 and M2 coefficients were calculated using the Just Another Colocalization (JACoP) plugin using appropriate pixel intensity thresholding to filter background signal.

Cellular Cisplatin Sensitization Assays

OVCAR8, OVCAR5, HEY, SKOv3, MDA-MB-231, PANC-1, and MIA PaCa-2 cells were seeded in black-walled 96-well plates at a density of 5,000 cells/well 24 hours prior to treatment. Cells were treated with SUPR peptides (50 μ M) or chloroquine (5 μ M, Sigma) both in the presence and absence of cisplatin (10 μ M, Sigma) in order to determine the effect of autophagy inhibition on cellular viability in treatment resistant cell lines. Cells were treated for a total of 48 hours (n = 6 per treatment group) prior to viability testing by 3-(4,5-dimethylthiazol-2-yl)-2,5-diphenyltetrazolium bromide (MTT) assay. Differences in cellular viability measurements between treatment groups were evaluated in R by applying two-way ANOVA after applying a log₁₀ or square root transformation to satisfy normality.

Cisplatin Sensitization Animal Model

Athymic nude mice were injected with 2 million OVCAR8 cells IP. Mice were treated with SUPR4B1W (10 mg/kg) combined with carboplatin (25 mg/kg) or saline 3x per week by IP injection. Each treatment group had 8 mice, with the exception of the group treated with carboplatin alone which had 4 mice. Treatments were administered for 3 weeks before mice were sacrificed and tumors were dissected and weighed. Differences in tumor mass between treatment groups were evaluated in R by a nonparametric Mann-Whitney-Wilcoxon rank-sum test.

The assay was repeated with the additional treatment groups for combinations of scrambled SUPR4B1W (10 mg/kg) with carboplatin (25 mg/kg) or saline. Treatment group size was expanded to 10 mice and the duration of the experiment was extended from 3 weeks to 4 weeks.

Statistical Analysis

To determine the independent and interactive effects of cisplatin and SUPR4B1W on cell viability, we used a two-way ANOVA with Type I sum of squares on A_{600} absorbance. Log10 and square root transformations were used on OVCAR8 and HEY cell line absorbance data, respectively, to achieve satisfactory normality. To determine the independent and interactive effects of carboplatin and SUPR4B1W structure on tumor weight in mice, we used a two-way ANOVA with Type III sum of squares. A square root transformation was necessary to handle right skewedness in Week 4 data. Following both analyses, Tukey's HSD via the package *lsmeans* was used to determine which treatment means were significantly different from one another.

Results & Discussion

Our goal was to generate small, protease-stable peptides with high affinity and selectivity for LC3. In order to generate target for selection, His6-tagged LC3A was expressed in *E. coli* and purified by Ni-NTA affinity chromatography (8.1 mg/L culture). Biotinylation of recombinant LC3A was carried out using Biotin-NHS and confirmed by HABA-Avidin assay. LC3A-biotin was then immobilized on streptavidin agarose for selection.

Selection against LC3A using MK8 Library

Selections against LC3A were carried out using SUPR peptide mRNA display(144). The DNA template library was designed with eight random codons and a fixed lysine codon to allow cyclization between the side chain of lysine and the N-terminal amino group (**Figure 1A**). The resulting library was translated in the

presence of amber suppressor tRNA acylated with N-methyl-L-alanine.

After seven rounds of selection against LC3A, binding of the library to the immobilized target increased

dramatically as evidenced by a reduction in the number of PCR cycles required to amplify the enriched library

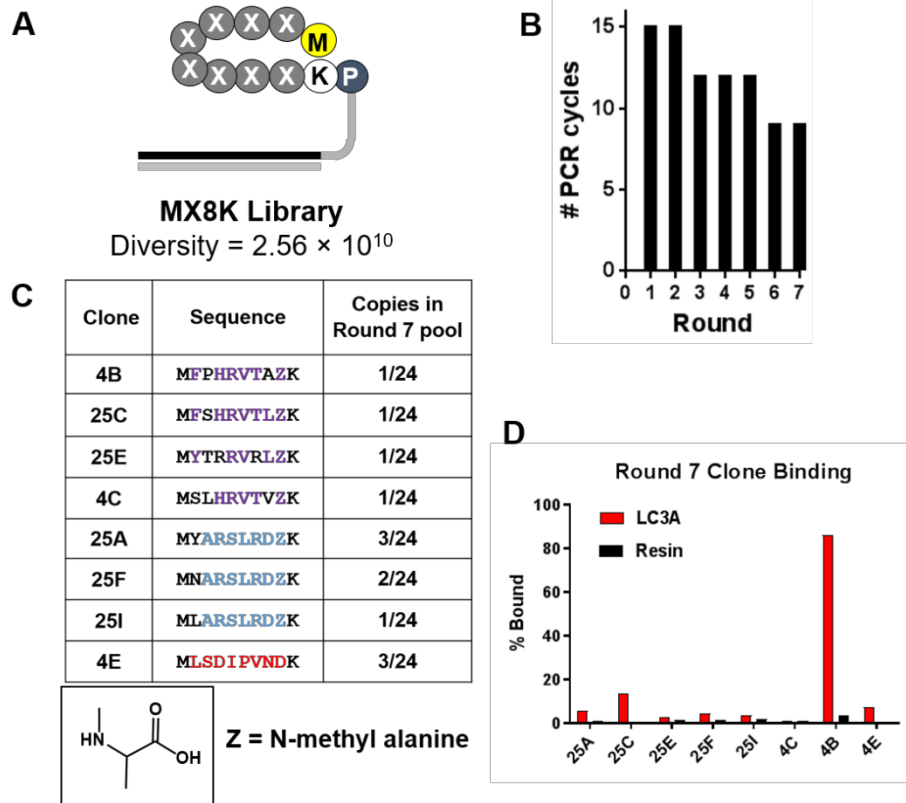


Figure 1 Selection of LC3-binding SUPR peptides. **A)** Schematic of the MX₈K library. Eight randomized codons were installed between the N-terminal methionine and a locked lysine residue. The library was cyclized by disuccinimidyl glutarate (DSG)-mediated crosslinking of the N-terminal amino group and the side-chain amino group of lysine. **B)** After seven rounds of selection the number of PCR cycles required to amplify the enriched dsDNA library declined and plateaued indicating convergence of the library. **C)** Sequencing of the final pool revealed three dominant peptide families (purple, blue and red). >80% of sequences identified had incorporated an N-methyl-L-alanine residue (Z) in the final random position of the macrocycle. **D)** Each sequence was synthesized as an mRNA-peptide fusion and panned against LC3A immobilized on streptavidin acrylamide or streptavidin acrylamide alone (resin). Clone 4B showed 86% binding to immobilized LC3 and minimal binding to the resin.

(Figure 1B). Sequencing revealed three dominant sequence families in the final pool which each share a consensus motif (Y/F/N/L)-XXX-(L/V/I) analogous to canonical LIM albeit with an additional amino acid in the spacer region (Figure 1C). It is possible that this additional amino acid arose from the more constrained conformation of the cyclic peptide compared to the linear LIMs found in LC3 adaptor proteins which typically occur as elongated β -strands(101).

Sequencing data also revealed that >80% of the clones analyzed from the round 7 pool incorporated N-methyl-L-alanine at position 9 within the macrocycle indicating that the selection provides a significant selection pressure for N-methyl-L-alanine incorporation at this position. In order to identify the highest affinity clones from the round 7 pool, we performed radioligand binding assays. Individual clones were translated as mRNA-peptide fusions in the presence of [³⁵S]-methionine, cyclized, and treated with RNase A to remove the RNA portion yielding peptides conjugated only to the poly-dA linker. Radiolabeled peptide-DNA conjugates were then panned against LC3A immobilized on neutravidin-acrylamide or resin alone. After an hour incubation at room temperature the resins were washed thoroughly and analyzed by scintillation counting. While several clones showed a moderate level of target-specific binding, clone 4B (cycl MFPHRVTAZK), hereafter SUPR4B, showed the highest target-specific binding with 86% of the input activity remaining bound to the immobilized target and minimal nonspecific binding to the resin alone **(Figure 1D)**.

Binding affinities of SUPR-4B and variants towards LC3A and LC3B

While SUPR4B appears to serve as a non-canonical LIM, we noted that phenylalanine occurred at the first randomized position within the macrocycle. Based on known LIM sequences, this residue is likely to interact with the W-site of the LC3 hot spot. Although some LIMs have phenylalanine in this position, it is the least commonly occurring amino acid residue (101). Binding to the W-site is achieved by burying an aromatic residue into the hydrophobic pocket, and the sidechain of tryptophan is well-suited to perform this interaction. While phenylalanine

and tyrosine appeared in the first position of the macrocycle in several clones, tryptophan was not incorporated in any of the peptides sequenced. This may have arisen from the low frequency of tryptophan-encoding codons in the library

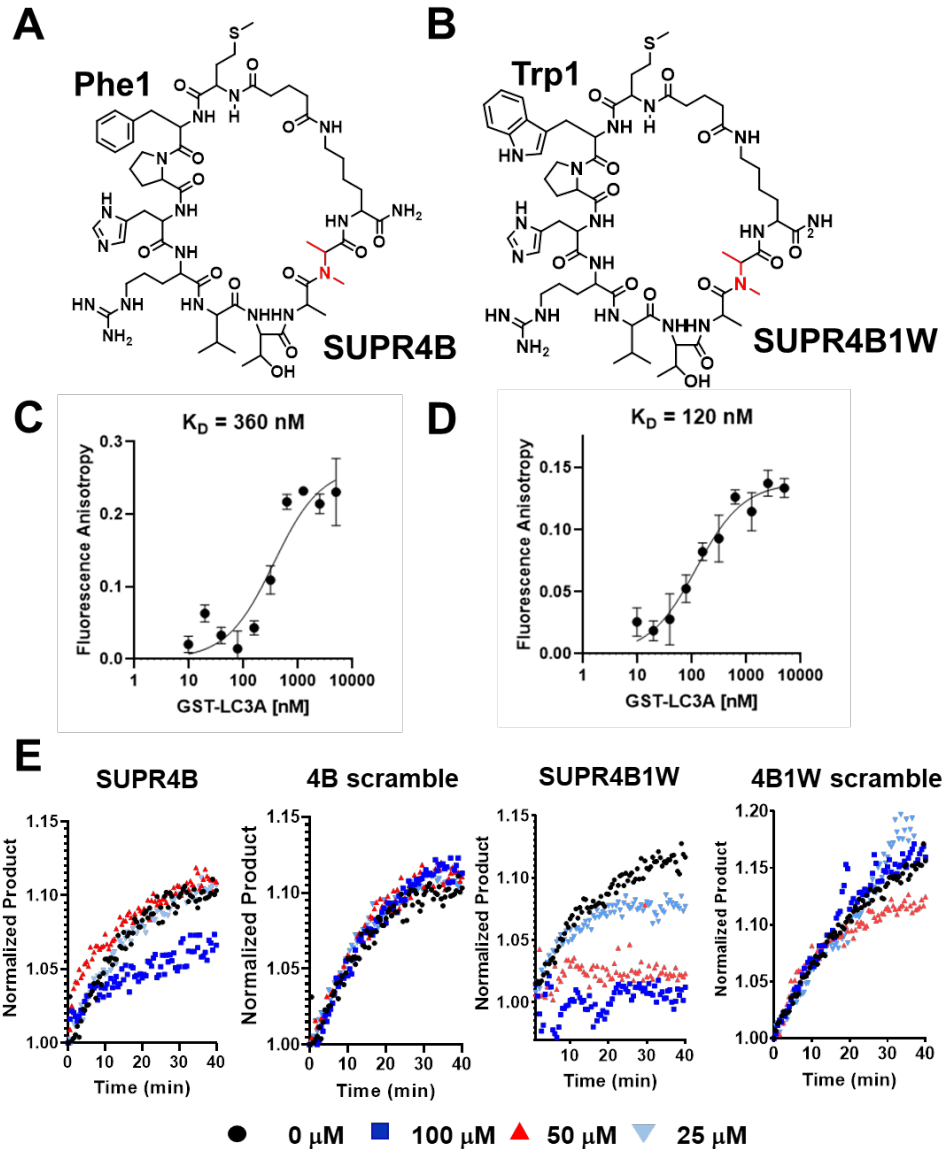


Figure 2: Binding affinities of SUPR4B peptides. **A)** Structure of SUPR4B. **B)** Structure of SUPR4B1W. FAM labeled SUPR peptides were incubated with increasing concentrations of GST-LC3A and fluorescence polarization measurements were made in triplicate. Each measurement was converted to anisotropy and fit to a one-site saturation binding model in Graphpad Prism to obtain the equilibrium binding constant. **C)** SUPR4B binds LC3A with a $K_D = 360$ nM **D)** SUPR4B1W binds LC3A with a $K_D = 120$ nM. **E)** Atg4B enzyme inhibition assay. Increasing concentrations of both SUPR4B and SUPR4B1W impair the ability of Atg4B to cleave the C-terminus of LC3-AMC leading to diminished AMC fluorescence. Neither scrambled peptide inhibited Atg4B's ability to cleave LC3-AMC.

(1/32) or poor incorporation efficiency at the N-terminus. Our sequencing may also have been too sparse to detect clones with tryptophan at the 2nd position and next-

generation high throughput sequencing may reveal such clones. we hypothesized that substitution of tryptophan for phenylalanine at position 2 in SUPR4B (SUPR4B1W) would improve affinity for LC3.

To evaluate the impact of tryptophan substitution on binding affinity for LC3, we measured the binding affinity of both SUPR4B (**Figure 2A**) and SUPR4B1W (**Figure 2B**) using fluorescence polarization anisotropy. Fluorescein-labeled SUPR peptides were incubated with increasing concentrations of GST-LC3A and GST-LC3B. Fluorescence polarization was measured ($\lambda_{Ex} = 485 \text{ nm}$, $\lambda_{Em} = 528 \text{ nm}$) and converted to fluorescence polarization anisotropy which was plotted against concentration of protein and fit to a one-site saturation binding model. SUPR-4B1W was found to bind to GST-LC3A with a K_D of $120 \pm 19 \text{ nM}$ while SUPR-4B bound to GST-LC3A with a K_D of $360 \pm 83 \text{ nM}$ (**Figure 2C, D**). This data supported our prediction that the larger aromatic side-chain of tryptophan would engage more strongly with the hydrophobic W-site binding pocket and increase the affinity of SUPR4B1W for LC3A relative to SUPR4B. SUPR-4B1W was also found to bind to GST-LC3B with a K_D of 189 ± 40.1 while SUPR-4B bound to GST-LC3B with a K_D of $392 \pm 82.7 \text{ nM}$ (**Table 1**). This indicates that selection against LC3A resulted in ligands with similar affinities for the LC3B homolog which is unsurprising given the 83% residue identity and 90% residue similarity between the two proteins (Clustal Omega alignment)

Binding affinity of both SUPR4B and SUPR4B1W for LC3A is significantly enhanced by cyclization. Fluorescence polarization assays were carried out using fluorescein-labeled linear SUPR4B and SUPR4B1W. Linear SUPR4B1W was found

to bind to GST-LC3A with a $K_D > 375$ nM while linear SUPR4B bound to GST-LC3A with a $K_D > 690$ nM. Linear SUPR4B1W was found to bind to GST-LC3B with a $K_D > 415$ nM while linear SUPR4B bound to GST-LC3B with a $K_D > 335$ nM (**Table 1**). These data indicate that cyclization provides at least 0.68 kcal/mol of binding energy for SUPR4B1W when interacting with LC3A likely through reduction of conformational entropy.

We also synthesized a version of SUPR4B1W in which the N-methyl-L-alanine at position 9 was replaced with L-alanine (SUPR4B1W8A) to determine the effect of N-methylation on binding affinity. Fluorescein-labeled SUPR-4B1W8A bound to GST-LC3A with a K_D of 105 ± 23.2 nM and GST-LC3B with a K_D of 197 ± 52.1 nM. These affinities are very similar to those observed for SUPR4B1W and indicate that incorporation of N-methylated amino acids does not positively contribute to binding energy in the case of SUPR4B1W. A summary of binding affinities obtained by fluorescence anisotropy is presented in **Table 1**.

	LC3A K_D (nM)	LC3B K_D (nM)
SUPR4B1W Linear	> 375	> 415
SUPR4B1W Cyclic	120 ± 19	189 ± 40.1
SUPR4B Linear	> 690	> 335
SUPR4B Cyclic	360 ± 83	392 ± 82.7
SUPR4B1W 8A Linear	> 1125	> 1250
SUPR4B1W8A Cyclic	105 ± 23.2	197 ± 52.1

Table 1 Binding affinities of SUPR peptides for LC3A/B by fluorescence polarization anisotropy

SUPR Peptides Attenuate Atg4b-mediated cleavage of LC3

Atg4 is a cysteine protease that plays a critical role in the regulation of autophagy through post-translational modification of LC3 homologs. Following translation, Atg4 binds to LC3 via a LIM and cleaves the protein at the C-terminus to expose a glycine residue which is lipidated with phosphatidylethanolamine (PE) prior to membrane insertion. We hypothesized that if our SUPR peptides bound to the Atg4 LIM-recognizing site on LC3, Atg4 binding and proteolytic cleavage would be inhibited. LC3A bearing a C-terminal 7-amino-3-methylcoumarin moiety (LC3-AMC) was pre-incubated with increasing concentrations of SUPR-4B, SUPR-4B1W, or a scrambled version of either SUPR peptide. Since AMC is only fluorescent when free in solution ($\lambda_{Ex} = 380 \text{ nm}$, $\lambda_{Em} = 460 \text{ nm}$), cleavage of LC3 by Atg4 can be monitored by increase in fluorescence at 460 nm. Atg4B (220 pM) was added to each combination of LC3-AMC (120 nM) and SUPR peptide (0-100 μM) and fluorescence emission was monitored for 40 minutes (**Figure 2E**). SUPR-4B inhibits Atg4B cleavage of LC3-AMC with an apparent $K_i > 100 \mu\text{M}$ while SUPR-4B1W inhibits cleavage with apparent $K_i \sim 35 \mu\text{M}$. Neither scrambled peptide had any inhibitory effect on Atg4B cleavage of LC3-AMC indicating that inhibition is sequence-dependent. These results suggest that the SUPR peptides occupy the PPI hot spot of LC3 and prevent formation of the Atg4:LC3 complex leading to inhibition of C-terminal proteolysis.

Protease stability is dependent on cyclization and N-methyl incorporation

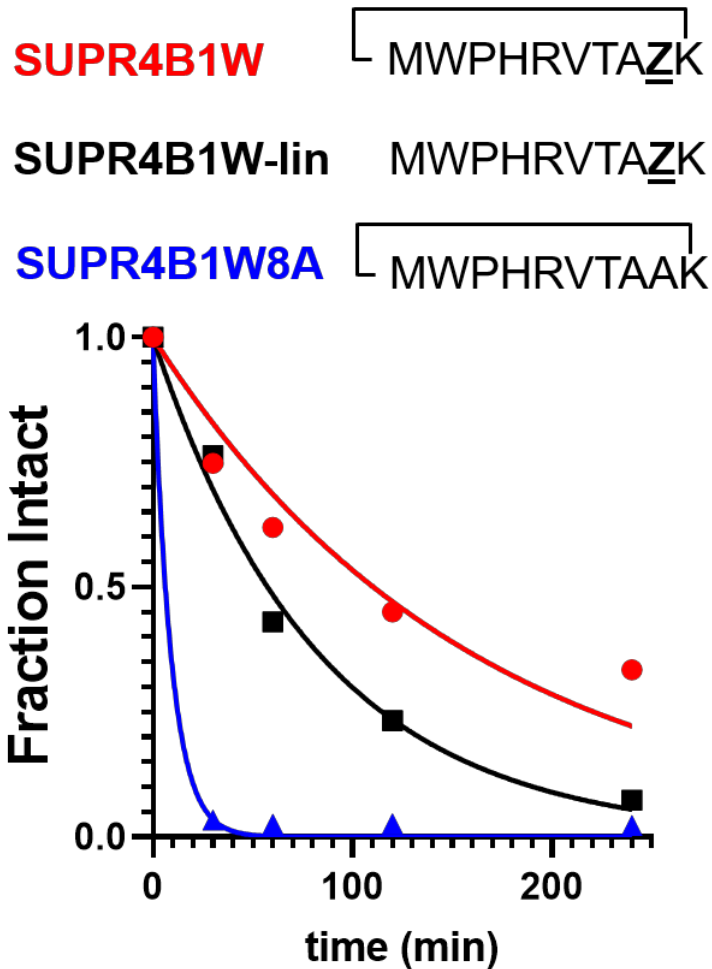


Figure 3. Cyclization and N-methyl-L-alanine dramatically improve the protease stability of SUPR4B1W. Analytical HPLC experiments show that SUPR4B1W has a half-life in proteinase-K of ~110 min (red line). Without cyclization, linear SUPR4B1W has a half-life of 57 min, a nearly 2-fold reduction (black line). N-L-methyl alanine plays a crucial role in mediating protease resistance; substitution of L-alanine reduces the protease half-life of the SUPR peptide to 6 min (blue line).

Peptides are highly susceptible to proteolysis in human serum and this feature has compromised the translation of many peptides into therapeutic compounds. SUPR mRNA display attempts to mitigate this drawback through macrocyclization and incorporation of N-methyl amino acids which have been shown to increase biological half-lives of peptides by

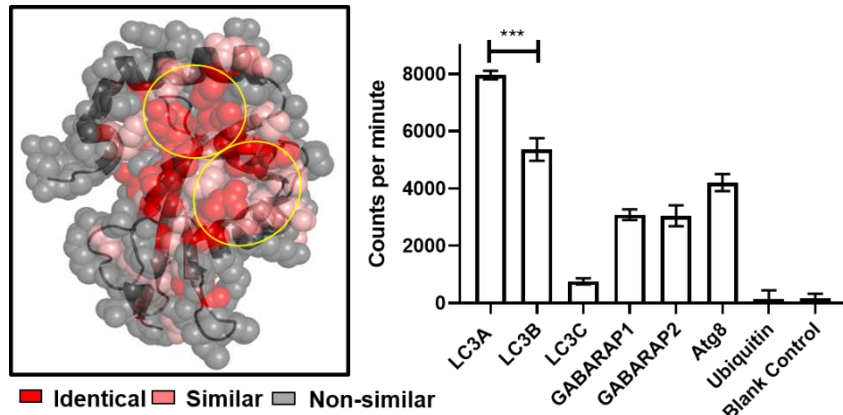
orders of magnitude (11).

We evaluated the protease stability of both cyclic and linear

SUPR4B1W and as well as a variant where the N-methyl alanine residues is replaced with alanine (SUPR4B1W8A). SUPR peptides were incubated for increasing time with agarose-immobilized proteinase-K and subjected to analysis by HPLC. SUPR4B1W was found to have a half-life in proteinase-K of 110 minutes,

while the linearized version of the peptide was found to have a half-life of 57 minutes (**Figure 3**). Removing the N-methyl-L-alanine dramatically increased susceptibility to proteolysis; SUPR-4B1W8A was completely degraded within 60 minutes of incubation with proteinase-k (half-life ~ 6 min). Based on these data, it appears that N-methyl-L-alanine is a major driver of protease stability, as substitution with L-alanine completely abrogates resistance to proteinase-K degradation. Previous SUPR mRNA display selections suggest that while incorporation of a single N-methyl amino acid moderately improves protease resistance, dramatic improvements in

protease stability (i.e. order of magnitude) are driven by multiple N-methyl residues (11). Indeed,



SUPR4B1W incorporates two N-methylated residues: the N-methyl-L-

Figure 5: SUPR4B1W Selectivity for LC3 Homologs. **A)** Crystal structure of LC3 (5CX3¹⁴⁶) showing the extent of residue conservation between LC3A, LC3B, LC3C, GABARAP1, GABARA2, and Atg8. The W and L sub-sites are highly conserved (circled in yellow). **B)** SUPR4B1W was immobilized on neutravidin-acrylamide and incubated with [³⁵S]-labeled LC3 homologs (LC3A, B, and C along with GABARAP L1 and L2, Atg8 (the yeast ortholog of LC3) and ubiquitin. SUPR4B1W showed modest selectivity for LC3A and LC3B compared with all other homologs and orthologs. No binding to ubiquitin was observed.

alanine incorporated at position 8 and the proline at position 2. When considered alongside the fluorescence polarization binding data, we can conclude that incorporation of N-methyl-L-alanine was primarily driven by selection for protease resistance, not selection for binding affinity.

SUPR4B1W Selectivity for LC3 Homologs

Fluorescence polarization assays showed that SUPR-4B1W binds to LC3B with an affinity similar to that of the selection target, LC3A. This is not entirely unsurprising, as LC3A and LC3B share a high degree of sequence similarity, particularly in the regions that define the protein-binding hot spot of each protein (**Figure 4A**). We sought to determine whether SUPR4B1W, with its non-canonical LIM, exhibits binding for other Atg8 mammalian orthologues or if binding was specific for LC3A/LC3B. Open reading frames (ORFs) for LC3A, LC3B, LC3C, GABARAP1, GABARAP2, Atg8, and Ubiquitin were transcribed into mRNA *in vitro* and translated *in vitro* in the presence of [³⁵S]-Methionine. SUPR4B1W was biotinylated and immobilized on neutravidin-acrylamide resin and the radiolabeled translation products were incubated with the resin. SUPR4B1W showed the highest binding to LC3A followed closely by LC3B (**Figure 4B**), an observation in line with our fluorescence anisotropy binding data. Moderate binding was also observed for both isoforms of GABARAP as well as Atg8 (the yeast ortholog of LC3). We observed virtually no binding by LC3C, which can be explained by LC3C's strong preference for the LVV motif which is not found in SUPR4B1W(98). SUPR4B1W showed no affinity for ubiquitin suggesting that the peptide binds to the LC3 hot spot (defined by the W and L sub-sites) rather than the core ubiquitin fold.

Autophagy-related proteins that contain canonical LIMs often show affinity for multiple isoforms of LC3 as well as isoforms of GABARAP, though affinity for each isoform varies (98,146). There also exists a GABARAP Interacting Motif (GIM)—(W/F)-(V/I)-X-V—which confers high selectivity for GABARAP proteins(133). Given

its small size and non-canonical LIM, the isoform selectivity of SUPR4B1W is very much in line with previously described linear LIM peptides.

SUPR4B1W is internalized into cells and co-localizes with punctate LC3 after starvation

Before assessing its potential as a therapeutic inhibitor of autophagy, we sought to validate the uptake of SUPR4B1W in human cell lines. We utilized copper-catalyzed click chemistry to conjugate the rhodamine derivative ROX-azide to SUPR4B1W via the side chain of a C-terminal propargylglycine residue. HeLa cells stably expressing eGFP-LC3B were grown in media supplemented with SUPR4B1W-ROX (500 nM) for 24 hours. After 24 hours, cells were starved for 2 hours to induce autophagy prior to confocal microscopy imaging. Induction of autophagy in this cell line results in a diffuse to punctate GFP staining pattern reflecting transition of diffuse cytosolic LC3-GFP to autophagosomes. SUPR4B1W-ROX is taken up by both unstarved (**Figure 5A**) and starved (**Figure 5B**) HeLa-

Figure 6: SUPR4B1W co-localizes with LC3 in starved HeLa cells. SUPR4B1W-ROX was incubated with HeLa cells expressing GFP-LC3 (green) in normal media (**A**) or starvation media (**B**) and visualized by confocal fluorescence microscopy. After starvation, the EGFP-LC3 transitions from diffuse to punctate staining indicating induction of autophagy. Significant overlap (yellow) of red and green puncta in starved cells indicates co-localization of LC3 and SUPR4B1W inside the cell. **C**) M1 and M2 co-localization coefficients were calculated for three fields of starved and unstarved cells. The M2 coefficient (co-localization green signal with red signal) increases after starvation. Scale bars represent XX μ m.

eGFP-LC3 cells, and in both cases displayed a punctate pattern suggesting an endocytotic/pinocytotic mechanism of uptake (147). To quantify the extent of colocalization between SUPR4B1W-ROX and GFP-LC3 puncta we calculated Manders' M1 and M2 colocalization coefficients for three fields of both starved and unstarved cells (**Figure 5C**). The M1 coefficient gives the percentage of pixels in the red channel (SUPR4B1W-ROX) that overlap with pixels in the green channel (eGFP-LC3). The M2 coefficient gives the percentage of pixels in the green channel that overlap pixels in the red channel. Starvation increases the M2 coefficient suggesting an increased co-localization of LC3 puncta with SUPR4B1W-ROX after starvation-induced autophagy. These data support cell uptake of SUPR4B1W and co-localization with intracellular LC3.

SUPR peptides sensitize resistant cell lines to cisplatin *in vitro*.

One of the overarching goals of this project was to produce cyclic peptide autophagy inhibitors that re-sensitized tumors to frontline chemotherapeutics. Previous reports have shown that induction of autophagy is correlated with cisplatin resistance in many human ovarian cancer cell lines including SKOV3, OVCAR8, Hey, CAOV3, and OVCA420. Cisplatin activates extracellular signal-regulated kinase (ERK) and promotes autophagy induction (89,148). Inhibition of MAPK/ERK signaling blocks autophagy induction and enhances cisplatin-induced apoptosis. This suggests that targeting cisplatin-induced autophagy may be a viable strategy for overcoming chemotherapy resistance in ovarian cancer.

To determine the utility of SUPR4B1W in this context, two platinum-resistant epithelial ovarian cancer cell lines—OVCAR8 and HEY—were subjected to

treatment with combinations of cisplatin and SUPR peptide for 48 hours before cellular viability was evaluated by MTT assay (Figure 6A, B). In both OVCAR8 and Hey, chloroquinine and cyclic SUPR4B1W significantly reduced cell viability in the absence of

cisplatin

whereas

linear

SUPR4B1W

did not

(Tukey's

HSD, $p <$

0.05). Both

chloroquinine

and cyclic

SUPR4B1W

reduced cell

viability more

effectively in

the presence of

cisplatin in both

cell lines ($p <$

0.0001). In

OVCAR8 cells,

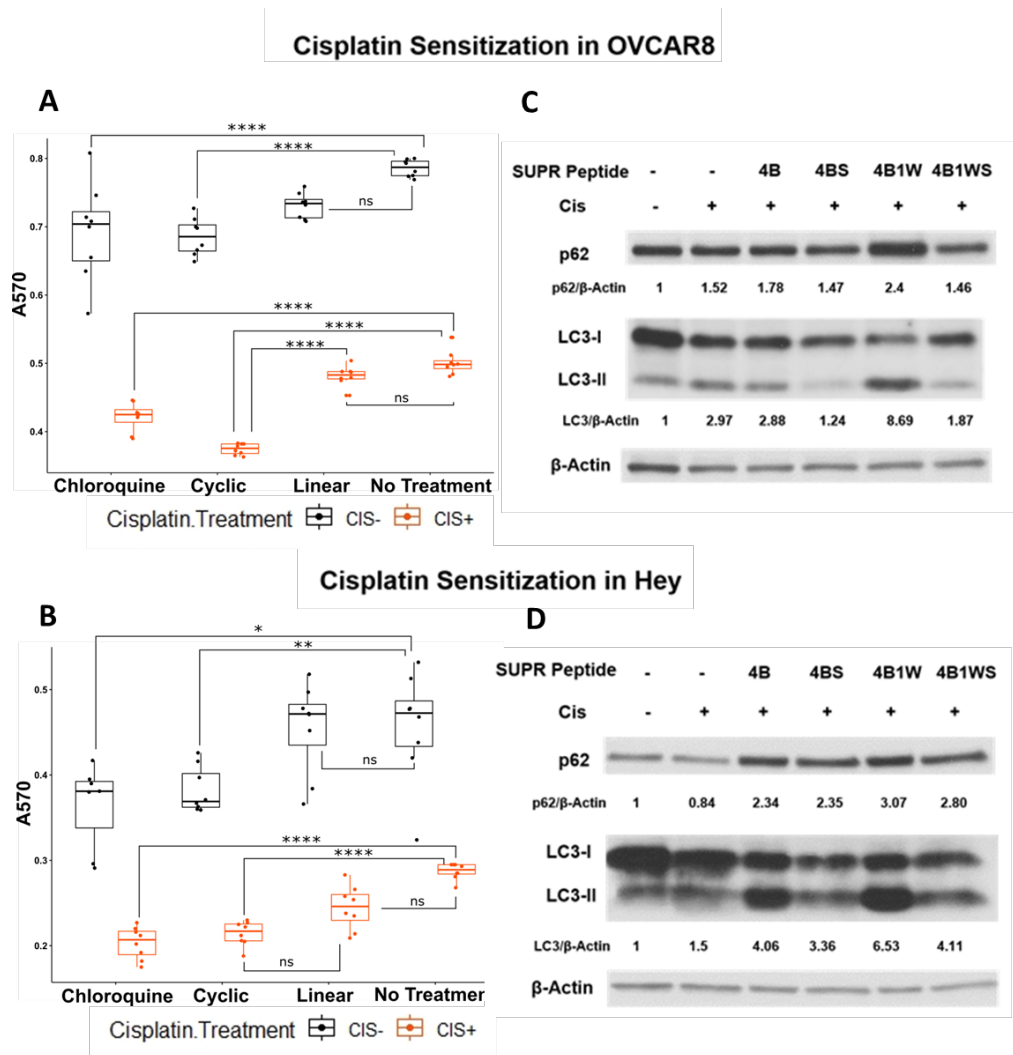


Figure 7: SUPR4B1W sensitizes ovarian cancer cells to cisplatin and results in p62 accumulation and LC3-II/LC3-I perturbation. Treatment of OVCAR8 (A) and HEY (B) ovarian cancer cells with SUPR4B1W and cisplatin significantly reduces cell viability after 48 h relative to cisplatin alone. A linearized version of SUPR4B1W showed no significant effect on viability in the presence or absence of cisplatin. Incubation of cisplatin-treated OVCAR8 cells (C) and Hey cells (D) with SUPR4B1W resulted in accumulation of p62 and an increase in the LC3II/LC3I ratio indicating inhibition of autophagy while a scrambled version of SUPR4B1W showed no effect. SUPR4B only showed perturbation of the LC3II/LC3I ratio in Hey cells and did not cause accumulation of p62 in either cell line.

cisplatin and the cyclic SUPR peptide interacted synergistically to decrease cell viability more than either cisplatin alone ($p < 0.001$) or chloroquine combined with cisplatin ($p = 0.0002$). Treatment with scrambled SUPR4B1W resulted in no change in viability compared to untreated. A linearized version of SUPR4B1W showed no significant effects on viability alone or in conjunction with cisplatin (Tukey's HSD, $p > 0.05$). These data suggest that viability changes are not the result of bulk uptake of non-specific peptide into cells, but rather a specific interaction mediated by SUPR4B1W. Enhancement of cisplatin efficacy was also seen in other ovarian cell lines (SKOV3, OVCAR5), triple-negative breast cancer cell lines (MDA-MB-231), and pancreatic cancer cell lines (Mia-PaCa-2, Panc1). These data suggest that cyclic SUPR4B1W, rather than a linearized or scrambled version, inhibits autophagy in cancer cell lines and sensitizes them to cisplatin-mediated cytotoxicity.

Western blots of treated cells show that combining cisplatin with both SUPR4B1W leads to a dramatic accumulation of lipidated LC3-II and p62 in both OVCAR8 and HEY cell lines (**Figure 6C, D**). Comparatively, the combination of CQ and cisplatin induces an accumulation of p62 and a dramatic reduction of cytosolic LC3-I and LC3-II. Cells undergoing autophagy typically show decreased levels of p62 as the protein is degraded in the lysosome following autolysosome fusion, and accumulation of p62 indicates disruption of autophagic flux(100). Taken together, increased p62 and LC3 levels provides a strong indication that SUPR4B1W inhibits cisplatin-induced autophagy in cell culture. Treatment with a scrambled version of SUPR4B1W showed no significant effects on p62 accumulation or LC3 lipidation indicating that this effect is sequence-dependent. Notably, SUPR4B showed some

effect on the LC3II/LC3I ratio in Hey cells but not in OVCAR8. SUPR4B showed no effect on p62 accumulation in either cell line which is consistent with its reduced LC3 affinity relative to SUPR4B1W.

SUPR4B1W sensitizes OVCAR8 tumors to carboplatin in nude mice

Given the encouraging cell-based data, we next sought to determine if SUPR4B1W could sensitize tumors to carboplatin treatment in an orthotopic mouse model. Cisplatin resistance in ovarian cancer is frequently observed in recurrent, metastatic nodules that appear throughout the peritoneum (149). Intraperitoneal injection of OVCAR8 cells provides a suitable model for recurrent, resistant metastatic

disease in nude mice. When injected, OVCAR8 forms tumor nodules throughout the

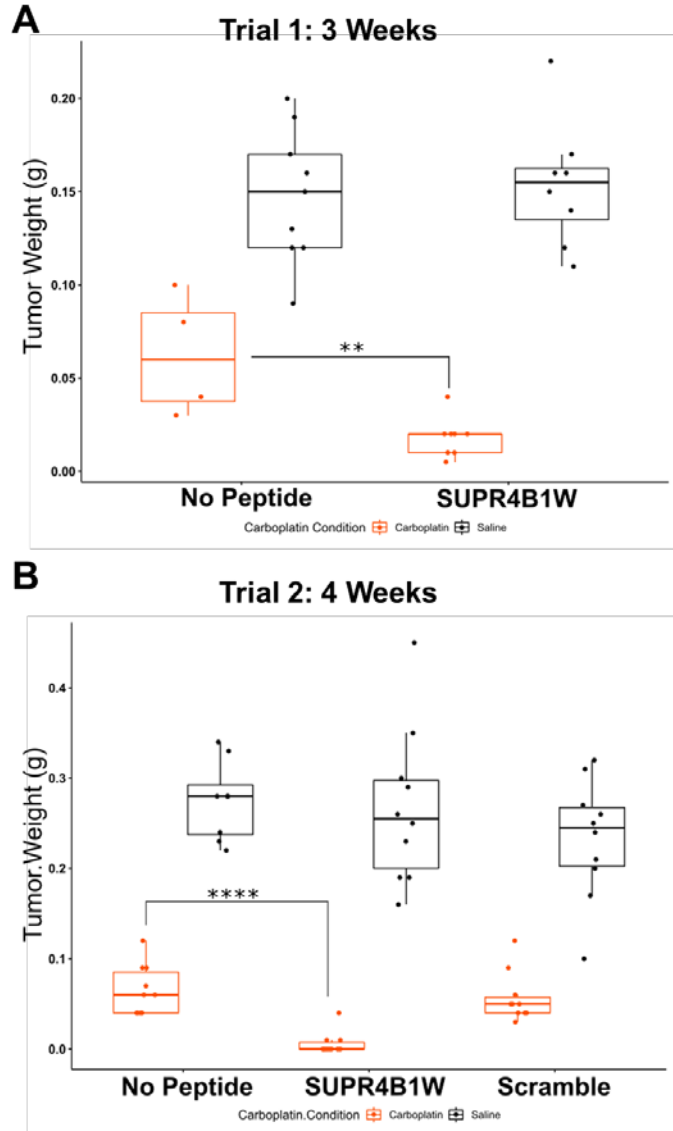


Figure 8: SUPR 4B1W Inhibits Tumor Growth *in vivo*. **A)** OVCAR8 cells were injected into the peritoneum of nude mice (n = 8 per group) followed by i.p. treatment with carboplatin (25 mg/kg, 3 times per week), SUPR4B1W (10 mg/kg, 3 times per week), or a combination of the two for 3 weeks. SUPR4B1W + carboplatin dramatically reduced tumor mass relative to carboplatin alone while SUPR4B1W alone had no effect. **B)** The same therapeutic trial was carried out for 4 weeks with the introduction of a scrambled version of SUPR4B1W. The combination of SUPR4B1W and carboplatin almost completely eliminated intraperitoneal growth in 4 weeks while the combination of carboplatin and a scrambled peptide showed no improvement relative to carboplatin alone.

abdominal peritoneum and gastrointestinal tract. To determine the effect of SUPR4B1W on tumor nodule formation, nude mice were IP-injected with 2 million OVCAR8 cells and subsequently treated 3 times weekly with combinations of carboplatin, SUPR4B1W, and chloroquine. At 3 weeks, the mice were sacrificed, the tumors were dissected, and total tumor mass for each treatment condition was evaluated (**Figure 7A**). Treatment with SUPR4B1W alone had no impact on tumor development (Tukey's HSD, $p = 0.9827$), but combining SUPR4B1W with carboplatin resulted in a significant reduction in total tumor mass compared to treatment with carboplatin alone (Tukey's HSD, $p = 0.0032$). This experiment was repeated, extending the treatment period to 4 weeks and treatment with a scrambled version of SUPR4B1W (**Figure 7B**). At 4 weeks, combined SUPR4B1W and carboplatin treatment again had a strong effect on tumor growth with 70% of mice in the SUPR4B1W+carboplatin group showing no observable tumor development. Combining scrambled SUPR4B1W with carboplatin resulted in no difference in total tumor mass compared to treatment with carboplatin alone (Tukey's HSD, $p = 0.9911$). These results provide a strong indication that SUPR4B1W selectively inhibits autophagy in tumors and may provide a potent lead compound for future therapeutic development.

Conclusions

We have employed SUPR peptide mRNA Display to design SUPR4B1W, a potent, cell-permeable inhibitor of the LC3 protein. This macrocyclic peptide shows mid-nanomolar affinity for LC3A and LC3B and selectivity for LC3A/B over other Atg8 orthologs. Binding studies revealed the cyclization contributes modestly, but

significantly, to the binding energetics of SUPR4B1W while the non-proteogenic N-methylalanine is dispensable for affinity. In contrast, the N-methyl alanine residue is absolutely essential for protease resistance while the contribution of cyclization to stability is modest. These results suggest that the incorporation of N-methyl amino acids is driven primarily by selection for protease resistance rather than target affinity.

Fluorophore-tagged SUPR4B1W is readily taken up in HeLa cells and displays a punctate staining pattern consistent with endocytosis or pinocytosis. While heavily N-methylated cyclic peptides have previously been shown to cross the cell membrane by diffusion (139), this mechanism of uptake would presumably have resulted in a diffuse staining pattern, particularly in unstarved cells where LC3 is distributed evenly throughout the cytosol. Given the relatively low fraction of N-methylation (25% of the randomized region) and the presence of an aliphatic macrocyclic bridge, we propose that the mechanism of uptake may be similar to that of stapled peptides which are also believed to transit the cell membrane by endocytosis and/or pinocytosis(150). While it has also been proposed that stapled peptides enter the cell following membrane disruption(151,152), we found no evidence of this mechanism by microscopy or by the appearance of non-specific toxicity in cell culture and animal models. Future studies will address the effect of N-methylation, charge, and hydrophobicity on the mechanism and extent of SUPR peptide cell penetration.

SUPR4B1W sensitizes multiple cell lines to cisplatin treatment and results in accumulation of p62 and significant perturbation of the LC3II/LC3I ratio. These

results strongly suggest that SUPR4B1W disrupts the PPIs of LC3 inside the cell and inhibits autophagosome maturation. Accumulation of LC3II, the lipidated form of LC3, may indicate that SUPR4B1W inhibits Atg4 binding and subsequent proteolytic recycling of LC3II – a conclusion supported by *in vitro* data showing inhibition of Atg4B proteolysis by SUPR4B1W. Inhibition of LC3II recycling could arrest autophagic flux by attenuating the rate of formation of new autophagosomes, although this mechanism of action remains to be proven experimentally.

The combination of SUPR4B1W and carboplatin results in almost complete inhibition of tumor outgrowth *in vivo* suggesting that this compound could be administered in an adjuvant setting to enhance the efficacy of platinum-based therapies or to prevent the outgrowth of platinum-resistant disease. Although the combined effect of SUPR4B1W and cisplatin was also observed in cell culture, the effect size was significantly lower relative to the *in vivo* models. This divergence may be the result of context. It has previously been shown that induction of autophagy in ovarian cancer cell lines results in a strikingly different survival phenotype than autophagy induction in the corresponding animal models (80). This was attributed to the effects of a relatively nutrient-poor tumor microenvironment compared to the nutrient-rich conditions found in cell culture. Alternatively the striking effect of SUPR peptide/carboplatin combinations *in vivo* may be the result of both chemotherapeutic effects and enhancement of the innate immune system. Although athymic nude mice were used to generate the orthotopic models, these mice still retain a functional innate immune system(153,154). Previous work in breast cancer (155) and renal cell carcinoma (RCC) (156) models has shown that

autophagy inhibition sensitizes these tumors to natural killer (NK)-mediated cell killing by preventing degradation of secreted granzyme. Inhibition of autophagy in macrophages has also been shown to alter polarization from M2 to M1 which could facilitate a pro-inflammatory, anti-tumoral response (157). Future studies will be carried out to deconvolute the effect of SUPR peptide-mediated autophagy inhibition on tumor viability, drug resistance, and the immune response.

CHAPTER THREE

THE ARHI MODEL OF INDUCIBLE AUTOPHAGY IN OVARIAN CANCER

This chapter is based in part upon sections of Ornelas, A., McCullough, C.R., Lu, Z. et al. Induction of autophagy by ARHI (DIRAS3) alters fundamental metabolic pathways in ovarian cancer models. BMC Cancer 16, 824 (2016).

<https://doi.org/10.1186/s12885-016-2850-8>

Introduction

Aplasia Ras homolog member I (ARHI also known as DIRAS3) is an imprinted tumor suppressor gene that is known to exhibit reduced or total loss of expression in breast(158), lung (159), hepatocellular (160), and pancreatic (161) carcinomas as well as greater than 60% of ovarian carcinomas (80,162). ARHI encodes for a small 26 kDa GTPase that is known to have great >50% homology with the various isoforms of RAS, a well-studied oncogene that frequently drives runaway growth signaling in carcinomas (163). ARHI blocks homodimerization of RAS and subsequent downstream growth signaling by forming heterodimers with RAS (164). Additionally, ARHI has been shown to inhibit the AKT-PI3K-mTOR pathway, the inhibition of which is a known initiator of autophagy. Re-expression of ARHI in ovarian carcinoma provides an excellent model of inducible autophagy and a powerful tool to study the impact of autophagy on tumor metabolism(80). Re-expression of ARHI under the control of doxycycline in the ovarian carcinoma cell lines SKOv3 and OVCAR8 induces highly elevated levels of autophagic flux resulting in non-apoptotic cell death with 72 hours of induction. We sought to gain a better understanding of the impact of ARHI-induced autophagy on metabolic

dysfunction and discovered that ARHI-mediated autophagy induces significant changes in mitochondrial membrane potential and generation of reactive oxygen species (ROS), a potent cellular stressor. When autophagic SKOv3-ARHI and OVCAR8-ARHI cell lines are treated with SUPR4B1W—a macrocyclic SUPR peptide inhibitor of LC3 PPIs—cell death is no longer observed and cells return to a normal viability phenotype at 72 hours post autophagy induction.

Materials and Methods

Cell Culture

ARHI-inducible SKOv3-ARHI ovarian cancer cells were maintained in McCoy's 5A medium supplemented with 10% tetracycline-free fetal bovine serum, 2 mM L-Glutamine, and 1% (v/v) penicillin-streptomycin. ARHI-inducible OVCAR8-ARHI ovarian cancer cells were maintained in RPMI 1640 medium supplemented with 10% tetracycline-free fetal bovine serum, 2 mM L-Glutamine, 1 mM Na-Pyruvate, and 1% (v/v) penicillin-streptomycin.

Uptake of Mitotracker Red FM by Fluorescence Microscopy

SKOv3-ARHI cells were seeded into 96 well plates and treated with 1 µg/ml Dox for 48 hours or grown untreated in complete media for 48 hours. Cells were treated with 50 nM MitoTracker Red FM (Invitrogen) for 45 minutes in FBS free media. Cells were then washed with 1x PBS (Hyclone) and immediately imaged by fluorescence microscopy ($\lambda_{ex} = 581 \text{ nm}$, $\lambda_{em} = 644 \text{ nm}$) using a Biotek Cytation5 Cell Imaging Multi-Mode Reader

Uptake of TMRM and H2DCFDA by Flow Cytometry

SKOv3-ARHI cells were treated with 1 µg/ml Dox for 24 and 48 h or with 50 nM Rapamycin for 24 h. Cells were then incubated with 20 nM tetramethyl rhodamine methyl ester (TMRM) in FBS-free media for 45 min, washed twice with phosphate buffered saline, and resuspended in FBS-free media. The mean fluorescence intensity for 10,000 cells was obtained by flow cytometry.

SKOv3-ARHI and SKOv3 (parental) cells were treated with Dox (1 µg/ml) for 12, 24 and 48 h. In a separate experiment SKOv3-ARHI cells were treated with Dox (1 µg/ml) for 48 h with and without BPTES (1 µM). The cells were then washed and stained with 5 µM H2DCFDA and analyzed by flow cytometry to obtain the mean fluorescence intensity. Triplicate samples were used for each experimental condition and analysis of the results was performed in GraphPad. The statistical significance was determined by unpaired, two-tailed t-test in GraphPad (*, $p < 0.05$; **, $p < 0.01$)

TOM20 Staining by Flow Cytometry

SKOv3-ARHI cells were seeded into a 75 cm² flask and allowed to reach confluence. Cells were treated with 1 µg/ mL of Doxycycline for different time points as previously discussed. After treatment, cells were trypsinized and harvested at 500xg for 10 min. Cells were then fixed in 3 % formaldehyde and permeabilized with 0.1 % Triton X100. Cells were then counted, aliquoted and incubated in 2 µg of TOM20 antibody (Santa Cruz Biotechnology) for 40 min. Cells were then washed and incubated in F(ab')₂- Goat anti Rabbit IgH (H + L) Secondary Antibody, Alexa Fluor® 488 conjugate (Thermo Scientific).

Effect of Autophagy inhibitors on Cellular Viability following ARHI induction

SKOv3-ARHI and OVCAR8-ARHI cells were seeded into 96-well plates at a density of 5,000 cells per well and treated with Dox for 24, 48, or 72 hours or grown for 72 hours without Dox treatment. Treatment media was replaced daily. Cells underwent simultaneous treatment with SUPR4B1W (50 μ M), SUPR4B1W scramble (50 μ M), Chloroquine (5 μ M), or were untreated. Treated cells were given 50 μ M SUPR4B1W in full media for 24, 48, or 72 hours. After 72 hours, cells were washed with 1X PBS and viability was measured by MTT assay. The statistical significance of difference in viability was determined by unpaired, two-tailed t-test in GraphPad (*, $p < 0.05$; **, $p < 0.01$)

Results and Discussion

ARHI expression modulates mitochondrial membrane potential & intracellular oxidative state

Staining of SKOv3-ARHI cells with Mitotracker dye following induction of ARHI revealed a significant decrease in dye uptake suggesting a loss of mitochondrial membrane potential, potentially induced by depletion of mitochondria through autophagic flux (**Figure 1A**). To quantitate this effect, SKOv3-ARHI cells were treated with Dox followed by the Nernstian fluorescent probe TMRM and analyzed by flow cytometry. Uptake of cationic Nernstian probes like TMRM is dependent on mitochondrial membrane potential, and the intensity of fluorescence generated by the probe can be used as a semi-quantitative measure of mitochondrial membrane potential. Treatment with Dox resulted in a decrease in TMRM uptake which was most pronounced at 24 h post-induction (**Figure 1B**). In

contrast, treatment with rapamycin had no effect on TMRM uptake. In order to determine if low TMRM uptake was being driven by low mitochondrial membrane potential or by a decrease in the number of mitochondria, SKOv3-ARHI cells were fixed and permeabilized following induction with Dox for 12, 24, and 48 h. The cells were then stained for the presence of the TOM20 receptor of the mitochondrial outer membrane preprotein translocase and analyzed by flow cytometry. Significantly lower Tom20 signal was observed after 12 h of Dox induction suggesting a decrease in the mitochondrial mass following ARHI induction (**Figure 1C**). We also sought to determine the effect of ARHI induction on the intracellular oxidative state using the oxygen-sensitive dye H2DCFDA. Induction of ARHI was found to increase H2DCFDA uptake by flow cytometry by almost 3-fold after 48 h (**Figure 1D**). This result is in good agreement with results of previous work. In contrast, parental SKOv3 cells showed no statistically significant change in H2DCFDA following treatment with Dox indicating that changes in intracellular redox state were the result of ARHI expression. Finally, we measured H2DCFDA uptake following ARHI induction and BPTES treatment for 48 h (**Figure 1E**). BPTES is a selective inhibitor of Glutaminase GLS1, a critical component in glutamine metabolism. We found that BPTES treatment resulted in decreased H2DCFDA uptake in Dox-induced SKOv3 cells while BPTES treatment alone resulted in no statistically significant change.

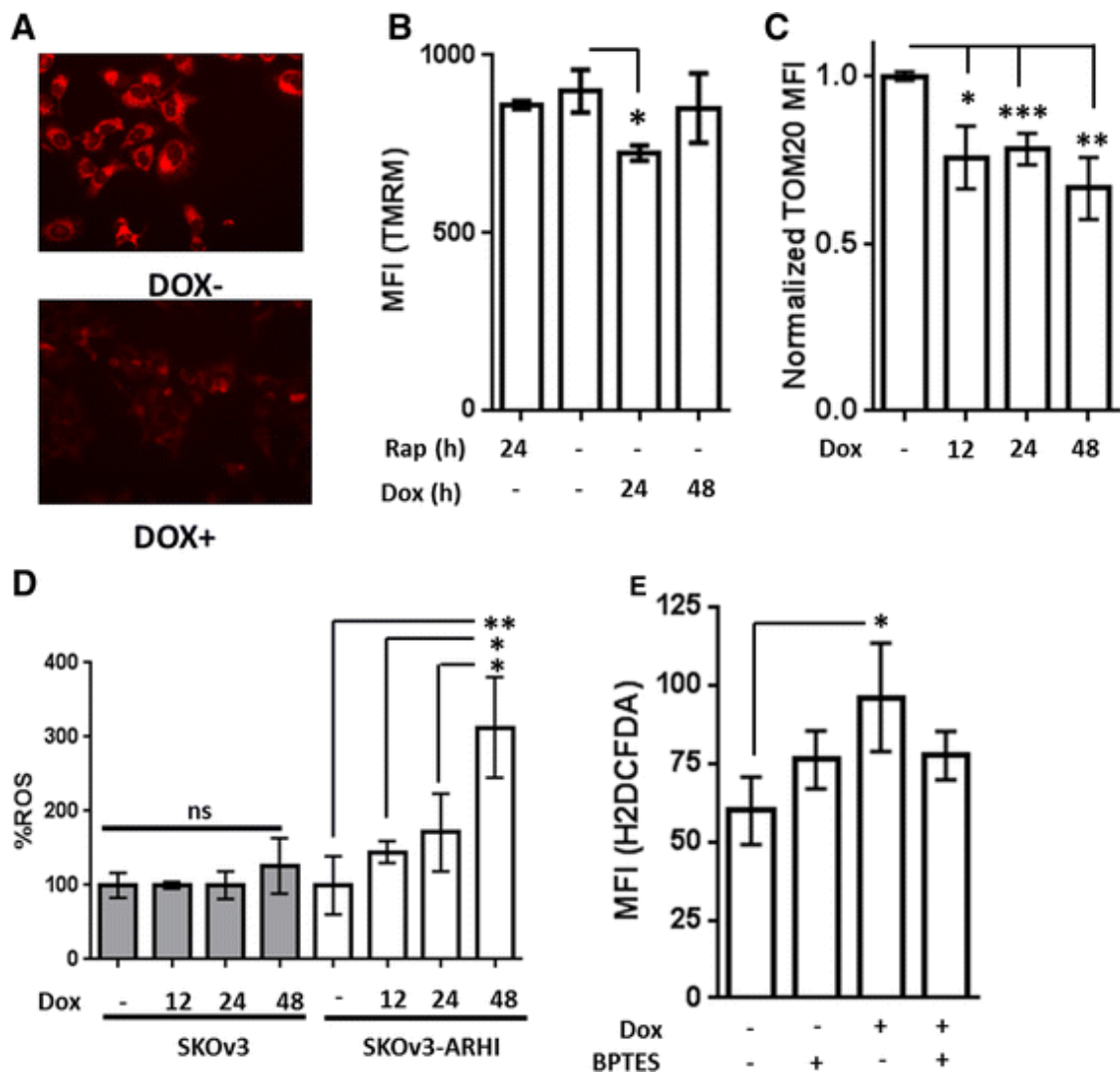


Figure 9 ARHI Expression alters Mitochondrial Membrane Potential and ROS in SKOv3-ARHI. **A)** SKOv3-ARHI cells were treated with and without Dox followed by staining with Mitotracker Red FM and visualized by fluorescence microscopy at 24 h. **B)** SKOv3-ARHI cells were treated with Dox or Rapamcyin for the indicated times followed by tetramethyl rhodamine methyl ester (TMRM). The mean fluorescence intensity (MFI) was obtained by flow cytometry. **C)** SKOv3-ARHI cells were treated with Dox for 48 h, followed by fixation in 3 % paraformaldehyde and permeabilization with 0.1 % Triton X-100. Cells were then stained with TOM20 antibody (Santa Cruz Biotechnology) and a secondary goat Anti-rabbit IgG conjugated to AF488® and analyzed by flow cytometry **D)** SKOv3 (parental) and SKOv3-ARHI cells were treated with Dox for the indicated times followed by H2DCFDA and analyzed by flow cytometry. The resulting MFI values were normalized to the Dox- value in either the parental or ARHI-transfected cell line. **E)** SKOv3-ARHI cells were treated with Dox for 48 h with and without BPTES (1 μ M) followed by staining with H2DCFDA and analysis by flow cytometry

Treatment with SUPR4B1W restores viability following ARHI expression

Induction of ARHI expression in SKOv3-ARHI and OVCAR8-ARHI by addition of Dox (1µg/mL) to culture media results in extreme autophagic flux that causes a marked reduction in cellular viability within 48 hours. Previous work suggests that this cell death occurs through apoptotic and non-apoptotic pathways due to a depletion of essential cellular proteins and organelles by autophagy. We sought to determine whether inhibition of autophagy following ARHI expression could restore cellular viability. As described in Chapter 2, SUPR41BW is a macrocyclic, protease-resistant peptide that has high affinity and selectivity for LC3. SUPR4B1W disrupts protein-protein interactions (PPIs) necessary for early autophagosome maturation, and has shown evidence of enhancing the effect of platinum-based chemotherapeutics in models of metastatic, resistant ovarian carcinoma. SKOv3-ARHI and OVCAR8-ARHI were induced for autophagy for 24, 48, or 72 hours and split into groups that received concurrent treatment with SUPR4B1W (50 µM), SUPR4B1W scramble (50 µM), Chloroquine (CQ) (5 µM), or no treatment. After 72 hours, cellular viability was measured by MTT assay. Cells that did not undergo autophagy induction showed no change in viability (**Figure 2A & 2B**) when treated with SUPR4B1W or its amino acid sequence scrambled counterpart suggesting that treatment with SUPR peptide alone is non-toxic. Treatment with CQ in the absence of ARHI induction resulted in a significant reduction in cellular viability in OVCAR8-ARHI cells after 72 hours of treatment (**Figure 2B**). CQ is a lysosomotropic agent that non-specifically accumulates in acidic vesicles where it raises vesicular pH inactivating lysosomal hydrolases. Both SKOv3-ARHI and OVCAR8-ARHI cells

demonstrate a return to normal levels of cellular viability at 72 hours post-induction when combined with SUPR4B1W treatment (**Figure 2C & 2D**). Combined treatment with scrambled SUPR4B1W or CQ shows no statistically significant restoration of viability. Combined treatment of CQ with DOX induction results in reduced cellular viability in OVCAR8-ARHI compared to induction alone, which is expected as OVCAR8-ARHI cells appear to be sensitive to prolonged CQ treatment even under normal growth conditions. While both CQ and SUPR4B1W appear to inhibit autophagy, their mechanisms of action differ dramatically. CQ acts late in the development of autophagosomes and in fact does not directly impact the autophagy machinery at all. CQ only acts after the autophagosome has fused with the lysosome to prevent final degradation of the autophagosome's contents. Those contents—such as essential organelles like mitochondria—are still sequestered inside vesicles where they cannot carry out their normal cellular functions. Since ARHI expression results in cell death due to depletion of essential cytosolic machinery by autophagy, it stands to reason that CQ would not restore cellular viability since it cannot prevent the sequestration of organelles and proteins. As demonstrated in Chapter 2, SUPR4B1W disrupts LC3 PPIs necessary for autophagosome maturation both in vitro and in cells. We therefore hypothesize that SUPR4B1W impacts early autophagosome formation and maturation preventing essential cytosolic machinery from becoming isolated in functional vesicles.

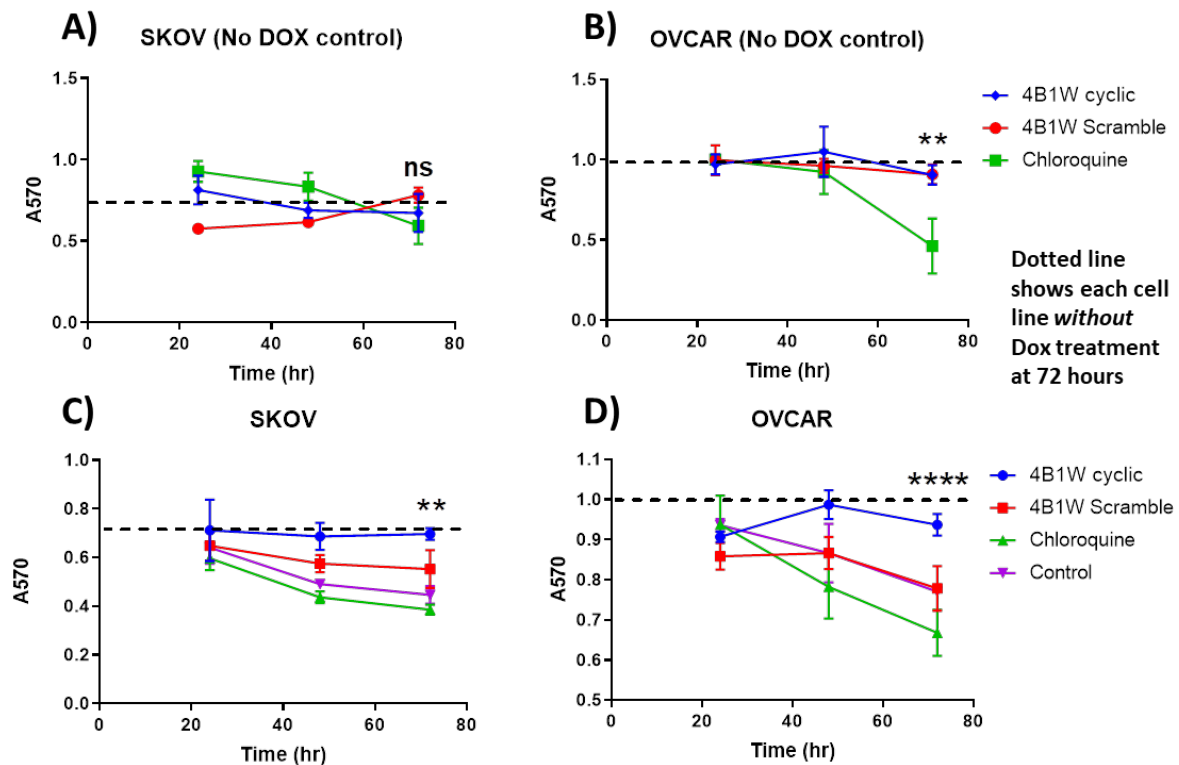


Figure 10 MTT assays of cellular viability in the ARHI expression model. **A)** SKOV3-ARHI and **B)** OVCAR8-ARHI cell lines show no impact on viability from SUPR peptide treatment in the absence of ARHI expression. CQ results in a significant reduction in cellular viability in OVCAR8-ARHI after 72 hours of treatment. **C)** SKOV3-ARHI and **D)** OVCAR8-ARHI cells show restoration of normal viability patterns after 72 hours of ARHI induction combined with SUPR4B1W treatment. SUPR4B1W scramble and CQ show no restoration of viability at 72 hours compared to induced cells that did not receive treatment

Conclusion

Inducible ARHI expression in ovarian carcinoma is a unique and powerful model that has provided numerous insights into both tumor development and altered cancer metabolism. This study has shown that ARHI expression fundamentally alters mitochondrial function in ovarian cell lines. We observed both reduced TMRM fluorescence and TOM20 signal by flow cytometry following ARHI induction, suggesting a decrease in cytosolic mitochondrial mass. Additionally, we observed that the generation of ROS increases following ARHI expression. Both reduced mitochondrial mass in the cytosol and increased ROS production could be explained

if ARHI-induced autophagy is resulting in the sequestration of mitochondria in autophagic vesicles and autolysosomes where they subsequently become dysfunctional. We hypothesize that this leads to increased ROS burden. Interestingly, while both ARHI expression and inhibition of glutamine metabolism through BPTES treatment result in increased ROS production, combined Dox and BPTES treatment resulted in less ROS production than Dox treatment alone. Further studies should focus on why inhibition of glutamine metabolism reduces ROS production in the context of ARHI-induced autophagy.

It has previously been established that ARHI expression leads to significant cell death within 48 hours, likely due to depletion of essential cellular machinery through highly increased autophagic flux. We demonstrated that treatment with SUPR4B1W concurrent with ARHI expression is able to abrogate this loss in cellular viability, possibly by disrupting the early formation and maturation of autophagosomes through the inhibition of LC3 PPIs. Autophagy inhibitors like CQ that disrupt end-stage degradation of autolysosome contents do not restore viability, suggesting that they act too late in the autophagic process to rescue viability. Further studies will focus on examining the impact of SUPR4B1W on early autophagosome development through the use of electron microscopy which is able to directly visualize autophagosomes and their contents. Additionally, further studies will examine the impact of SUPR4B1W on in vivo models of ARHI expression where it is known that ARHI expression results in transition to dormancy rather than cell death and increased autophagic flux is thought to be essential in mediating survival during dormancy.

CHAPTER FOUR

MULTI-WAVELENGTH PHOTOACOUSTIC VISUALIZATION OF HIGH INTENSITY FOCUSED ULTRASOUND LESIONS

This chapter is based upon Gray, J. P., Dana, N., Dextraze, K. L., Maier, F., Emelianov, S., & Bouchard, R. R. (2016). Multi-Wavelength Photoacoustic Visualization of High Intensity Focused Ultrasound Lesions. Ultrasonic Imaging, 38(1), 96–112. Copyright © 2016 SAGE Publications

<https://doi.org/10.1177/0161734615593747>

Introduction

High intensity focused ultrasound

High intensity focused ultrasound (HIFU) is a minimally invasive technique that has developed significantly over the last two decades for the treatment of benign and malignant conditions in soft tissues (165,166). HIFU treatments use ultrasound transducers with highly controlled beams to instantly achieve destructive temperatures at their focus. This technique has been used to treat targets that may be several centimeters below the skin surface, while preserving healthy tissue since hyperthermal therapy tends to occur at the focus of the beam (166). HIFU is of clinical interest for several conditions, including atrial fibrillation of cardiac tissue (167,168), central nervous system disorders of the brain (169), treatment of both benign and malignant solid tumors through thermal ablation (166), and enhanced drug delivery at treatment sites (170). In the United States, HIFU has been indicated for clinical treatment of uterine fibroids and malignant bone metastases (171).

Image guidance is employed during HIFU for treatment planning, tissue temperature, and assessment of tissue damage during and after treatment (i.e. estimating treatment margins) (166). Real-time image guidance has accommodated adaptive ablation planning, leading to increased efficacy of HIFU treatments and improved precision in estimating treatment margins (166). Imaging guidance for hyperthermal therapy has been provided by magnetic resonance (MRI) imaging, computed tomography (CT), and ultrasound (US), all of which have been able to elucidate anatomical structures and heating-probe location (172). Several of these techniques have demonstrated the capability to monitor tissue temperature changes, yet only MRI is used as a standard-of-care technique for image guidance during clinical treatments (173,174).

Photoacoustic imaging

Photoacoustic (PA) imaging is a relatively novel technique that is gaining attention due to its feasibility of implementation as a point-of-care imaging solution, its molecular sensitivity, and its ready compatibility with existing US technology (175). PA imaging can be achieved through extracorporeal or interstitial application of near-infrared (NIR) laser pulses, which are absorbed by endogenous chromophores or exogenous contrast agents (176,177). Due to the “optical window,” in which optical absorption by water, fat, and blood decreases dramatically in the NIR region (650-1100 nm), imaging depths of several centimeters can be achieved in soft tissues (178). Photon energy absorbed by chromophores is converted into mechanical energy through a rapid thermal expansion, which results in the

generation of an acoustic transient that propagates through soft tissue and may be detected by a standard US transducer at the tissue surface (175,176). Detected signals can then be used to estimate a map of optical absorption with sub-millimeter spatial resolution. Since PA signals are detected using an ultrasonic transducer, PA images can be co-registered with US images (175). These photoacoustic-ultrasonic (PAUS) images allow for the presentation of anatomical information alongside estimated optical absorption, and thus molecular composition, of the tissue.

The amplitude of PA pressure waves, $p_0(\mathbf{r}, T, \lambda)$, generated as a result of optical absorption by chromophores in tissue, are dependent on the speed of sound in tissue ($v_s(T)$ [cm s⁻¹]), a temperature-dependent volume expansion coefficient ($\beta(T)$ [K⁻¹]), the isobaric heat capacity in tissue ($C_p(T)$ [J kg⁻¹ K⁻¹]), the optical absorption coefficient of the tissue ($\mu_{abs}(\mathbf{r}, \lambda)$ [cm⁻¹]), and the optical fluence ($\Phi(\mathbf{r}, \lambda)$ [J cm⁻²]) as (175–177)

$$p_0(\mathbf{r}, T, \lambda) = \left(\frac{\beta(T)v_s^2(T)}{C_p(T)} \right) \mu_{abs}(\mathbf{r}, \lambda) \Phi(\mathbf{r}, \lambda). \quad \text{Eq. 1}$$

Contrast in PA images arises from variations in the optical absorption coefficient, which depends on both the concentration of chromophores in tissue and the wavelength of the laser source. Due to the wavelength dependence of the optical absorption coefficient, multi-wavelength photoacoustic imaging can be performed by varying the wavelength of the laser through the entire NIR region in order to estimate the optical absorption properties of the tissue (175,179). Varying the location of the PAUS transducer or using a 2D array and obtaining PA signals at several wavelengths allows for the generation of a multi-wavelength 3D PAUS volume.

Additionally, the temperature dependence of pressure wave generation may allow for real-time monitoring and characterization of temperature change during ablation (180–183).

Current image-guidance methods

Image guidance techniques greatly improve the outcome of HIFU treatments by allowing physicians to more accurately and completely estimate treatment margins, yet existing imaging modalities are not entirely satisfactory for treatment guidance (172,184,185). Currently, image guidance of HIFU treatments is performed using several standard imaging modalities. Traditional pulse-echo B-mode US provides excellent anatomical information and can provide short-term identification of hyperechoic regions of tissue corresponding to microbubble formation at the site of the HIFU focus; however, it cannot provide quantification of lesion extent (186). Elastography can be used to assess and characterize induced lesions, but can be difficult to implement *in vivo* and provide a significant number of false-positives (187). Magnetic resonance imaging (MRI) allows for excellent identification of treatment targets, treatment planning, and real-time tracking of relative temperature changes at the site of ablation through MRI thermography (173,174,188), but it is limited by the high cost and equipment incompatibility imposed by high magnetic field strengths. PA imaging is a promising modality for image guidance of HIFU therapies because of its ready compatibility with existing technology and capability to monitor target and healthy tissue during ablation with sub-millimeter spatial

resolution. This level of spatial resolution in fact exceeds the spatial resolution of existing temperature MRI guidance techniques (1-2 mm) (166,189).

HIFU guidance with PA imaging

PA imaging provides several unique qualities that make it promising as an alternative to existing image-guidance techniques for HIFU. PA imaging is capable of both thermography and spectroscopy (180,190,191), allowing for real-time assessment of temperature changes and tissue state. In practice, conventional US techniques such as Doppler imaging or microbubble-contrast perfusion assessment can also be applied concurrently with PA imaging to assess nearby critical structures, such as vessels (175).

Previous studies of HIFU ablations *in vitro* and *in vivo* using PA imaging have shown that PA imaging is capable of providing image contrast in the ablation region (192–197). This change in contrast at the ablation site may be attributed to a change in the concentration of chromophores in the tissue as a result of heating (198). However, single-wavelength methods typically fail to provide enough information to reliably quantify the precise position and dimensions of HIFU lesions. Studies using radio-frequency ablation have shown that multi-wavelength PA imaging is capable of detecting changes in the concentration of chromophores—specifically in the concentration of deoxy-hemoglobin (Hb)—following thermal ablation and that these multi-wavelength methods allow PA imaging to identify an optical absorption spectrum specific to ablated tissue and distinct from the typical Hb spectrum (191,194). In this study, we use the previously described technique (191,194) in an

in vitro environment following HIFU and water-bath ablation of cardiac and liver tissue samples. 2D and 3D multi-wavelength PA data of ablated tissue samples is then correlated to these two absorption spectra to create Tissue Characterization Maps (TCM), which are used to quantitate lesion size for comparison to stained gross pathology. Additionally, we examine the temperature dependence of the PA signal as tissue samples are heated in a PBS bath.

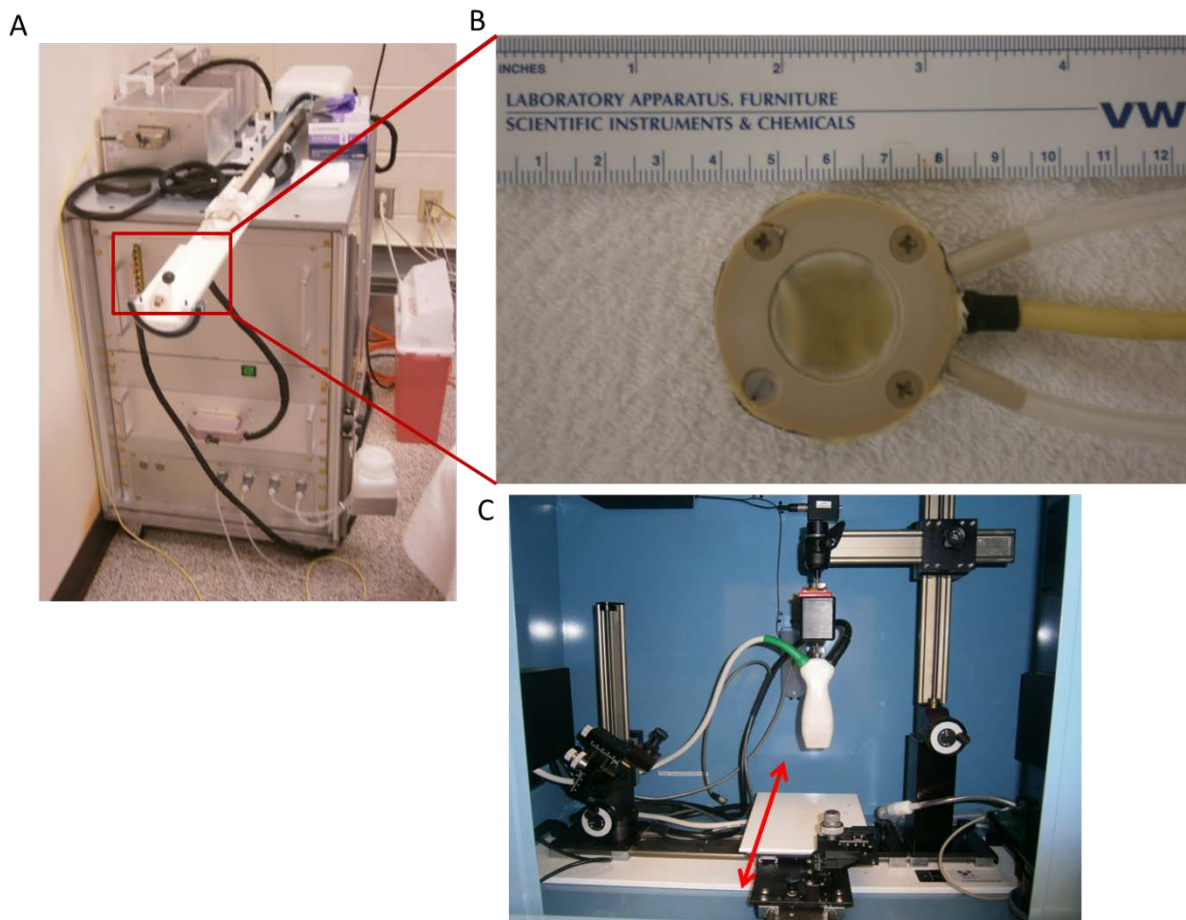


Figure 1. Photographs of experimental equipment. **A)** LabFUS 2.5-MHz small-animal HIFU system. **B)** Close-up view of eight-element, 2.5-MHz HIFU transducer. **C)** Vevo LAZR 2100 combined PAUS imaging system. Red arrow indicates motorized platform for elevation scanning during 3D imaging.

Methods

Sample preparation and ablation procedure

Imaging samples were acquired from fresh porcine cardiac and liver tissues (Animal Technologies Inc., Tyler, TX) within 24 hours of sacrifice and were never frozen. Excised tissues from one liver and two hearts were used to make three liver samples and three cardiac samples, each approximately 30x30x20 mm³ in size. Each specimen was embedded into an agar phantom for HIFU sonication. The HIFU transducer was acoustically coupled to the agar phantoms using ultrasound gel and samples were each sonicated for 120 seconds at power settings between 22 and 30 watts using a LabFUS 2.5-MHz small-animal HIFU system (Image Guided Therapy Inc., Paris, France). Photographs of the HIFU system, HIFU transducer, and imaging system are presented in **Figure 1**. Following ablation, tissue specimens were removed from their agar phantoms, and the uppermost 1.5 – 2 mm of tissue surface was removed in order to expose ablation lesions to allow for tissue-sample photography and later co-registration with imaging data.

Additionally, fresh bovine liver tissues (Animal Technologies Inc., Tyler, TX) were acquired within 24 hours of sacrifice and never frozen. Two samples were excised from one liver and submerged in normal PBS in an imaging chamber containing a heat exchanger. The goal of this experiment was to monitor the tissue PA signal as a function of bath temperature. The tissue sample was located in the center of the copper tubing coil, which comprised the heat exchanger, to generate an approximately isotropic temperature field. Bath temperature was measured via

thermocouple at a location a few millimeters from the upper surface of the tissue imaging plane.

Imaging setup

Following the aforementioned ablation procedure, specimens were anchored in a thin layer of gelatin and submerged in normal phosphate buffered saline (PBS) to achieve acoustic coupling between the tissue sample and the PAUS transducer. PAUS imaging was performed using a Vevo LAZR 2100 imaging system equipped with a 21-MHz US transducer coupled to a pulsed Nd:YAG laser capable of irradiating from 670-970 nm (FUJIFILM VisualSonics Inc., Toronto, Canada). In each sample, a single-wavelength 3D PAUS scan was performed over the extent of the tissue sample in order to identify a single plane containing the ablation lesion. The location of the lesion was chosen by selecting an area in the 3D PAUS scan exhibiting a hyperechoic US signal and high PA contrast. After identification of the lesion, a 2D comprehensive multi-wavelength PA scan was performed on this plane using wavelengths ranging from 680-970 nm in 3-nm steps. A multi-wavelength 3D PAUS scan was then performed on each tissue over a volume including the ablation lesion using five wavelengths in the NIR region (740, 750, 760, 780, 900 nm), corresponding to a distinct feature in the Hb absorption spectrum (199), and averaging eight frames for each wavelength and location.

For the bath-heated samples, multi-wavelength PA imaging was done using five wavelengths in the NIR region (740, 750, 760, 770, 780 nm), corresponding to the same Hb spectral feature. First, a baseline multi-wavelength PA acquisition was

performed. The bath-heat exchanger was then activated, and the tissue bath temperature rapidly rose to approximately 60 °C. PA imaging at all wavelengths was conducted at one-minute intervals for the first 30 minutes, then at five-minute intervals thereafter, up to 60 minutes. Bath temperature was measured at each imaging time-point. Immediately post-imaging, the tissue sample was removed from the water bath and bisected at the imaging plane. Photographs were taken of the sample prior to heating, as well as at the point of bisection post-heating.

Staining procedure

Following imaging, samples were stained using triphenyl tetrazolium chloride (TTC) salts for registration and comparison of gross pathology to PAUS data (Sigma-Aldrich Corp., St Louis, MO). TTC is a redox indicator of metabolic activity: the white stain accumulates in cells and is oxidized to a deep red color by a variety of molecules associated with metabolic activity (200,201). Tissue in the ablation region has undergone necrosis and should become white/gray in color, while metabolically active healthy tissue outside the ablation region will become a deep red. Staining solutions were prepared by dissolving 0.1 mg/ml TTC in normal PBS. Tissue samples were submerged in staining solution and incubated at 37° C for 20 minutes with constant stirring. After staining, tissue samples were patted dry and photographed. Bath-heated tissue samples were not stained as the tissue was clearly coagulated throughout the entire tissue volume.

2D multi-wavelength PA analysis

The comprehensive 2D multi-wavelength scans were analyzed to assess whether HIFU treatment results in a change in the PA spectra of tissue. Regions of interest (ROI) were selected in areas showing high PA contrast and areas showing low PA contrast, corresponding to areas of ablated and non-ablated tissue, respectively. The mean PA signal inside each ROI was calculated for each wavelength scanned and plotted to display the absorption spectra for ablated (liver and cardiac, respectively) and non-ablated tissue (**Figure 2**).

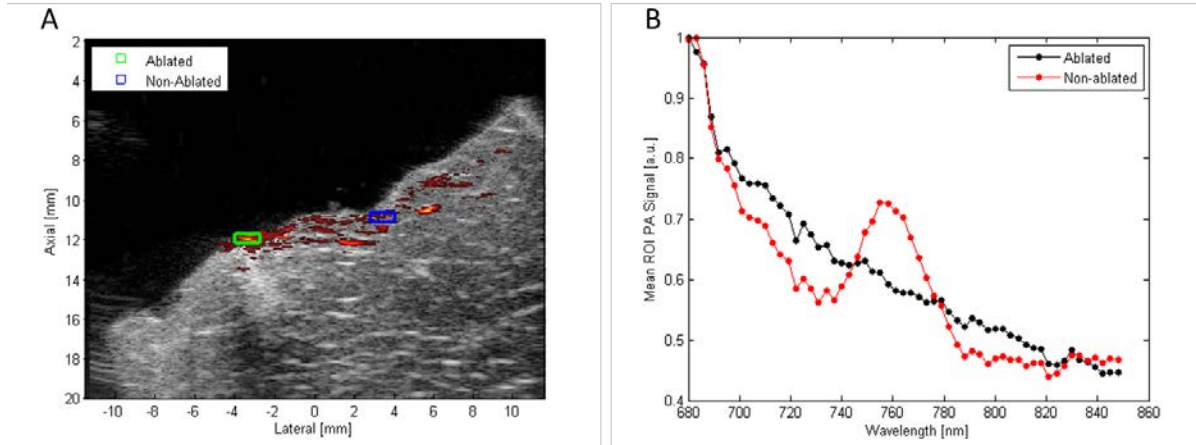


Figure 2 Results of 2D comprehensive multi-wavelength PA imaging. A) Overlay of single-wavelength PA data at 710 nm on matched US image. High PA contrast and US hyperechogenicity exhibited in area where lesion is expected. **B)** Plot of mean PA signal in each ROI indicated at each wavelength. Mean PA spectrum in areas outside lesion exhibit the characteristic peak of Hb around 760 nm; peak not seen in area of high PA contrast where lesion is expected.

Creation of tissue characterization maps

Tissue characterization maps (TCMs) were generated using a correlation-based algorithm. Reference absorption spectra for ablated and Hb absorbers were obtained from the comprehensive multi-wavelength PA data (liver or cardiac, as appropriate) using previously described methods (191). The filtered PA data were

compared to two reference spectra (i.e. Hb correlation and a distinct ablated correlation for each tissue type), resulting in two 3D datasets of Pearson correlation coefficients. These two 3D correlation datasets (i.e. Hb correlation coefficients and ablated correlation coefficients) were then processed with a simple thresholding algorithm. Correlation thresholds of 0.6 were used for both Hb and ablated reference spectra. PA voxels were then classified based on the respective thresholds and correlation coefficients. Voxels that correlated strongly (i.e. displayed correlation coefficients above the threshold) to only one reference spectra were classified accordingly (i.e. class 2 for ablated; class 1 for Hb). Voxels that correlated strongly to both were classified according to their greatest correlation coefficient. Voxels that correlated strongly to neither reference spectra were classified as 0 (no correlation). Thus, a trinary 3D TCM was constructed for each PA dataset and compared to photographed gross pathology. For the bath-treated tissue samples, an equivalent process was employed, save that a correlation threshold of 0.65 was used. A 2D TCM was generated at each time point, and the 2D multi-wavelength PA signal was examined as a function of time (i.e. thermal exposure).

Image registration and characterization of ablation size

HIFU 3D TCM data were co-registered with top-view photographs of stained gross pathology by manual registration based on corresponding visual landmarks. Top-view C-scan TCMs were obtained by taking the mode along the depth axis for each voxel at the surface of the TCM volume. Mode calculations were performed from a depth 0.184 mm (corresponding to five voxels, which tended to avoid

subsurface fluence artifacts) below the surface of the volume to a depth 1.29 mm (corresponding to 35 voxels) below the surface. Borders between areas of ablation and non-ablation were manually segmented in matched TCMs and pathology photographs by three experts, generating three segmentations for each TCM or pathology photograph. The segmentations for each TCM or photograph were analyzed automatically using MATLAB. Pixel-wise lesion area was calculated from each expert-segmentation of corresponding TCM data and gross pathology photographs. The mean and standard deviation of lesion areas from the expert segmentations were calculated and subsequently converted to physical dimensions (mm²). Percent area agreement between gross pathology and TCMs was calculated for each tissue sample as

$$\begin{aligned} & \text{\% Area Agreement} & & \text{Eq.} \\ & = 1 - \frac{|\text{Segmented Image Area} - \text{Segmented Pathology Area}|}{\text{Segmented Pathology Area}} & & 2 \end{aligned}$$

An SNR analysis was done, comparing SNR up to 8 mm tissue depth, while varying the number of averages. A 0.21x0.18 mm² sliding kernel was used, analyzing signal along a depth line located in the center of the ROI shown in **Figure 5A**. Additionally, a noise image was acquired (degassed water, no laser irradiation) to assess PA image noise at the equivalent depth. Up to 64 averages were used. Analysis was done on beam-formed image data, using the following equation

$$\text{SNR} = 10 \cdot \log_{10} \left(\frac{\overline{PA}}{\sigma_{noise}} \right), \quad \text{Eq. 3}$$

where \overline{PA} and σ_{noise} denote the ROI mean PA signal and noise standard deviation, respectively. The SNR threshold was empirically determined by analyzing the depth, and thus corresponding SNR, at which the TCM loses continuity (i.e. the point at which the gaps/inconsistencies in the solid TCM regions become as large as or greater than the spatial averaging kernel used).

Results

2D multi-wavelength PA analysis

Figure 2 displays the results of 2D multi-wavelength PA imaging performed in liver tissue. **Figure 2A** shows an overlay of the single-wavelength PA signal at 710 nm on its matched US image. ROIs shown in **Figure 2A** represent the area averaged at each wavelength to generate the reference spectra from ablated and non-ablated tissue; these spectra are shown in **Figure 2B**. We expect the dominant absorber to be Hb in this wavelength region as the *ex vivo* tissue samples should be oxygen-depleted (178). Non-ablated tissue displays an absorption spectrum that agrees well with that of Hb (191) as the characteristic local maximum in the absorption spectrum around 760 nm is readily apparent. The absorption spectrum in the ROI corresponding to ablated tissue decreases monotonically with increasing optical wavelength and does not display the characteristic 760-nm local maximum of the Hb absorption spectrum, indicating a likely change in the concentration of Hb absorbers due to hyperthermia.

Lesion area statistics

TCMs were created by correlating to wavelengths in the region between 740 and 780 nm; the region where ablated tissue and Hb absorption spectra are most distinct. Tissue characterization was achieved at depths up to 3 mm below the surface of the tissue, while gross pathology indicated that lesions extend 5-7 mm in depth. Examples of 3D TCM volumes overlaid on matching US volumes for liver and cardiac tissues are shown in **Figure 3**.

Results of area calculations performed on manually segmented lesions in both TCMs and gross pathology photographs can be found in **Table 1**; a representative sample image can be found in **Figure 4**. In TCM volumes, we observed areas of tissue bordering the areas of strong ablation correlation that correlated poorly to both ablated and non-ablated absorption spectra. These areas were segmented in addition to the area that was primarily classified as the lesion and was also compared to gross pathology.

	Liver #1	Liver #2	Liver #3	Cardiac #1	Cardiac #2	Cardiac #3
Pathology Area (mm ²)	16.9±1.8	35.3±3.7	22.2±2.0	11.4±1.0	10.3±0.1	3.5±0.2
Combined Ablated Core and Non-Correlation Region area (mm ²)	15.7±1.9	28.1±0.2	22.2±0.1	11.5±0.4	7.21±0.2	3.2±0.1
% Area Agreement Combined Ablated Core and Non-Correlation Region	93.2%	79.8%	99.9%	99.1%	70.0%	91.7%
Ablated Core Area	8.53±0.1	25.6±0.1	20.0±0.1	11.6±0.6	7.2±0.2	2.1±0.2
% Area Agreement Ablated Core	50.6%	72.5%	90.2%	98.3%	70.1%	61.2%

Table 1 Results of area calculations performed on manually segmented lesions in both TCMs and gross pathology photographs.

For the bath-heated samples, **Figure 5A–E** shows a 2D TCM overlaid on co-registered B-Mode US images for five time points, with a rectangular square identifying an ROI for spectral analysis. At baseline (**Fig. 5A**) strong correlation to Hb is observed to approximately 4 mm in depth across the entire width of the tissue sample. The depth of this correlation decreases to about 2 mm by 15 minutes (**Fig. 5B**). By 30 minutes, a thin layer correlating to ablated tissue can be identified at the tissue surface (**Fig. 5C**). At 45 minutes, 1 – 2 mm of ablated tissue is identified at the surface, with only sporadic Hb is identified beneath the surface, and this trend

continues at 60 minutes (**Fig. 5E**). **Figure 5F** shows a surface plot of the mean PA signal of the ROI, normalized to baseline, as a function of wavelength and time. The PA signal rapidly increases for the first 5 minutes after heating onset, but still maintains the Hb spectral shape (local maximum at 760 nm). Amplitude decreases slightly, but spectral shape is maintained until approximately 30 minutes, at which point the spectra begins to flatten, correlating more strongly to the ablated reference spectra thereafter (as shown by the surface color). **Figure 5G** allows for better comparison of the spectra at prominent time points. Note that at 5 minutes after heating onset (bath temperature of 52 °C) a PA signal increase of approximately 80% from baseline can be seen across all wavelengths. The signal decreases slightly, but remains relatively constant at roughly 50% above baseline until about 30 minutes after heating onset. At 30 minutes, we can see the PA spectrum flattening out, and by 45 and 60 minutes, we observe a monotonically decreasing spectrum that strongly resembles the ablated reference spectrum for liver.

Analysis of TCMs against the SNR results suggests that an SNR of 10 dB is generally sufficient for reliable tissue characterization using this method. By increasing averages, we found SNR using this method can be improved approximately proportional to $\sqrt{\# \text{ averages}}$, allowing accurate TCMs at greater depths in tissue, though at the cost of increased imaging time.

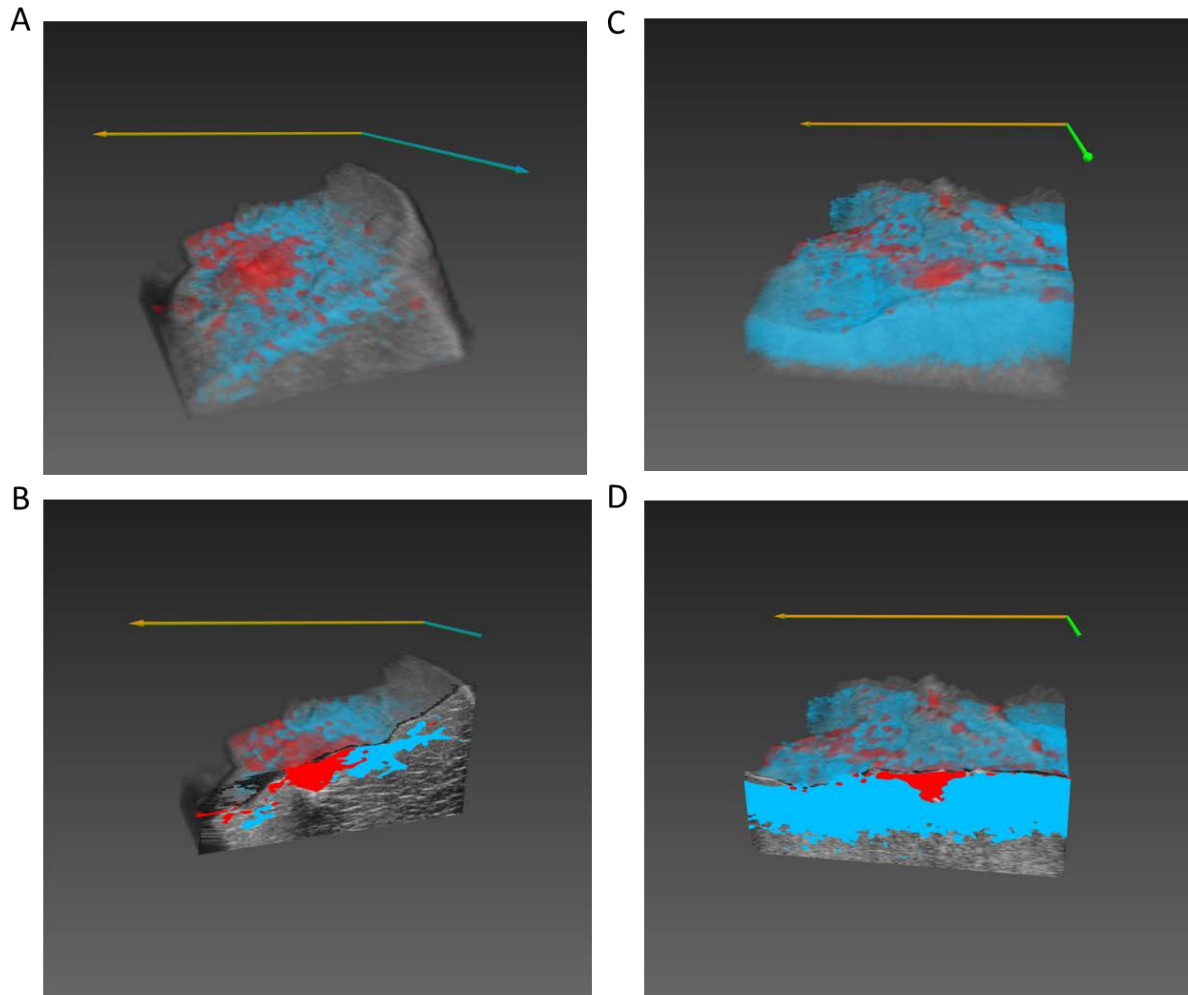
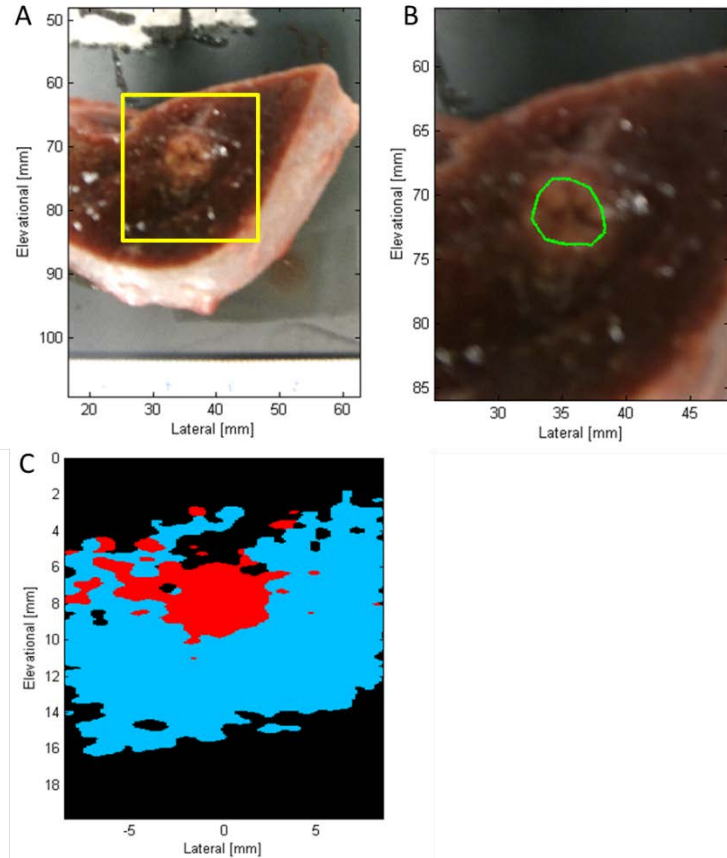


Figure 3 Renderings of 3D TCM volumes overlaid matching 3D US volumes. **A)** Full liver sample 3D volume rendering and **B)** cut-away view of 2D frame in the interior of the lesion of the same liver volume. **C)** Full cardiac sample 3D volume rendering and **D)** cut-away view of 2D frame in the interior of the lesion of same cardiac volume.

Discussion

In this initial study, we demonstrate that multi-wavelength PA imaging can provide estimates of lesion extent with gross pathology area agreement greater than 79% in liver and greater than 70% in cardiac tissue. As has been shown previously (193,197,202) and demonstrated in this study (**Figure 2**), high PA signal contrast in

the ablated lesion center can be obtained using a single laser wavelength. However, PA imaging data from a single wavelength tends not to be sufficient to completely characterize the extent of the ablation lesion. While single-wavelength PA imaging may be useful to perform a quick 3D scan and obtain a rough identification of the lesion center, multi-wavelength TCMs provide significantly more information about the boundaries and extent of ablation lesions, as shown



by comparing figures 2A and 3B and 5A–E. Focusing on the wavelengths where the

Figure 4 Comparison of gross pathology and TCM data for one liver tissue sample. **A)** Photographed stained gross pathology. Red box indicates area of tissue displayed by 2D TCM data. **B)** Zoomed in photograph of stained gross pathology. Manual segmentation of gross pathology overlaid in green. **C)** C-scan 2D TCM plane reconstructed from TCM volume for manual segmentation. Blue indicates Hb correlation, Red indicates ablated spectrum correlation, black indicates correlation to neither spectra.

absorption spectra of ablated and non-ablated tissue display different features, multi-wavelength TCMs were able to identify HIFU ablation lesions in *ex vivo* cardiac and liver tissue and obtain area agreement with gross pathology photographs in excess of 70% and with sub-millimeter spatial resolution. TCMs compared well with manually segmented gross pathology photographs (minimum 70% area agreement),

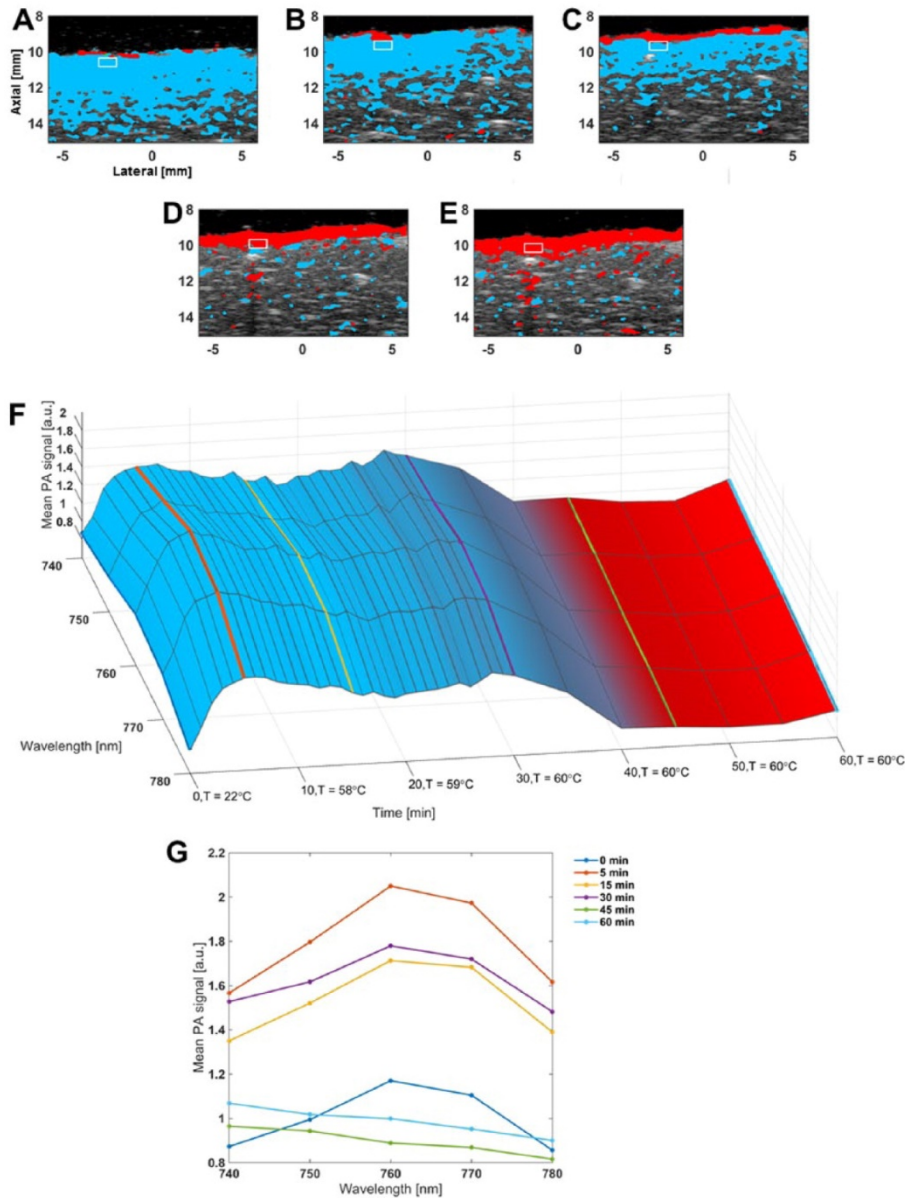


Figure 5. Comparison of TCMs (same color-coding as previously stated) and spectra for sample subjected to PBS-bath thermal treatment: **(A)** to **(E)** TCMs overlaid on co-registered US B-mode image for time-points 0 (baseline), 15, 30, 45, and 60 minutes of thermal treatment, respectively. White rectangular box denotes a 1 × 0.5 mm² ROI selected for analysis, maintained at constant depth from tissue surface; **(F)** surface plot of mean PA signal in ROI (normalized to baseline), as a function of wavelength and time. Surface color-map represents mean TCM color value across ROI at each time-point; **(G)** PA-signal spectra from F for time-points 0, 5, 15, 30, 45, and 60 minutes (time-points at 0, 15, 30, 45, and 60 minutes correspond to images A to E, respectively). TCM = tissue characterization map; PBS = phosphate buffered saline; US = ultrasound; PA = photoacoustic; ROI = regions of interest.

demonstrating multi-wavelength PA imaging as a potential tool for HIFU lesion identification and quantification.

Despite our success in the identification and characterization of HIFU ablation lesions in cardiac and liver tissues, limitations in PA

imaging and our experimental setup prevent ideal characterization of

lesion dimensions. Imaging artifacts immediately at the surface of the tissue were observed and are believed to be the result of subsurface photon fluence and

refractive index discontinuities between the surface of the tissue and the PBS used to couple the tissue to the ultrasound transducer. In our study, these artifacts were mitigated when creating 2D TCM images of the top-view plane by using a depth 0.184 mm below the tissue surface as the starting point for reconstruction of the C-scan projected views.

PA based TCMs also underestimated lesion depth in this experiment. Depth of PA imaging is limited by scattering of photons which increases the likelihood of absorption by chromophores at shallower depths in the tissue. In this experiment, imaging depths were limited to no more than 3 mm below the surface of the tissue, yet HIFU lesions extended 5-7 mm in depth. Several techniques could be employed in order to increase the penetration depth of imaging, including increased photon fluence and increased frame averaging to improve the signal-to-noise ratio at depth, as discussed below. Interstitial delivery of light by laser fibers also allows for significantly deeper light delivery to provide image guidance of treatments on deep-lying tissues, such as the liver and kidneys (203). By employing these methods, it should be possible to extend imaging depth beyond 3 mm in *ex vivo* experiments. Additionally, penetration depth could possibly be improved in *in vivo* experiments due to the fact that tissues will be highly oxygenated. Optical absorption by oxygenated hemoglobin is roughly an order of magnitude lower in the NIR spectrum than that of Hb (179). This reduction in optical absorption may allow increased optical penetration depth while maintaining energy, but it may require re-optimizing imaging wavelengths to maintain contrast between ablated and native oxygenated tissue.

A noteworthy effect observed in this experiment was the appearance of a ring of tissue surrounding the area correlating to ablated tissue in TCMs that did not correlate well to either the obtained ablated tissue spectrum or the standard Hb spectrum. This effect was observed in both liver and cardiac tissue in our study and has been reported in previous studies (191). In cardiac tissues, the area of non-correlation was not always observed. An example of this effect is seen in **Figure 4C**, where an area of non-correlated tissue (i.e. black) borders the upper area correlating highly to ablated tissue (i.e. red) at the core of the lesion. The segmentation region containing the region of ablation-correlated (red) and non-correlated (e.g. also including the black region extending from 4-6 mm in elevation in **Fig. 4C**) tissue showed better agreement with segmented ablation regions in gross pathology photographs than the segmentations of the ablation-correlated region alone. Regions of ablation correlation alone tended to underestimate the area extent of lesions when compared to gross pathology segmentations. The change in the PA spectrum in ablated tissue likely results from hyperthermia-induced changes in the Hb chromophore. It is possible that incomplete conversion of Hb occurs at the edge of the ablation region due to reduced increase in local temperature as compared to the core of the lesion, resulting in an absorption spectrum that did not correlate well to either Hb or the lesion core.

The capacity of PA imaging to assess temperature has been previously demonstrated by examining changes in PA amplitude (180,183) . By applying similar techniques, we were able to track the relative temperature rise in the bath-heated tissue sample during the first several minutes. As shown in **Figure 5F**, the PA

amplitude then decreases slightly after five minutes. We suspect this is primarily a result of changes in surface fluence. As can be seen in the B-Mode US images in **Figure 5**, the tissue swells initially (**B** and **C**), before contracting partially (**D** and **E**). This initial tissue swelling is likely the result of increased osmotic pressure in the bath, following temperature increase. The swelling is likely to affect and the surface fluence, due to a change in separation between the tissue and light emission source. The tissue contraction observed in **Figure 5D** and **5E** is likely due coagulation of ECM proteins, which concurs with the observed strong correlation of the PA signal to the ablated reference spectrum (red region in figures). These results highlight the potential complementary nature of PA thermography and multi-wavelength analysis. Tissue coagulation may also explain the decrease in PA amplitude after 30 minutes, as increased optical scattering following coagulation will reduce fluence, and thus PA signal, at greater depths. While these factors confound PA thermography in this experiment, these issues may not be as prevalent in clinical applications for several reasons. First, tissue hyperthermal therapy typically occurs on the order of several seconds to a few minutes and is typically much more spatially localized, which may reduce large scale tissue swelling or edema. Lastly, if an optical scattering increase within an ROI correlates to a change in the observed PA spectra, as suggested by this study, it may serve as a partial endpoint for hyperthermal therapy, rather than a mitigating factor to image guidance. Furthermore, if changes in optical fluence and absorption can be accounted for (perhaps by collecting some backscattered light for diffuse reflectance assessment (204)), PA thermography may be able to quantify thermal dose, comparable to what is currently done using MRI thermography.

The SNR analysis suggests that roughly 10 dB SNR is necessary for reliable TCM analysis. Our particular system showed that, with 64 averages, the SNR up to 5 mm can be improved to allow for reliable TCM analysis. While increased averaging may be prohibitive in some clinical applications, such as cardiac imaging, this analysis suggests a baseline to predict TCM accuracy as a function of depth for a given application and imaging system.

Future work

Development of *in vivo* imaging solutions will be necessary to apply PA imaging clinically for guidance of HIFU treatments. Although development of an *in vivo* system for combined HIFU therapy and PAUS imaging will not be a trivial task, building upon previous work by Cui *et al.* (193,195,202) and Prost *et al.* (205) may improve single-device integration, which allows straightforward co-registration of HIFU ablation space with PA and US imaging spaces. This would overcome a significant hurdle for clinical translation.

Real-time image guidance remains a currently unrealized goal for developing PA imaging systems. While this study used a laser source with a pulse repetition frequency (20 Hz) that limited acquisition to near-real-time imaging (five single-wavelength frames per second, without averaging), commercial laser systems operating at kilohertz pulse repetition frequencies are readily available at select wavelengths, albeit sometimes with lower pulse energies. These systems may allow PA imaging, with proper wavelength selection, to achieve complete real-time image guidance exceeding 30 frames per second (191).

Corroboration of these results in an *in vivo* model is necessary in order to confirm that the findings reported here are relevant to further clinical application. One recent study (192) has reported inconclusive findings, showing that while most single-wavelength *ex vivo* studies reported positive PA contrast in the ablation lesion, it is possible to observe negative contrast in ablation lesions *in vivo*. One proposed explanation is that variations in thermal deposition between *in vivo* and *ex vivo* models may lead to a different distribution of chromophores between the two environments. As our method relies upon correlation to multiple laser wavelengths, it may be possible to identify a difference in the chromophores present in the ablated regions of *in vivo* and *ex vivo* models. While the data in this study suggests Hb is present in significant quantities before ablation and is significantly reduced following ablation, it is not clear which chromophore(s) is generating PA signal in the ablated region. Previous work has suggested that increased temperatures during thermal therapy may give rise to a variety of hemoglobin derivatives, which may account for the observed contrast between normal and ablated tissue (206–208). While production of hemoglobin derivatives is often cited as a potential source of contrast in ablated tissues, to our knowledge no study has shown definitively that the proposed derivatives are produced in significant concentrations in tissue. Studies of the thermal unfolding and aggregation process of hemoglobin using 2D infrared spectroscopy have shown that thermal degradation is a complex, multi-step process that is irreversible once local tissues reach a certain temperature threshold: initial destabilizations in the structure of hemoglobin occur at low temperatures between 30-44° C; complete thermal unfolding occurs between 44-54° C; and irreversible

aggregation of the denatured protein occurs at temperatures above 54° C (209). This complex, three-stage denaturation process involves several potentially irreversible conformation changes in the structure of hemoglobin. Given the dependence of protein absorption on the 3D structure of the protein, these irreversible, temperature-dependent structural changes in hemoglobin may explain the observed elimination of the 760-nm peak in the Hb spectrum in ablated tissue. Partial unfolding of Hb may yield a range of different absorption spectra in ablated tissues rather than a single absorption spectrum corresponding to a single chromophore. This range of unfolding states could explain the observed correlation discrepancies at the edges of tissue lesions and could be developed to benchmark levels of partial tissue coagulation. In future studies, it would be useful to submit samples of ablated and non-ablated tissues to hemopathological and chemical assays in order to identify with confidence which chromophores are present and in what concentration before and after ablation.

PA-based temperature monitoring must also account for changes in optical absorption and fluence. A previous study (210) monitored the PA signal ratio at two different wavelengths during tissue heating, verifying that PA signal variations occur consistently across wavelengths until the tissue undergoes a change of state (i.e. thermal coagulation), as we observed. By analyzing complementary PA-signal amplitude and multi-wavelength techniques used herein with more applicable hyperthermia models (RF- and HIFU-hyperthermal therapy using *in vivo* models), we can better evaluate and improve their utility, which is paramount to implementing real-time imaging guidance for thermal treatment.

Conclusion

We have demonstrated the feasibility of using multi-wavelength PA imaging to create tissue characterization volumes that allow the differentiation of HIFU-induced tissue ablation lesions from non-ablated tissue and to estimate the treatment margins of tissue ablations in 2D planes in *ex vivo* cardiac and liver tissue samples following a HIFU ablation. Multi-wavelength PA imaging demonstrates that HIFU-induced hyperthermia results in changes in the Hb absorption spectrum that can be leveraged for PA-based segmentation. Multi-wavelength TCMs were used to successfully identify lesion size with a greater accuracy than single-wavelength methods. Multi-wavelength TCMs agreed with gold-standard stained pathology images (70% area agreement) and were able to successfully assess lesion margins with a spatial resolution comparable to existing temperature MRI techniques. Additionally, we demonstrated the complementary nature of PA thermography and multi-wavelength TCMs. Further *in vivo* experiments concurrent with treatment must be performed to assess PA signal changes in living tissues. These results suggest that multi-wavelength PA imaging and PA thermography present a promising modality for guiding hyperthermia therapies that depend on precise knowledge of temperature and lesion extent in order to preserve critical structures.

Acknowledgements

The authors would like to thank Dr. Jason Stafford, Oguzhan Ege, Charles Kingsley, Trevor Mitcham, and Houra Marta Taghavi for assisting with experiments.

We would also like to thank Jordan Roos for administrative assistance. This work was funded, in part, by a Cancer Prevention and Research Institute of Texas Julia Jones Mathews Scholarship.

CHAPTER FIVE

CONCLUSION

In this dissertation we have discussed the issue of disease-generating intracellular protein-protein interactions (PPIs) and the challenges they pose for researchers. Traditional small molecule drug design has narrowly focused on a particular area of chemical space to produce “druglike” molecules that passively diffuse through the cell membrane to inhibit proteins by occupying localized hydrophobic binding pockets on the surfaces of proteins, primarily the active sites of enzymes. These targets represent only a small portion of disease-generating targets however, and drug-like small molecules lack the size to interrupt PPIs when those interactions occur through the interface of surfaces that measure hundreds or even thousands of square Angstroms. Biologics have addressed this problem, at least in part, by virtue of the fact that monoclonal antibodies—which typically mass ~150 kDa)—have the requisite size to bind to massive protein surface areas and in fact are often larger than their targets. Production of monoclonal antibodies is often prohibitively expensive however, and the main asset of antibodies—their size—is an Achilles heel as it prevents them from accessing intracellular compartments.

Peptides occupy a potentially useful region of chemical space between small molecules and biologics. At a length of ~5-20 amino acids, therapeutically-relevant peptides have masses in the range 500-2500 Da and surface areas $>400 \text{ \AA}^2$. Molecules in this range have sufficient size to disrupt many PPIs, yet peptides have historically been largely ignored as therapeutic candidates due to issues of stability and cell permeability of linear peptides. In recent decades, technological

developments have made great strides in resolving these issues. Lessons learned from cell-penetrating peptides and naturally cell permeable cyclic peptides like Cyclosporine A have made it clear that elimination of hydrogen bond donors in the peptide backbone and stabilization of the peptide structure through cyclization are key properties inherent to stable, cell-permeable peptides. Backbone stabilization—through macrocyclization or stapling—and incorporation of N-methylation of backbone amides are now common design choices that produce serum stable peptides often capable of accessing the cytosol. Directed evolution technologies like mRNA display are able to efficiently screen massive libraries of peptides—far larger by orders of magnitude than any small molecule screen—to produce molecules that bind targets and disrupt PPIs with affinity and selectivity comparable to antibodies. Technological advancements in mRNA display technology, notably SUPR peptide mRNA display, incorporate N-methylation, macrocyclization, and protease screens produce serum stable peptides that retain superior binding properties. Excitingly, many of the features that impart protease resistance are now known to facilitate cell permeability, opening the door to the deployment of SUPR peptide mRNA display as a design tool to develop new compounds that target intracellular PPIs.

In this dissertation, we have described SUPR mRNA display selections against LC3, a small ubiquitin-like protein that plays a crucial role in autophagy. The lead candidate from these selections, SUPR4B1W, bound to LC3 with a mid-nanomolar affinity and showed specificity for the LC3A and LC3B isoforms of LC3. SUPR4B1W disrupts interactions between LC3 and the autophagy related protein Atg4b *in vitro* and has a biological half-life of approximately 2 hours in the presence

of the highly active protease, Proteinase K. Evidence of autophagy inhibition was observed in two different models of ovarian cancer treated with SUPR4B1W.

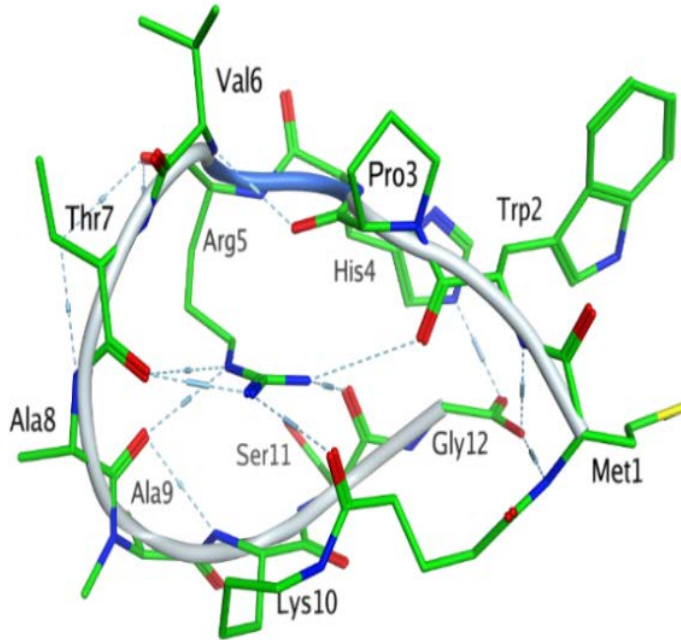


Figure1. 3D structure of SUPR4B1W. One of the conformational ensemble structures reveals that Arg5 side chain forms multiple internal hydrogen bonds with several other residues including the backbone carbonyl oxygens of Ala8, Lys10 and Gly12. This may partially explain the enhanced stability of cell permeability of SUPR4B1W.

SUPR4B1W rescued viability in the DIRAS3 model after 72 hours of treatment while chloroquine—a non-specific anti-autophagy compound that disables lysosomal degradation—does not. These data, along with evidence that

SUPR4B1W inhibits Atg4B activity *in vitro*, suggest that SUPR4B1W may inhibit the early autophagy machinery and frustrate autophagosome formation. In models of autophagy-induced cisplatin resistance, treatment with SUPR4B1W re-sensitized ovarian cancer cells to cisplatin causing a significant reduction in cellular viability compared to treatment with cisplatin alone. Treatment with SUPR4B1W, in combination with cisplatin, also effectively prevented outgrowth of tumor nodules in

nude mice four weeks after intraperitoneal injection with an ovarian carcinoma cell line.

Until now, development of autophagy inhibitors has relied on the directed evolution of naïve libraries. Future work on SUPR peptides targeting LC3 will focus on rational design and optimization using predictive modeling of the structure of SUPR4B1W to determine the mechanism of its interactions with LC3.

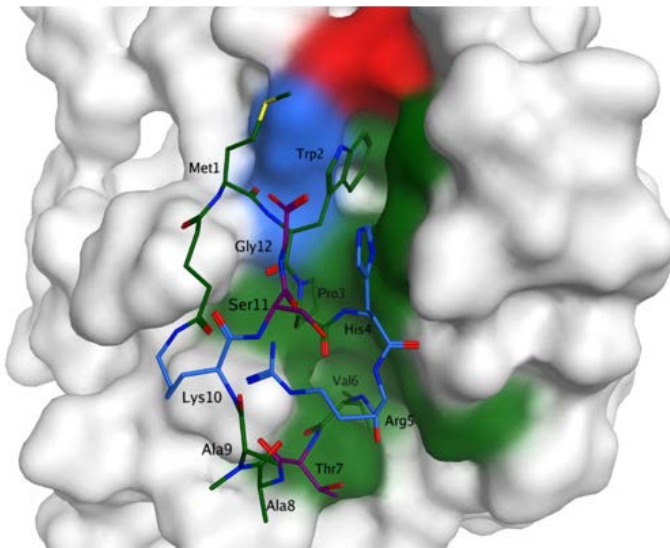


Figure 2: Preliminary computational models of SUPR4B1W docked into the active sites of LC3. Green surface represents hydrophobic areas on LC3, blue for electrostatic positive and red for negative.

Our collaborators the laboratory of Shuxing Zhang have generated structural models of potential conformers of SUPR4B1W. Using this method, the Zhang lab demonstrated that the side-chain of Arg5 in SUPR4B1W forms multiple internal hydrogen bonds with several other amino acids in the peptide (**Figure 1**). These internal

hydrogen bonds may contribute strongly to both the stability and cell permeability of SUPR4B1W.

To model SUPR peptide – LC3 interactions, the LC3A crystal structure (PDB:5CX3) was imported into MOE software. Preliminary modeling based on the initial preposition of SUPR4B1W in the binding pocket of LC3, indicates that the

Pro3 facilitates formation of beta turn involving residues His4, Arg5, and Val6

(Figure 2). Such beta turn structure explains how SUPR4B1W can accommodate an extra residue between the W-site and L-site binding residues as well as enhanced affinity relative to peptides lacking proline at the third position. Moreover, this model supports our hypothesis that the Trp2 side chain interacts with W site and the side

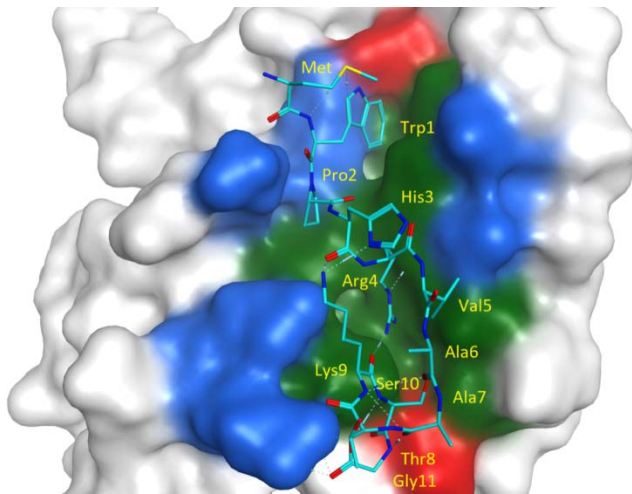


Figure 3 preliminary modeling of SUPR4B1W linear predicts that without the beta turn imposed by proline in the cyclic conformation, it is difficult for Val6 to associate with the L-site resulting in reduced affinity

chain of Val6 interacts with L site. Interestingly, the imidazole side chain of His4 stacks with the side chain of His27 in LC3, potentially contributing to the binding energy of the cyclic peptide. Modeling of the linearized version of

SUPR4B1W provides some insight into why cyclization improves binding **(Figure 3).**

Without the beta turn imposed by cyclization and Pro3, the linear peptide struggles to accommodate the addition of a third spacer amino acid to the LIM and presents Arg4 in the L-site rather than Val5. These observations provide structural evidence to explain the higher affinity of cyclized SUPR4B1W relative to the linear version.

Modeling of the selected SUPR4B peptide (phenylalanine at position 2) predicts a significantly weaker binding energy which we observe experimentally.

In the future, we will carry out computational alanine scans to gain knowledge about the impact of specific residues on the conformation of SUPR4B1W and its interaction with LC3. By computationally mutating individual residues of SUPR4B1W to alanine and docking the new structure into LC3, we can better understand the impact of specific amino acid residues. This data will inform future medicinal chemistry efforts to drive the affinity of SUPR4B1W into the low nanomolar regime. Preliminary computational alanine scanning indicates that mutation of Trp2 or Val6 significantly reduces the affinity to LC3, a prediction that is entirely consistent with our experimental data. Mutating Trp2 to Ala results in maximum affinity reduction while mutating Val6 to Ala results in second highest reduction in affinity. Interestingly, mutating Arg5 to Ala resulted in increase in affinity. The models show that Arg5 does not interact with LC3 receptor and is instead involved in forming multiple hydrogen bond interactions with backbone carbonyl oxygen atoms. We speculate that replacing such Arg with Ala may contribute to increased affinity for LC3 while decreasing its cell permeability through the disruption of the intramolecular hydrogen bond network. Further modeling can help identify amino acid substitutions that may convey improved properties such as binding affinity or specificity for individual isoforms of LC3.

REFERENCES

1. Lipinski CA. Lead- and drug-like compounds: The rule-of-five revolution. *Drug Discovery Today: Technologies*. 2004.
2. Hopkins AL, Groom CR. The druggable genome. *Nat Rev Drug Discov*. 2002;
3. Santos R, Ursu O, Gaulton A, Bento AP, Donadi RS, Bologa CG, et al. A comprehensive map of molecular drug targets. *Nat Rev Drug Discov*. 2016;
4. Betzi S, Restouin A, Opi S, Arold ST, Parrot I, Guerlesquin F, et al. Protein-protein interaction inhibition (2P2I) combining high throughput and virtual screening: Application to the HIV-1 Nef protein. *Proc Natl Acad Sci U S A*. 2007;
5. Johansson-Åkhe I, Mirabello C, Wallner B. Predicting protein-peptide interaction sites using distant protein complexes as structural templates. *Sci Rep*. 2019;
6. Roberts RW, Szostak JW. RNA-peptide fusions for the in vitro selection of peptides and proteins. *Proc Natl Acad Sci U S A*. 1997;94(23):12297–302.
7. Li P, Roller P. Cyclization Strategies in Peptide Derived Drug Design. *Curr Top Med Chem*. 2005;
8. Millward SW, Fiacco S, Austin RJ, Roberts RW. Design of Cyclic Peptides That Bind Protein Surfaces with Antibody-Like Affinity. *ACS Chem Biol*. 2007;2(9):625–34.
9. Roxin Á, Zheng G. Flexible or fixed: A comparative review of linear and cyclic

- cancer-targeting peptides. *Future Medicinal Chemistry*. 2012.
10. Gentilucci L, De Marco R, Cerisoli L. Chemical Modifications Designed to Improve Peptide Stability: Incorporation of Non-Natural Amino Acids, Pseudo-Peptide Bonds, and Cyclization. *Curr Pharm Des*. 2010;
 11. Fiacco S V., Kelderhouse LE, Hardy A, Peleg Y, Hu B, Ornelas A, et al. Directed Evolution of Scanning Unnatural-Protease-Resistant (SUPR) Peptides for in Vivo Applications. *ChemBioChem*. 2016;1643–51.
 12. Chatterjee J, Gilon C, Hoffman A, Kessler H. N-methylation of peptides: A new perspective in medicinal chemistry. *Acc Chem Res*. 2008;
 13. Fiacco S V., Roberts RW. N-methyl scanning mutagenesis generates protease-resistant G protein ligands with improved affinity and selectivity. *ChemBioChem*. 2008;
 14. Harayama T, Riezman H. Understanding the diversity of membrane lipid composition. *Nature Reviews Molecular Cell Biology*. 2018.
 15. Dougherty PG, Sahni A, Pei D. Understanding Cell Penetration of Cyclic Peptides. *Chemical Reviews*. 2019.
 16. Hediger MA, Clémenton B, Burrier RE, Bruford EA. The ABCs of membrane transporters in health and disease (SLC series): Introduction. *Molecular Aspects of Medicine*. 2013.
 17. Smith DE, Clémenton B, Hediger MA. Proton-coupled oligopeptide transporter family SLC15: Physiological, pharmacological and pathological implications.

Molecular Aspects of Medicine. 2013.

18. Rudd MD, Luse DS. Amanitin greatly reduces the rate of transcription by RNA polymerase II ternary complexes but fails to inhibit some transcript cleavage modes. *J Biol Chem.* 1996;
19. Kobayashi J, Suzuki H, Shimbo K, Takeya K, Morita H. Celogentins A-C, new antimitotic bicyclic peptides from the seeds of *Celosia argentea*. *J Org Chem.* 2001;
20. Dickson CJ, Hornak V, Pearlstein RA, Duca JS. Structure-kinetic relationships of passive membrane permeation from multiscale modeling. *J Am Chem Soc.* 2017;
21. Ahlbach CL, Lexa KW, Bockus AT, Chen V, Crews P, Jacobson MP, et al. Beyond cyclosporine A: Conformation-dependent passive membrane permeabilities of cyclic peptide natural products. *Future Med Chem.* 2015;
22. Sheu SY, Yang DY, Selzle HL, Schlag EW. Energetics of hydrogen bonds in peptides. *Proc Natl Acad Sci U S A.* 2003;
23. Deechongkit S, Nguyen H, Powers ET, Dawson PE, Gruebele M, Kelly JW. Context-dependent contributions of backbone hydrogen bonding to β -sheet folding energetics. *Nature.* 2004;
24. Bockus AT, McEwen CM, Lokey RS. Form and Function in Cyclic Peptide Natural Products: A Pharmacokinetic Perspective. *Curr Top Med Chem.* 2013;
25. Bionda N, Stawikowski M, Stawikowska R, Cudic M, López-Vallejo F, Treitl D,

- et al. Effects of Cyclic Lipodepsipeptide Structural Modulation on Stability, Antibacterial Activity, and Human Cell Toxicity. *ChemMedChem*. 2012;
26. Bertino EM, Otterson GA. Romidepsin: A novel histone deacetylase inhibitor for cancer. *Expert Opinion on Investigational Drugs*. 2011.
 27. Smolewski P, Robak T. The discovery and development of romidepsin for the treatment of T-cell lymphoma. *Expert Opin Drug Discov*. 2017;
 28. Schreiber SL, Crabtree GR. The mechanism of action of cyclosporin A and FK506. *Immunology Today*. 1992.
 29. Witek J, Keller BG, Blatter M, Meissner A, Wagner T, Riniker S. Kinetic Models of Cyclosporin A in Polar and Apolar Environments Reveal Multiple Congruent Conformational States. *J Chem Inf Model*. 2016;
 30. Masuda Y, Tanaka R, Ganesan A, Doi T. Systematic Analysis of the Relationship among 3D Structure, Bioactivity, and Membrane Permeability of PF1171F, a Cyclic Hexapeptide with Paralyzing Effects on Silkworms. *J Org Chem*. 2017;
 31. Doherty GJ, McMahon HT. Mechanisms of Endocytosis. *Annu Rev Biochem*. 2009;
 32. Kaksonen M, Roux A. Mechanisms of clathrin-mediated endocytosis. *Nature Reviews Molecular Cell Biology*. 2018.
 33. Swanson JA, King JS. The breadth of macropinocytosis research. *Philosophical Transactions of the Royal Society B: Biological Sciences*. 2019.

34. Lim JP, Gleeson PA. Macropinocytosis: An endocytic pathway for internalising large gulps. *Immunology and Cell Biology*. 2011.
35. West MA, Bretscher MS, Watts C. Distinct endocytotic pathways in epidermal growth factor-stimulated human carcinoma A431 cells. *J Cell Biol*. 1989;
36. Recouvreux MV, Commisso C. Macropinocytosis: A metabolic adaptation to nutrient stress in cancer. *Frontiers in Endocrinology*. 2017.
37. Jones AT. Macropinocytosis: Searching for an endocytic identity and role in the uptake of cell penetrating peptides. *Journal of Cellular and Molecular Medicine*. 2007.
38. Mann DA, Frankel AD. Endocytosis and targeting of exogenous HIV-1 Tat protein. *EMBO J*. 1991;
39. Derossi D, Joliot AH, Chassaing G, Prochiantz A. The third helix of the Antennapedia homeodomain translocates through biological membranes. *J Biol Chem*. 1994;
40. Agrawal P, Bhalla S, Usmani SS, Singh S, Chaudhary K, Raghava GPS, et al. CPPsite 2.0: A repository of experimentally validated cell-penetrating peptides. *Nucleic Acids Res*. 2016;
41. Zorko M, Langel Ü. Cell-penetrating peptides: Mechanism and kinetics of cargo delivery. *Advanced Drug Delivery Reviews*. 2005.
42. Su Y, Doherty T, Waring AJ, Ruchala P, Hong M. Roles of arginine and lysine residues in the translocation of a cell-penetrating peptide from ¹³C, ³¹P,

and ¹⁹F Solid-State NMR. *Biochemistry*. 2009;

43. Christianson HC, Belting M. Heparan sulfate proteoglycan as a cell-surface endocytosis receptor. *Matrix Biol*. 2014;
44. Wallbrecher R, Verdurmen WPR, Schmidt S, Bovee-Geurts PH, Broecker F, Reinhardt A, et al. The stoichiometry of peptide-heparan sulfate binding as a determinant of uptake efficiency of cell-penetrating peptides. *Cell Mol Life Sci*. 2014;
45. Dom G, Shaw-Jackson C, Matis C, Bouffieux O, Picard JJ, Prochiantz A, et al. Cellular uptake of Antennapedia Penetratin peptides is a two-step process in which phase transfer precedes a tryptophan-dependent translocation. *Nucleic Acids Research*. 2003.
46. Witte K, Olausson BES, Walrant A, Alves ID, Vogel A. Structure and dynamics of the two amphipathic arginine-rich peptides RW9 and RL9 in a lipid environment investigated by solid-state NMR and MD simulations. *Biochim Biophys Acta - Biomembr*. 2013;
47. Magzoub M, Pramanik A, Gräslund A. Modeling the endosomal escape of cell-penetrating peptides: Transmembrane pH gradient driven translocation across phospholipid bilayers. *Biochemistry*. 2005;
48. Erazo-Oliveras A, Muthukrishnan N, Baker R, Wang TY, Pellois JP. Improving the endosomal escape of cell-penetrating peptides and their cargos: Strategies and challenges. *Pharmaceuticals*. 2012.

49. Lönn P, Dowdy SF. Cationic PTD/CPP-mediated macromolecular delivery: Charging into the cell. *Expert Opinion on Drug Delivery*. 2015.
50. Bus T, Traeger A, Schubert US. The great escape: How cationic polyplexes overcome the endosomal barrier. *Journal of Materials Chemistry B*. 2018.
51. Verdurmen WPR, Mazlami M, Plückthun A. A quantitative comparison of cytosolic delivery via different protein uptake systems. *Sci Rep*. 2017;
52. Lättig-Tünnemann G, Prinz M, Hoffmann D, Behlke J, Palm-Apergi C, Morano I, et al. Backbone rigidity and static presentation of guanidinium groups increases cellular uptake of arginine-rich cell-penetrating peptides. *Nat Commun*. 2011;
53. Mandal D, Nasrolahi Shirazi A, Parang K. Cell-penetrating homochiral cyclic peptides as nuclear-targeting molecular transporters. *Angew Chemie - Int Ed*. 2011;
54. Traboulsi H, Larkin H, Bonin MA, Volkov L, Lavoie CL, Marsault É. Macrocytic Cell Penetrating Peptides: A Study of Structure-Penetration Properties. *Bioconjug Chem*. 2015;
55. Qian Z, Liu T, Liu YY, Briesewitz R, Barrios AM, Jhiang SM, et al. Efficient delivery of cyclic peptides into mammalian cells with short sequence motifs. *ACS Chem Biol*. 2013;
56. Qian Z, Larochele JR, Jiang B, Lian W, Hard RL, Selner NG, et al. Early endosomal escape of a cyclic cell-penetrating peptide allows effective

- cytosolic cargo delivery. *Biochemistry*. 2014;53(24):4034–46.
57. Qian Z, Martyna A, Hard RL, Wang J, Appiah-Kubi G, Coss C, et al. Discovery and Mechanism of Highly Efficient Cyclic Cell-Penetrating Peptides. *Biochemistry*. 2016;
 58. Aguilera TA, Olson ES, Timmers MM, Jiang T, Tsien RY. Systemic in vivo distribution of activatable cell penetrating peptides is superior to that of cell penetrating peptides. *Integr Biol*. 2009;
 59. Sarko D, Beijer B, Boy RG, Nothelfer EM, Leotta K, Eisenhut M, et al. The pharmacokinetics of cell-penetrating peptides. *Mol Pharm*. 2010;
 60. Lau YH, De Andrade P, Wu Y, Spring DR. Peptide stapling techniques based on different macrocyclisation chemistries. *Chemical Society Reviews*. 2015.
 61. Chu Q, Moellering RE, Hilinski GJ, Kim YW, Grossmann TN, Yeh JTH, et al. Towards understanding cell penetration by stapled peptides. *Medchemcomm*. 2015;
 62. Kim YW, Verdine GL. Stereochemical effects of all-hydrocarbon tethers in *i,i*+4 stapled peptides. *Bioorganic Med Chem Lett*. 2009;
 63. Chang YS, Graves B, Guerlavais V, Tovar C, Packman K, To KH, et al. Stapled α -helical peptide drug development: A potent dual inhibitor of MDM2 and MDMX for p53-dependent cancer therapy. *Proc Natl Acad Sci U S A*. 2013;
 64. Shustov AR, Horwitz SM, Zain J, Patel MR, Goel S, Sokol L, et al. Preliminary

- Results of the Stapled Peptide ALRN-6924, a Dual Inhibitor of MDMX and MDM2, in Two Phase IIa Dose Expansion Cohorts in Relapsed/Refractory TP53 Wild-Type Peripheral T-Cell Lymphoma. *Blood*. 2018;
65. Moellering RE, Cornejo M, Davis TN, Bianco C Del, Aster JC, Blacklow SC, et al. Direct inhibition of the NOTCH transcription factor complex. *Nature*. 2009;
 66. Grossmann TN, Yeh JTH, Bowman BR, Chu Q, Moellering RE, Verdine GL. Inhibition of oncogenic Wnt signaling through direct targeting of β -catenin. *Proc Natl Acad Sci U S A*. 2012;
 67. Zhang G, Barragan F, Wilson K, Levy N, Herskovits A, Sapozhnikov M, et al. A Solid-Phase Approach to Accessing Bisthioether-Stapled Peptides Resulting in a Potent Inhibitor of PRC2 Catalytic Activity. *Angew Chemie - Int Ed*. 2018;
 68. Roberts RW, Szostak JW. RNA-peptide fusions for the in vitro selection of peptides and proteins. *Proc Natl Acad Sci U S A*. 1997;
 69. Takahashi TT, Austin RJ, Roberts RW. mRNA display: Ligand discovery, interaction analysis and beyond. *Trends in Biochemical Sciences*. 2003.
 70. Wang H, Liu R. Advantages of mRNA display selections over other selection techniques for investigation of protein-protein interactions. *Expert Review of Proteomics*. 2011.
 71. Barrick JE, Takahashi TT, Balakin A, Roberts RW. Selection of RNA-binding peptides using mRNA-peptide fusions. *Methods*. 2001;
 72. Kamalinia G, Engel BJ, Srinivasamani A, Grindel BJ, Ong JN, Curran MA, et

- al. mRNA Display Discovery of a Novel Programmed Death Ligand 1 (PD-L1) Binding Peptide (a Peptide Ligand for PD-L1). *ACS Chem Biol.* 2020;1.
73. Olson CA, Adams JD, Takahashi TT, Qi H, Howell SM, Wu TT, et al. Rapid mRNA-display selection of an IL-6 inhibitor using continuous-flow magnetic separation. *Angew Chemie - Int Ed.* 2011;50(36):8295–8.
74. Fukuda I, Kojoh K, Tabata N, Doi N, Takashima H, Miyamoto-Sato E, et al. In vitro evolution of single-chain antibodies using mRNA display. *Nucleic Acids Res.* 2006;
75. Engel BJ, Grindel BJ, Gray JP, Millward SW. Purification of poly-dA oligonucleotides and mRNA-protein fusions with dT25-OAS resin. *Bioorganic Med Chem Lett.* 2020;
76. Millward SW, Takahashi TT, Roberts RW. A general route for post-translational cyclization of mRNA display libraries. *J Am Chem Soc.* 2005;127(41):14142–3.
77. Feng Y, He D, Yao Z, Klionsky DJ. The machinery of macroautophagy. *Cell Research.* 2014.
78. Marino G, Niso-Santano M, Baehrecke EH, Kroemer G. Self-consumption: the interplay of autophagy and apoptosis. *Nat Rev Mol Cell Biol* [Internet]. 2014;15(2):81–94. Available from:
<http://www.ncbi.nlm.nih.gov/pubmed/24401948>
<http://www.ncbi.nlm.nih.gov/pmc/articles/PMC3970201/pdf/nihms560579.pdf>

79. Ornelas A, McCullough CR, Lu Z, Zacharias NM, Kelderhouse LE, Gray J, et al. Induction of autophagy by ARHI (DIRAS3) alters fundamental metabolic pathways in ovarian cancer models. *BMC Cancer*. 2016;
80. Lu Z, Luo RZ, Lu Y, Zhang X, Yu Q, Khare S, et al. The tumor suppressor gene ARHI regulates autophagy and tumor dormancy in human ovarian cancer cells. *J Clin Invest*. 2008;
81. Karantza V, White E. Role of Autophagy in Breast Cancer. *Autophagy*. 2007;
82. Han Y, Fan S, Qin T, Yang J, Sun Y, Lu Y, et al. Role of autophagy in breast cancer and breast cancer stem cells (Review). *International Journal of Oncology*. 2018.
83. Yu L, Gu C, Zhong D, Shi L, Kong Y, Zhou Z, et al. Induction of autophagy counteracts the anticancer effect of cisplatin in human esophageal cancer cells with acquired drug resistance. *Cancer Lett*. 2014;355(1):34–45.
84. Wen YA, Xing X, Harris JW, Zaytseva YY, Mitov MI, Napier DL, et al. Adipocytes activate mitochondrial fatty acid oxidation and autophagy to promote tumor growth in colon cancer. *Cell Death Dis*. 2017;
85. Muilenburg D, Parsons C, Coates J, Virudachalam S, Bold RJ. Role of autophagy in apoptotic regulation by Akt in pancreatic cancer. *Anticancer Res*. 2014;
86. Bryant KL, Der CJ. Blocking autophagy to starve pancreatic cancer. *Nat Rev Mol Cell Biol*. 2019;

87. Yang S, Wang X, Contino G, Liesa M, Sahin E, Ying H, et al. Pancreatic cancers require autophagy for tumor growth. *Genes Dev.* 2011 Apr;25(7):717–29.
88. Zhang SF, Wang XY, Fu ZQ, Peng QH, Zhang JY, Ye F, et al. TXNDC17 promotes paclitaxel resistance via inducing autophagy in ovarian cancer. *Autophagy.* 2015;11(2):225–38.
89. Wang J, Wu GS. Role of autophagy in cisplatin resistance in ovarian cancer cells. *J Biol Chem.* 2014;289(24):17163–73.
90. Ren J-H, He W-S, Nong L, Zhu Q-Y, Hu K, Zhang R-G, et al. Acquired Cisplatin Resistance in Human Lung Adenocarcinoma Cells Is Associated with Enhanced Autophagy. *Cancer Biother Radiopharm [Internet].* 2010;25(1):75–80. Available from:
<http://www.liebertonline.com/doi/abs/10.1089/cbr.2009.0701>
91. Paglin S, Hollister T, Delohery T, Hackett N, McMahon M, Sphicas E, et al. A Novel Response of Cancer Cells to Radiation Involves Autophagy and Formation of Acidic Vesicles Advances in Brief A Novel Response of Cancer Cells to Radiation Involves Autophagy and Formation of Acidic Vesicles 1. *2001;(212):439–44.*
92. Ito H, Daido S, Kanzawa T, Kondo S, Kondo Y. Radiation-induced autophagy is associated with LC3 and its inhibition sensitizes malignant glioma cells. *Int J Oncol.* 2005;26(5):1401–10.

93. Apel A, Herr I, Schwarz H, Rodemann HP, Mayer A. Blocked autophagy sensitizes resistant carcinoma cells to radiation therapy. *Cancer Res.* 2008;68(5):1485–94.
94. Geleris J, Sun Y, Platt J, Zucker J, Baldwin M, Hripcsak G, et al. Observational Study of Hydroxychloroquine in Hospitalized Patients with Covid-19. *N Engl J Med.* 2020;
95. Wetterholm DH, Winter FC. Histopathology of Chloroquine Retinal Toxicity. *Arch Ophthalmol.* 1964;
96. Leung LSB, Neal JW, Wakelee HA, Sequist L V., Marmor MF. Rapid Onset of Retinal Toxicity from High-Dose Hydroxychloroquine Given for Cancer Therapy. *Am J Ophthalmol.* 2015;
97. Chen CY, Wang FL, Lin CC. Chronic hydroxychloroquine use associated with QT prolongation and refractory ventricular arrhythmia. *Clin Toxicol.* 2006;
98. Johansen T, Lamark T. Selective Autophagy: ATG8 Family Proteins, LIR Motifs and Cargo Receptors. *Journal of Molecular Biology.* 2020.
99. Noda NN, Ohsumi Y, Inagaki F. Atg8-family interacting motif crucial for selective autophagy. *FEBS Lett [Internet].* 2010;584(7):1379–85. Available from: <http://dx.doi.org/10.1016/j.febslet.2010.01.018>
100. Pankiv S, Clausen TH, Lamark T, Brech A, Bruun JA, Outzen H, et al. p62/SQSTM1 binds directly to Atg8/LC3 to facilitate degradation of ubiquitinated protein aggregates by autophagy*[S]. *J Biol Chem.*

2007;282(33):24131–45.

101. Birgisdottir ÅB, Lamark T, Johansen T. The LIR motif - crucial for selective autophagy. *Journal of Cell Science*. 2013.
102. Yorimitsu T, Klionsky DJ. Autophagy: Molecular machinery for self-eating. *Cell Death and Differentiation*. 2005.
103. He C, Klionsky DJ. Regulation Mechanisms and Signaling Pathways of Autophagy. *Annu Rev Genet*. 2009;
104. Xie Z, Klionsky DJ. Autophagosome formation: Core machinery and adaptations. *Nature Cell Biology*. 2007.
105. Johansen T, Lamark T. Selective autophagy mediated by autophagic adapter proteins. *Autophagy*. 2011.
106. Rogov V, Dötsch V, Johansen T, Kirkin V. Interactions between Autophagy Receptors and Ubiquitin-like Proteins Form the Molecular Basis for Selective Autophagy. *Molecular Cell*. 2014.
107. Mathew R, Karantza-Wadsworth V, White E. Role of autophagy in cancer. *Nat Rev Cancer* [Internet]. 2007;7(12):961–7. Available from: <http://www.pubmedcentral.nih.gov/articlerender.fcgi?artid=2866167&tool=pmc-entrez&rendertype=abstract>
108. Yang ZJ, Chee CE, Huang S, Sinicrope FA. The Role of Autophagy in Cancer: Therapeutic Implications. *Mol Cancer Ther* [Internet]. 2011;10(9):1533–41. Available from: <http://mct.aacrjournals.org/cgi/doi/10.1158/1535-7163.MCT-11->

109. White E. Deconvoluting the context-dependent role for autophagy in cancer. *Nature Reviews Cancer*. 2012.
110. White E. the role for autophagy in cancer (White, 2015).pdf. *J Clin Invest* [Internet]. 2015;125(1):42–6. Available from: <http://www.jci.org/articles/view/73941%5Cnpapers3://publication/doi/10.1172/jci73941>
111. Galluzzi L, Pietrocola F, Bravo-San Pedro JM, Amaravadi RK, Baehrecke EH, Cecconi F, et al. Autophagy in malignant transformation and cancer progression. *EMBO J*. 2015;
112. Kondo Y, Kanzawa T, Sawaya R, Kondo S. The role of autophagy in cancer development and response to therapy. *Nat Rev Cancer* [Internet]. 2005;5(9):726–34. Available from: <http://www.nature.com/nrc/journal/v5/n9/pdf/nrc1692.pdf>
113. Washington MN, Suh G, Orozco AF, Sutton MN, Yang H, Wang Y, et al. ARHI (DIRAS3)-mediated autophagy-associated cell death enhances chemosensitivity to cisplatin in ovarian cancer cell lines and xenografts. *Cell Death Dis*. 2015;
114. Fujii S, Mitsunaga S, Yamazaki M, Hasebe T, Ishii G, Kojima M, et al. Autophagy is activated in pancreatic cancer cells and correlates with poor patient outcome. *Cancer Sci*. 2008;

115. Hashimoto D, Bläuer M, Hirota M, Ikonen NH, Sand J, Laukkarinen J. Autophagy is needed for the growth of pancreatic adenocarcinoma and has a cytoprotective effect against anticancer drugs. *Eur J Cancer*. 2014;
116. New M, Van Acker T, Long JS, Sakamaki J, Ryan KM, Tooze SA. Molecular Pathways Controlling Autophagy in Pancreatic Cancer. *Front Oncol*. 2017;
117. Gong C, Bauvy C, Tonelli G, Yue W, Deloménie C, Nicolas V, et al. Beclin 1 and autophagy are required for the tumorigenicity of breast cancer stem-like/progenitor cells. *Oncogene*. 2013;
118. Poillet-Perez L, Xie X, Zhan L, Yang Y, Sharp DW, Hu ZS, et al. Autophagy maintains tumour growth through circulating arginine. *Nature*. 2018.
119. Karsli-Uzunbas G, Guo JY, Price S, Teng X, Laddha S V., Khor S, et al. Autophagy is required for glucose homeostasis and lung tumor maintenance. *Cancer Discov*. 2014;4(8):915–27.
120. Wu HM, Jiang ZF, Ding PS, Shao LJ, Liu RY. Hypoxia-induced autophagy mediates cisplatin resistance in lung cancer cells. *Sci Rep [Internet]*. 2015;5:1–15. Available from: <http://dx.doi.org/10.1038/srep12291>
121. Sui X, Chen R, Wang Z, Huang Z, Kong N, Zhang M, et al. Autophagy and chemotherapy resistance: A promising therapeutic target for cancer treatment. *Cell Death Dis*. 2013;4(10):1–12.
122. Lomonaco SL, Finniss S, Xiang C, DeCarvalho A, Umansky F, Kalkanis SN, et al. The induction of autophagy by ??-radiation contributes to the

- radioresistance of glioma stem cells. *Int J Cancer*. 2009;125(3):717–22.
123. Yao KC, Komata T, Kondo Y, Kanzawa T, Kondo S, Germano IM. Molecular response of human glioblastoma multiforme cells to ionizing radiation: cell cycle arrest, modulation of cyclin-dependent kinase inhibitors, and autophagy. *J Neurosurg* [Internet]. 2003;98(2):378–84. Available from: <http://thejns.org/doi/10.3171/jns.2003.98.2.0378>
124. Chaachouay H, Ohneseit P, Toulany M, Kehlbach R, Multhoff G, Rodemann HP. Autophagy contributes to resistance of tumor cells to ionizing radiation. *Radiother Oncol* [Internet]. 2011;99(3):287–92. Available from: <http://dx.doi.org/10.1016/j.radonc.2011.06.002>
125. Smith AG, Macleod KF. Autophagy, cancer stem cells and drug resistance. *Journal of Pathology*. 2019.
126. Amaravadi RK, Kimmelman AC, Debnath J. Targeting autophagy in cancer: Recent advances and future directions. *Cancer Discovery*. 2019.
127. Chude CI, Amaravadi RK. Targeting autophagy in cancer: Update on clinical trials and novel inhibitors. *Int J Mol Sci*. 2017;18(6).
128. Marinković M, Šprung M, Buljubašić M, Novak I. Autophagy modulation in cancer: Current knowledge on action and therapy. *Oxidative Medicine and Cellular Longevity*. 2018.
129. Padman BS, Nguyen TN, Lazarou M. Autophagosome formation and cargo sequestration in the absence of LC3/GABARAPs. *Autophagy*. 2017.

130. Noda NN, Kumeta H, Nakatogawa H, Satoo K, Adachi W, Ishii J, et al. Structural basis of target recognition by Atg8/LC3 during selective autophagy. *Genes to Cells*. 2008;13(12):1211–8.
131. Fuller JC, Burgoyne NJ, Jackson RM. Predicting druggable binding sites at the protein-protein interface. *Drug Discovery Today*. 2009.
132. Arkin MR, Tang Y, Wells JA. Small-molecule inhibitors of protein-protein interactions: Progressing toward the reality. *Chemistry and Biology*. 2014.
133. Wirth M, Zhang W, Razi M, Nyoni L, Joshi D, O'Reilly N, et al. Molecular determinants regulating selective binding of autophagy adapters and receptors to ATG8 proteins. *Nat Commun*. 2019;
134. Faulstich H, Trischmann H, Mayer D. Preparation of tetramethylrhodaminyl-phalloidin and uptake of the toxin into short-term cultured hepatocytes by endocytosis. *Exp Cell Res*. 1983;
135. Fischer WJ, Altheimer S, Cattori V, Meier PJ, Dietrich DR, Hagenbuch B. Organic anion transporting polypeptides expressed in liver and brain mediate uptake of microcystin. *Toxicol Appl Pharmacol*. 2005;
136. Letschert K, Faulstich H, Keller D, Keppler D. Molecular characterization and inhibition of amanitin uptake into human hepatocytes. *Toxicol Sci*. 2006;
137. Giordanetto F, Kihlberg J. Macrocyclic drugs and clinical candidates: What can medicinal chemists learn from their properties? *J Med Chem*. 2014;
138. Qian Z, Dougherty PG, Pei D. Targeting intracellular protein–protein

- interactions with cell-permeable cyclic peptides. *Current Opinion in Chemical Biology*. 2017.
139. Rezai T, Yu B, Millhauser GL, Jacobson MP, Lokey RS. Testing the conformational hypothesis of passive membrane permeability using synthetic cyclic peptide diastereomers. *J Am Chem Soc*. 2006;128(8):2510–1.
 140. White TR, Renzelman CM, Rand AC, Rezai T, McEwen CM, Gelev VM, et al. On-resin N-methylation of cyclic peptides for discovery of orally bioavailable scaffolds. *Nat Chem Biol*. 2011;
 141. Rhodes CA, Dougherty PG, Cooper JK, Qian Z, Lindert S, Wang QE, et al. Cell-Permeable Bicyclic Peptidyl Inhibitors against NEMO-I κ B Kinase Interaction Directly from a Combinatorial Library. *J Am Chem Soc*. 2018;
 142. Kritzer JA, Lear JD, Hodsdon ME, Schepartz A. Helical β -peptide inhibitors of the p53-hDM2 interaction. *J Am Chem Soc*. 2004;
 143. Pisaneschi F, Kelderhouse LE, Hardy A, Engel BJ, Mukhopadhyay U, Gonzalez-Lepera C, et al. Automated, Resin-Based Method to Enhance the Specific Activity of Fluorine-18 Clicked PET Radiotracers. *Bioconj Chem*. 2017;acs.bioconjchem.6b00678.
 144. Fiacco S V., Kelderhouse LE, Hardy A, Peleg Y, Hu B, Ornelas A, et al. Directed Evolution of Scanning Unnatural-Protease-Resistant (SUPR) Peptides for in Vivo Applications. *ChemBioChem*. 2016;1643–51.
 145. Howell SM, Fiacco S V, Takahashi TT, Jalali-Yazdi F, Millward SW, Hu B, et

- al. Serum stable natural peptides designed by mRNA display. *Sci Rep* [Internet]. 2014;4:6008. Available from:
<http://www.nature.com/srep/2014/140919/srep06008/full/srep06008.html%5Cn>
<http://www.ncbi.nlm.nih.gov/pubmed/25234472%5Cnhttp://www.pubmedcentral.nih.gov/articlerender.fcgi?artid=PMC4168267>
146. Cheng X, Wang Y, Gong Y, Li F, Guo Y, Hu S, et al. Structural basis of FYCO1 and MAP1LC3A interaction reveals a novel binding mode for Atg8-family proteins. *Autophagy*. 2016;
147. Campa VM, Capilla A, Varela MJ, De La Rocha AMA, Fernandez-Troyano JC, Belén Barreiro R, et al. Endocytosis as a biological response in receptor pharmacology: Evaluation by fluorescence microscopy. *PLoS One*. 2015;
148. Jiang Y, Ji F, Liu Y, He M, Zhang Z, Yang J, et al. Cisplatin-induced autophagy protects breast cancer cells from apoptosis by regulating yes-associated protein. *Oncol Rep*. 2017;
149. Mitra AK, Davis DA, Tomar S, Roy L, Gurler H, Xie J, et al. In vivo tumor growth of high-grade serous ovarian cancer cell lines. *Gynecol Oncol*. 2015;
150. Walensky LD, Kung AL, Escher I, Malia TJ, Barbuto S, Wright RD, et al. Activation of apoptosis in vivo by a hydrocarbon-stapled BH3 helix. *Science* (80-). 2004;
151. Li YC, Rodewald LW, Hoppmann C, Wong ET, Lebreton S, Safar P, et al. A Versatile Platform to Analyze Low-Affinity and Transient Protein-Protein

- Interactions in Living Cells in Real Time. *Cell Rep.* 2014;
152. Okamoto T, Zobel K, Fedorova A, Quan C, Yang H, Fairbrother WJ, et al. Stabilizing the pro-apoptotic BimBH3 helix (BimSAHB) does not necessarily enhance affinity or biological activity. *ACS Chem Biol.* 2013;
 153. Szadvari I, Krizanova O, Babula P. Athymic nude mice as an experimental model for cancer treatment. *Physiological Research.* 2016.
 154. Kelland LR. "Of mice and men": Values and liabilities of the athymic nude mouse model in anticancer drug development. *Eur J Cancer.* 2004;
 155. Baginska J, Viry E, Berchem G, Poli A, Noman MZ, Van Moer K, et al. Granzyme B degradation by autophagy decreases tumor cell susceptibility to natural killer-mediated lysis under hypoxia. *Proc Natl Acad Sci U S A.* 2013;
 156. Messai Y, Noman MZ, Hasmim M, Janji B, Tittarelli A, Boutet M, et al. ITPR1 protects renal cancer cells against natural killer cells by inducing autophagy. *Cancer Res.* 2014;
 157. Liu K, Zhao E, Ilyas G, Lalazar G, Lin Y, Haseeb M, et al. Impaired macrophage autophagy increases the immune response in obese mice by promoting proinflammatory macrophage polarization. *Autophagy.* 2015;
 158. Yu Y, Xu F, Peng H, Fang X, Zhao S, Li Y, et al. NOEY2 (ARHI), an imprinted putative tumor suppressor gene in ovarian and breast carcinomas. *Proc Natl Acad Sci U S A.* 1999;
 159. Wu X, Liang L, Dong L, Yu Z, Fu X. Effect of ARHI on lung cancer cell

- proliferation, apoptosis and invasion in vitro. *Mol Biol Rep.* 2013;
160. Huang J, Lin Y, Li H, Qing D, Teng XM, Zhang YL, et al. ARHI, as a novel suppressor of cell growth and downregulated in human hepatocellular carcinoma, could contribute to hepatocarcinogenesis. *Mol Carcinog.* 2009;
161. Dalai I, Missiaglia E, Barbi S, Butturini G, Doglioni C, Falconi M, et al. Low expression of ARHI is associated with shorter progression-free survival in pancreatic endocrine tumors. *Neoplasia.* 2007;
162. Lu Z, Luo RZ, Peng H, Rosen DG, Atkinson EN, Warneke C, et al. Transcriptional and posttranscriptional down-regulation of the imprinted tumor suppressor gene ARHI (DRAS3) in ovarian cancer. *Clin Cancer Res.* 2006;
163. Luo RZ, Fang X, Marquez R, Liu SY, Mills GB, Liao WSL, et al. ARHI is a Ras-related small G-protein with a novel N-terminal extension that inhibits growth of ovarian and breast cancers. *Oncogene.* 2003;
164. Sutton MN, Lu Z, Li YC, Zhou Y, Huang T, Reger AS, et al. DIRAS3 (ARHI) Blocks RAS/MAPK Signaling by Binding Directly to RAS and Disrupting RAS Clusters. *Cell Rep [Internet].* 2019;29(11):3448-3459.e6. Available from: <https://doi.org/10.1016/j.celrep.2019.11.045>
165. Bailey MR, Khokhlova V a., Sapozhnikov O a., Kargl SG, Crum L a. Physical mechanisms of the therapeutic effect of ultrasound (a review). *Acoust Phys [Internet].* 2003 Jul;49(4):369–88. Available from: <http://link.springer.com/10.1134/1.1591291>

166. Kennedy JE. High-intensity focused ultrasound in the treatment of solid tumours. *Nat Rev Cancer*. 2005;5:321–7.
167. Lee LA, Simon C, Ph D, Bove EL, Mosca RS, Ebbini ES, et al. High Intensity Focused Ultrasound Effect on Cardiac Tissues : Potential for Clinical Application. *Echocardiography*. 2000;17(6):563–6.
168. Groh M a, Binns O a, Burton HG, Ely SW, Johnson AM. Ultrasonic cardiac ablation for atrial fibrillation during concomitant cardiac surgery: long-term clinical outcomes. *Ann Thorac Surg [Internet]*. 2007 Dec [cited 2014 Oct 23];84(6):1978–83. Available from:
<http://www.ncbi.nlm.nih.gov/pubmed/18036920>
169. Jagannathan J, Sanghvi NT, Crum LA, Yen CP, Medel R, Dumont AS, et al. High-intensity focused ultrasound surgery of the brain: Part 1-A historical perspective with modern applications. Vol. 64, *Neurosurgery*. 2009. p. 201–10.
170. Dromi S, Frenkel V, Luk A, Traugher B, Angstadt M, Bur M, et al. Pulsed-high intensity focused ultrasound and low temperature-sensitive liposomes for enhanced targeted drug delivery and antitumor effect. *Clin Cancer Res [Internet]*. 2007 May 1 [cited 2014 Oct 23];13(9):2722–7. Available from:
<http://www.pubmedcentral.nih.gov/articlerender.fcgi?artid=2555974&tool=pmc&rendertype=abstract>
171. U.S. Food and Drug Administration Center for Devices and Radiological Health. InSightec ExAblate® System, Model 2000/2100/2100 VI approval letter. 2012.

172. Goldberg SN, Grassi CJ, Cardella JF, Charboneau JW, Dodd GD, Dupuy DE, et al. Image-guided tumor ablation: standardization of terminology and reporting criteria. *JVIR*. 2005 Jun;16(6):765–78.
173. Hynynen K, Damianou C, Darkazanli A, Unger E, Levy M, Schenck JF. On-line MRI monitored noninvasive ultrasound surgery. 1992 14th Annu Int Conf IEEE Eng Med Biol Soc. 1992;1:350–1.
174. Jolesz F a. MRI-guided focused ultrasound surgery. *Annu Rev Med* [Internet]. 2009 Jan [cited 2014 Oct 23];60:417–30. Available from: <http://www.pubmedcentral.nih.gov/articlerender.fcgi?artid=4005559&tool=pmc&rendertype=abstract>
175. Bouchard RR, Sahin O, Emelianov SS. Ultrasound-guided photoacoustic imaging: current state and future development. *IEEE Trans Ultrason Ferroelectr Freq Control*. 2014 Mar;61(3):450–66.
176. Xu M, Wang L V. Photoacoustic imaging in biomedicine. *Rev Sci Instrum* [Internet]. 2006 [cited 2014 Jul 18];77(4):041101. Available from: <http://scitation.aip.org/content/aip/journal/rsi/77/4/10.1063/1.2195024>
177. Beard P. Biomedical photoacoustic imaging. *Interface Focus*. 2011;(June).
178. Smith AM, Mancini MC, Nie S. Bioimaging: second window for in vivo imaging. *Nat Nanotechnol* [Internet]. 2009 Nov [cited 2014 Oct 21];4(11):710–1. Available from: <http://www.pubmedcentral.nih.gov/articlerender.fcgi?artid=2862008&tool=pmc>

entrez&rendertype=abstract

179. Mallidi S, Luke GP, Emelianov S. Photoacoustic imaging in cancer detection, diagnosis, and treatment guidance. *Trends Biotechnol* [Internet]. 2011 May [cited 2014 Oct 24];29(5):213–21. Available from:
<http://www.pubmedcentral.nih.gov/articlerender.fcgi?artid=3080445&tool=pmc>
entrez&rendertype=abstract
180. Shah J, Park S, Aglyamov S, Larson T, Ma L, Sokolov K, et al. Photoacoustic imaging and temperature measurement for photothermal cancer therapy. *Biomed Opt*. 2008 Jan;13(3):34024.
181. Larin K V. Monitoring of temperature distribution in tissues with optoacoustic technique in real time. *Proc SPIE*. 2000;3916:311–21.
182. Larina I V, Larin K V, Esenaliev RO. Real-time optoacoustic monitoring of temperature in tissues. Vol. 38, *Journal of Physics D: Applied Physics*. 2005. p. 2633–9.
183. Pramanik M, Wang LV. Thermoacoustic and photoacoustic sensing of temperature. *J Biomed Opt*. 2009;14(5):054024.
184. Schlesinger D, Benedict S, Diederich C, Gedroyc W, Klibanov A, Larner J. MR-guided focused ultrasound surgery, present and future. *Med Phys*. 2013 Aug;40(8):080901.
185. Rosenthal EL, Warram JM, Bland KI, Zinn KR. The Status of Contemporary Image-Guided Modalities in Oncologic Surgery. *Ann Surg*. 2015

May;261(1):46–55.

186. Vaezy S, Shi X, Martin RW, Chi E, Nelson PI, Bailey MR, et al. Real-time Visualization of High-Intensity Focused Ultrasound Treatment Using Ultrasound Imaging. *Ultrasound Med Biol*. 2001;27(1):33–42.
187. Righetti R, Kallel F, Stafford RJ, Price RE, Krouskop TA, Hazle JD, et al. Elastographic characterization of HIFU-induced lesions in canine livers. *Ultrasound Med Biol*. 1999;25:1099–113.
188. Ottenhausen M, Bodhinayake I, Banu M, Kesavabhotla K, Ray A, Boockvar J a. Industry progress report on neuro-oncology: Biotech update 2013. *J Neurooncol* [Internet]. 2013 Nov [cited 2014 Oct 14];115(2):311–6. Available from: <http://www.ncbi.nlm.nih.gov/pubmed/23949146>
189. Quesson B, de Zwart J, Moonen C. Magnetic resonance temperature imaging for guidance of thermotherapy. *J Magn Reson Imaging* [Internet]. 2000 Oct;12(4):525–33. Available from: <http://www.ncbi.nlm.nih.gov/pubmed/11042633>
190. Lee HJ, Liu Y, Zhao J, Zhou M, Bouchard RR, Mitcham T, et al. In vitro and in vivo mapping of drug release after laser ablation thermal therapy with doxorubicin-loaded hollow gold nanoshells using fluorescence and photoacoustic imaging. *J Control Release Soc*. 2013 Nov;172(1):152–8.
191. Dana N, Di Biase L, Natale A, Emelianov S, Bouchard R. In vitro photoacoustic visualization of myocardial ablation lesions. *Heart Rhythm*

- [Internet]. 2014 Jan [cited 2014 Oct 13];11(1):150–7. Available from:
<http://www.ncbi.nlm.nih.gov/pubmed/24080065>
192. Chitnis P V, Brecht H-P, Su R, Oraevsky A a. Feasibility of optoacoustic visualization of high-intensity focused ultrasound-induced thermal lesions in live tissue. *J Biomed Opt.* 2010;15(April):021313.
 193. Cui H, Staley J, Yang X. Integration of photoacoustic imaging and high-intensity focused ultrasound. *J Biomed Opt.* 2010;15:021312.
 194. Sun Y, O'Neill B. Imaging high-intensity focused ultrasound-induced tissue denaturation by multispectral photoacoustic method: an ex vivo study. *Appl Opt [Internet]*. 2013 Mar 10;52(8):1764. Available from:
<http://www.ncbi.nlm.nih.gov/pubmed/23478783>
 195. Cui H, Yang X. In vivo imaging and treatment of solid tumor using integrated photoacoustic imaging and high intensity focused ultrasound system. *Med Phys.* 2010;37:4777–81.
 196. Cui H, Yang X. Real-time monitoring of high-intensity focused ultrasound ablations with photoacoustic technique: an in vitro study. *Med Phys [Internet]*. 2011 Oct [cited 2015 Jan 13];38(10):5345–50. Available from:
<http://www.ncbi.nlm.nih.gov/pubmed/21992353>
 197. Funke AR, Aubry JF, Fink M, Boccara AC, Bossy E. Photoacoustic guidance of high intensity focused ultrasound with selective optical contrasts and time-reversal. *Appl Phys Lett.* 2009;94(5).

198. Khokhlova TD, Pelivanov IM, Sapozhnikov O a, Solomatin VS, Karabutov A a. Opto-acoustic diagnostics of the thermal action of high-intensity focused ultrasound on biological tissues: the possibility of its applications and model experiments. *Quantum Electron* [Internet]. 2006 Dec 31 [cited 2015 Jan 14];36(12):1097–102. Available from: <http://stacks.iop.org/1063-7818/36/i=12/a=A03?key=crossref.8a713888d2484d9e17be3fb5baa2c59d>
199. Kim JG, Xia M, Liu H. Extinction coefficients of hemoglobin for near-infrared spectroscopy of tissue. *IEEE Eng Med Biol Mag*. 2005;24:118–21.
200. Black MM, Kleiner IS. The Use of Triphenyltetrazolium Chloride for the Study of Respiration of Tissue Slices. *Science* (80-). 1949;110(2868):660–1.
201. Berridge M, Tan A, McCoy K, Wang R. The biochemical and cellular basis of cell proliferation assays that use tetrazolium salts. *Biochemica* [Internet]. 1996 [cited 2015 Jan 13];(4):4–9. Available from: http://lifescience.roche.com/wcsstore/RASCatalogAssetStore/Articles/BIOCHEMA_96_4_p14-19.pdf
202. Cui H, Yang X. Real-time monitoring of high-intensity focused ultrasound ablations with photoacoustic technique: an in vitro study. *Med Phys*. 2011 Oct;38(10):5345–50.
203. Mitcham T, Marques T, Chatterjee D, Krishnan S, Pugh T, Bouchard R. Transrectal photoacoustic-ultrasonic imaging enhancement through interstitial irradiation and targeted nanoparticles. In: *Proceedings of the 2013 IEEE Ultrasonics Symposium*. 2013.

204. Hennessy R, Lim SL, Markey MK, Tunnell JW. Monte Carlo lookup table-based inverse model for extracting optical properties from tissue-simulating phantoms using diffuse reflectance spectroscopy. *J Biomed Opt.* 2013;18(3):037003.
205. Prost A, Funke A, Tanter M, Aubry J-F, Bossy E. Photoacoustic-guided ultrasound therapy with a dual-mode ultrasound array. *J Biomed Opt.* 2012;17:061205.
206. Khokhlova TD, Pelivanov IM, Sapozhnikov O a, Solomatin VS, Karabutov A a. Opto-acoustic diagnostics of the thermal action of high-intensity focused ultrasound on biological tissues: the possibility of its applications and model experiments. *Quantum Electron.* 2006 Dec;36(12):1097–102.
207. Farahani K, Saxton RE, Yoon HC, De Salles AAF, Black KL, Lufkin RB. MRI of thermally denatured blood: Methemoglobin formation and relaxation effects. *Magn Reson Imaging.* 1999;17:1489–94.
208. Black JF, Barton JK. Chemical and structural changes in blood undergoing laser photocoagulation. *Photochem Photobiol.* 2004;80:89–97.
209. Yan Y-B, Wang Q, He H-W, Zhou H-M. Protein thermal aggregation involves distinct regions: sequential events in the heat-induced unfolding and aggregation of hemoglobin. *Biophys J.* 2004;86:1682–90.
210. Hsiao Y-S, Wang X, Deng CX. Dual-wavelength photoacoustic technique for monitoring tissue status during thermal treatments. *J Biomed Opt [Internet].*

2013;18:067003. Available from:

<http://www.ncbi.nlm.nih.gov/pubmed/23733048>

VITA

Joshua Gray was born in Beverly, Massachusetts, the son of Michael Gray and Shari Litch Gray. After completing his work in high school, he entered Boston University in Boston, Massachusetts. He received the degree of Bachelor of Arts in

physics from Boston University in May 2013. While he was at Boston University, he worked in laboratory of Paul Hall, Ph.D. modeling the effects of mantle plumes on plate tectonics and the formation of island chains. In 2012, he worked as a research assistant in the laboratory of Ugo Amaldi, Ph.D. at the Organisation européenne pour la recherche nucléaire (CERN) in Geneva, Switzerland where he designed bending and focusing magnets for a prototype carbon ion linear accelerator for heavy ion treatment of cancer. After graduation from Boston University, he joined the Ph.D. program at the University of Texas MD Anderson Cancer Center UTHealth Graduate School of Biomedical Sciences in June 2013